Contact damage on ceramic laminates

Luca Ceseracciu

PhD Dissertation to opt to the degree of Doctor in Materials Science
for the Technical University of Catalonia

Advisors:
Prof. Marc Anglada
Dr. Emilio Jiménez Piqué

Thesis developed at the Universitat Politècnica de Cataluña
Departament de Ciència dels Materials i Enginyeria Metal·lúrgica
May 2008

Abstract

The use of ceramic materials in many industrial fields is spread and ever-increasing, for their excellent properties, either mechanical, thermal, tribological or biological. However, their intrinsic brittleness and lack of reliability are obstacles to further spreading these materials in applications where structural resistance is required. To build multilayered composite structures is a promising way which aims to increase the reliability of ceramics. As it is common in composite materials, layered materials allow the mechanical properties to be superior to those of the constituent materials, in the studied case due to the presence of compressive residual stress in the surface.

The best applications for such materials are those related to the surface properties; for this reason the response to contact loading is especially important to characterize the mechanical properties and to assist in the design of advanced ceramic composites. Hertzian indentation techniques provide a powerful tool to study such type of loading, which is otherwise difficult to characterize with the traditional mechanical testing methodologies.

Contact damage in brittle materials appears mainly as surface ring-cracks, which can develop in a characteristic cone crack. Such fissuration is detrimental to the functionality of the material, and can lead to the failure of the component. Tough ceramics often present another type of damage, the so-called quasi-plasticity, generated as subsurface microcracking and which is cause of inelastic deformation.

In this thesis, alumina-based ceramic laminates were characterized in their resistance to contact damage in all its aspects, starting from the appearance of surface fissures, to the propagation of brittle cracks in the first layer and its influence on the material strength, to the contact loading-induced failure. Experimental measurements were coupled with Finite Element analysis of the involved parameters, which assisted in formulating comprehensive guidelines for the correct characterization and the design of advanced multilayered ceramics.

Abstract

The presence of residual stress in ceramic laminates proved to be effective in improving the material resistance to the ring cracking, generated by monotonic, cyclic and long-lasting tests. The better resistance to these latter revealed the existence of grain bridging hindering the crack formation, unexpected in fine-grained alumina and which was related to the small crack character of the ring crack. Longer lasting cyclic tests showed that more severe damage appears in the multilayered materials than in the monolithic one, suggesting a modification of the predominant damage mode to quasi-plastic-derived surface degradation.

Propagation of long cone cracks is affected by residual stress in both the length and angle. An automatic Finite Element model of crack propagation allowed to predict crack growth as a function of both the extrinsic residual stresses and of microstructural parameters, which helped address the long-open question of the cone crack angle on polycrystalline materials.

The response to remote loading of indented materials, in other words the strength degradation, is conditioned by the cone crack geometry, as well as by other factors deriving from the laminated structure, such as the presence of residual stress itself and the load redistribution due to the elastic mismatch between layers. Similarly, the contact strength, *i.e.* the resistance to local blunt compression, is improved in the composite materials as a consequence of the residual stresses. Nevertheless, the risk of high stress in the lower tensile layers was highlighted for both types of loading and general consideration on the design of laminated materials were proposed.

In the overall, a comprehensive characterization of the contact properties of the studied materials was achieved, and the understanding of crack propagation on brittle polycrystalline materials was broadened and improved.

Resumen

La difusión de los materiales cerámicos en muchos campos de la industria es amplia y está en fuerte expansión, debido a las excelentes propiedades de estos materiales, ya sean mecánicas, térmicas, tribológicas o biológicas. Sin embargo, su fragilidad intrínseca y falta de fiabilidad limitan una mayor difusión en esas aplicaciones donde se precisa alta resistencia estructural. La producción de composites multilaminares es un camino prometedor para aumentar la fiabilidad de los cerámicos. Los cerámicos multicapa permiten que las propiedades mecánicas sean mejores que las de los componentes, debido a la presencia en la superficie de tensiones residuales de compresión provocadas diferencias de expansión térmica entre las capas.

Las aplicaciones óptimas de estos materiales son las que están relacionadas con las propiedades superficiales; por eso la respuesta a las cargas por contacto son especialmente importantes para caracterizar las propiedades mecánicas y para mejorar el diseño de cerámicos composites avanzados. Las técnicas de indentación Hertziana son herramientas muy útiles para estudiar este tipo de carga, que por otro lado es difícil de caracterizar por ensayos mecánico tradicionales.

El daño por contacto en materiales frágiles aparece principalmente como grietas anillo en la superficie, que pueden desarrollarse como grietas cono, características de este tipo de carga. Este agrietamiento es perjudicial para la funcionalidad del material, y puede llevar al fallo de la pieza. Las cerámicas tenaces, por otro lado, pueden presentar un daño, cuasi-plástico, que se genera debajo la superficie en forma de microagrietamento, y que es causa de deformación inelástica.

En esta tesis, se caracteriza la resistencia al daño por contacto materiales cerámicos en base alúmina, incluyendo todos los aspectos de ese daño, desde la aparición de fisuras superficiales, a la propagación de grietas frágiles en la primera capa y su influencia sobre la resistencia del material, hasta el fallo inducido por carga de contacto. Se comparan medidas experimentales con análisis a los Elementos Finitos de los parámetros involu-

crados en cada caso, lo que permite formular pautas para una correcta caracterización y diseño de cerámicas multicapas avanzados.

Se vio que la presencia de tensiones residuales es efectiva en mejorar la resistencia a la formación de grieta anillo, sea generada por cargas monotónicas, cíclicas o estáticas. La alta resistencia frente a este último tipo de carga revela que existen mecanismos de puenteo intergranular que se oponen a la formación de grietas, lo que era inesperado por el tamaño de grano fino, y que se atribuye a un efecto de grieta corta, comparada con la microestructura. Ensayos cíclicos de larga duración mostraron, por otro lado, que en los materiales multicapas aparece daño superficial más severo que en los monolíticos, lo que sugiere un cambio del daño predominante hacía una degradación superficial producida por cuasi-plasticidad.

Las tensiones residuales afectan tanto la longitud como el ángulo de la grieta cono. Se modeló el problema mediante Elementos Finitos y algoritmos de propagación de grieta, lo que permitió predecir el crecimiento de grieta en función tanto de las tensiones residuales, como de otros parámetros microestructurales, y determinar del ángulo de la grieta cono en materiales policristalinos.

La respuesta a cargas remotas de materiales indentados, en otras palabras la degradación de la resistencia, se ve afectada por la geometría de la grieta cono, y por otros factores que son consecuencia de la estructura laminar, tales como las tensiones residuales y la redistribución de carga por el desajuste elástico entre capas. Asimismo, la resistencia por contacto, o sea la resistencia a compresión roma localizada, se ve mejorada en materiales laminares, como consecuencia de las tensiones residuales. Sin embargo, se evidenció que existe el riesgo de que se genere tensión elevada en las capas interiores bajo ambos tipos de carga, y se propusieron consideraciones generales sobre el diseño de materiales laminares.

En definitiva, se consiguió una caracterización exhaustiva de las propiedades de contacto mecánico de los materiales estudiados, y se amplió y mejoró el conocimiento de la propagación de grieta en materiales frágiles policristalinos.

Contents

Abstract **iii**

Resumen **v**

List of Figures **xi**

Nomenclature **xvii**

1 Introduction **1**

1.1 Advanced ceramics for structural applications 1
1.2 Shielding microstructures 2
1.3 Layered structures 3
1.3.1 Multilayers with weak interfaces 3
1.3.2 Multilayers with strong interfaces 4
1.4 Ceramic laminates with residual stress 5
1.5 Spherical indentation theory 6
1.6 Cone crack 11
1.7 Inelastic contact damage 13
1.8 Failure caused by contact damage 17
1.9 Objectives of the thesis 18

2 Experimental Methods **21**

2.1 Material processing and preparation 21
2.2 Physical and mechanical characterization 24
2.2.1 Mechanical properties 24
2.2.2 Residual stresses 29
2.3 Spherical indentation techniques 33

2.4 Damage observation techniques . . . 36
2.5 Residual strength testing . . . 39
2.6 Contact strength testing . . . 40

3 Finite Element Analysis 43
3.1 Introduction to FEM . . . 43
3.1.1 `Abaqus` . . . 45
3.2 Application: residual stresses evaluation . . . 45
3.3 Application: strength degradation . . . 49
3.4 Application: contact strength . . . 51
3.5 Automated Algorithm of crack propagation . . . 53
3.5.1 Model of punch indentation . . . 54
3.5.2 Output handling . . . 57
3.5.3 Input normalization . . . 59
3.5.4 Example of crack propagation . . . 60
3.5.5 Example of crack initiation . . . 60

4 Surface damage by Hertzian indentation 63
4.1 Ring crack appearance . . . 63
4.1.1 Monotonic loading . . . 64
4.1.2 Static and cyclic loading . . . 66
4.1.3 Crack growth analysis . . . 69
4.2 Severe damage . . . 72

5 Cone crack propagation 79
5.1 R-curve . . . 79
5.1.1 Analytical expression of R-curve and implementation in the FE model . . . 79
5.1.2 Results . . . 82
5.2 Residual stresses . . . 86
5.2.1 Influence of the residual stresses on the unstable propagation . . . 88
5.2.2 Influence of the residual stresses on the stable propagation . . . 89
5.3 Ceramic laminates . . . 90

6 Strength degradation by cone cracking 93

6.1 Flexural strength of laminated materials 94
6.2 Strength degradation 98

7 Contact strength of ceramic laminates **101**
7.1 Experimental results 101
7.2 Finite Element analysis 104
7.3 Considerations on the design with ceramic laminates 106

8 Conclusions **111**

Bibliography **115**

A Script codes of the FE model **123**
A.1 `propcrack.py` 123
A.2 `model.py` 129
A.3 `output.py` 136
A.4 `initcrack.py` 138

List of publications **141**

List of Figures

1.1 Scheme of crack length-dependent toughness, or R-curve 2
1.2 Scheme of crack deflection along the weak interfaces in ceramic laminates. The arrows represent crack deflection/bifurcation 4
1.3 Scheme of residual stress generated in multilayered ceramics from differential shrinkage after sintering. Gray layers represent the ones with lower α. The deformation at the edges has been exaggerated. 5
1.4 Scheme and symbology of Hertzian cone cracking 8
1.5 Scheme of indentation stress-strain curve 9
1.6 Scheme of the Auerbach paradox 9
1.7 Stress intensity factor as a function of the crack length, with the asymptotical Roesler solution 12
1.8 Scheme of shear-activated microcracks, with extensile wings at the grain boundaries 14
1.9 Calculated critical load ratio for selected ceramics, for a sphere radius R=3.18 mm 15
1.10 Influence of grain size on the Hertzian damage: optical micrographs of half-surface and section views of indentations on aluminas with different grain sizes 16
1.11 Scheme of the contact strength test: parallel strip subjected to compression by opposite rigid cylinders 18

2.1 Scheme of the tape casting processing for thin ceramic sheet production . . . 22
2.2 Scheme of the A/AZ and A/2AZ samples lamination 22
2.3 Photography of the A/AZ multilayered material. Dark layers are the alumina ones, clear layers the alumina-zirconia ones 23

2.4 Microstructure of the interface between A (left) and AZ (right) layers. Zirconia grains appear as white for the higher atomic weight of zirconium with respect to aluminium 25

2.5 Typical *P-h* curve obtained by instrumented nanoindentation 26

2.6 a) Young modulus and b) hardness as a function of the penetration depth under instrumented indentation 27

2.7 Scheme of fracture toughness measurement by Vickers indentation 28

2.8 Residual stress distribution, as calculated by Finite Element analysis 29

2.9 AFM of the indentations imprints produced with a Berkovich indenter in alumina (a) and A/AZ laminated composite (b), with a total penetration depth of 1 μm. Arrows in the alumina image show the existence of radial cracks. 31

2.10 a) Residual stresses linear map measured by piezo-spectroscopy on the cross-section of A/AZ and A/2AZ multilayers, b) theoretical calculation of near-edge stress 32

2.11 Scheme of Spherical indentation 33

2.12 Scheme of the sample holders employed in the spherical indentation tests, which allow accurate placement in both axis 34

2.13 Typical staircase plot for the determination of critical load P_c for ring cracking. Empty symbols mean no visible damage, filled symbols mean detectable ring crack 35

2.14 Scheme of the types of loading tested: a) monotonic, b) cyclic and c) static . 36

2.15 Scheme of the sectioning techniques employed for damage evaluation: a) cut-and-bond, b) transverse sectioning, c) parallel grinding 37

2.16 Example of grinding-enhanced quasi-plastic microcraking after application of the transverse sectioning technique 38

2.17 Phases of residual strength measurements: a) indentation, b) bending 39

2.18 Normalized stress σ_x under contact strength test at the surface (a) and along the axis (b) for different values of the contact zone width $2s$ 41

2.19 Scheme of the contact strength testing 41

3.1 Meshes employed in the residual stress evaluation of the stress map a) near the edge, b) in the center and c) on the surface, respectively, representing one eight of actual samples. In c) the symbology and the symmetry axis are also reported 46
3.2 3D maps of a) the σ_{xx} and b) the average pressure present on the sample . . 47
3.3 Center (squares) and near-edge (circles) stress maps, resulting from FE analysis. The former are presented as the σ_{xx} component, the latter as the average pressure $1/3\Sigma\sigma_{11}$ 48
3.4 Uniaxial stress relaxation for the free surfaces at the edges along the a) x and b) y directions, both normalized over the sample width b, for $y = 0$ and $x = 0$, respectively 48
3.5 Mesh of the model for the cone crack equilibrium geometry. The crack is represented as straight, the indenter as a rigid sphere 50
3.6 Mesh of the 3D model of bending test; in small a detail of the mesh at the cone crack is shown 51
3.7 Typical mesh of the model for contact strength evaluation, with a detail of the contact zone 52
3.8 Flow diagram of the Python automatic incremental model of crack propagation 53
3.9 Scheme of flat punch indentation 54
3.10 Initial geometry of the flat punch model. r_0/a, P, δc are user-defined input 55
3.11 a) Mesh of a well-developed crack and b) mesh refinement with collapsed nodes for the stress intensity factors measurements at the crack tip 56
3.12 Collapsed vertex nodes and moved midside nodes for representing the crack tip and the strain singularity of perfectly elastic materials 58
3.13 Typical evolution of the stress intensity factor K_I with the cone crack propagation. Arrows indicate increments in load 59
3.14 Fracture energy as a function of the crack length for a range of starting radii, a) from the presented FE study and b) as extracted from the cited work . . 61

4.1 Contours of normalized K_I as a function of the relative crack depth c/a and position r/a 64
4.2 Scheme of semi-elliptical crack, origin of the ring crack under Hertzian indentation 65

4.3 Indentation load against time or number of cycles under a) stress corrosion cracking and b) cyclic fatigue tests. Empty points indicate no apparent damage, filled points the existence of well-developed ring crack 67

4.4 Comparison between the damage evolution under static and cyclic loading, represented as applied load against equivalent time, for the A/AZ laminated composite. 68

4.5 Optical pictures of typical ring cracks of A/AZ material produced under: (a) static loading and (b) cyclic loading. Ring crack in panel (b) is not perfectly circular and regions of grain bridging are visible. 70

4.6 SEM pictures of typical ring cracks of A/AZ material produced under: (a) static loading and (b) cyclic loading. The crack in panel (a) is smooth, while in panel (b) the grain removal typical from fatigue mechanisms of ceramics is evident. 70

4.7 Cyclic loading tests of A/AZ laminate composite with: (a) difference between maximum and minimum load constant, with maximum applied load against number of cycles; (b) constant maximum load, with ΔP against applied number of cycles. 73

4.8 Damage produced in A/AZ and MA by Hertzian fatigue tests under load of 500 N and different numbers of cycles. Although A/AZ has a better resistance to appearance of ring crack, it presents an apparent higher surface degradation (chipping) for severe conditions (N = 10^5 cycles). 74

4.9 Scanning electron microscope pictures of the alumina layer in A/AZ composite showing: (a) damage zone underneath the indenter, where the severe microcracking produced by shear loading can be appreciated (b) undamaged microstructure of the same material far from the indentation site. Both pictures have been taken at a depth of 50 μm from the surface. 75

4.10 Damage present in the MA and A/AZ materials as a function of the depth (z) for an applied load of 500 N and 10^4 cycles. It can be appreciated that in the MA a cone crack is formed, whereas in the A/AZ it exist both ring crack (partially developed into cone crack) and quasi-plastic damaged, as it can be appreciated in z = -10 μm, where the ring crack is marked with (1) and the quasi-plastic damage is marked with (2). 77

5.1 Scheme of mode-II grain bridging: intergranular friction (points 1,2 and 3) acts against the shear stress σ_P, producing a reduction of the kink angle from β to β' 80
5.2 Comparison of the crack paths obtained with the kink criterion from Eq. (5.3) and (5.5), respectively, normalized over the contact radius a 81
5.3 Influence of the microstructural coefficient λ on the crack path, for arbitrary values of the remaining variables. It can be seen that such coefficient is irrelevant in the path definition. 82
5.4 Crack paths obtained by varying the coefficient K_{II}^{∞} (expressed in $MPa\sqrt{m}$) for a constant $K_I^{\infty} = 2.0 \quad MPa\sqrt{m}$. Each path presents a constant angle, meaning that the discontinuity in the lower term of eq. (5.5) does not affect the crack trajectory 84
5.5 Cone crack angles as function of K_{II}^{∞}, for various values of K_I^{∞} (expressed in $MPa\sqrt{m}$) corresponding to different crack lengths 85
5.6 Scheme of slanted crack on a semi-infinite plate, whose stress intensity factors approximate the effect of residual stress on the Hertzian cone crack. 87
5.7 Scheme of the influence of the residual stresses on the unstable mode-I stress intensity factor 87
5.8 Crack paths in alumina as functions of the normalized residual stresses parameter σ_r/p_0 88
5.9 Normalized angle variation, with respect to the unstressed counterpart, of alumina with various amounts of residual stress and of soda-lime glass. The zone of linearity is highlighted 89
5.10 Cone crack angle in presence of residual stress, presenting a progressive decrease during unstable propagation and a constant value when stability is attained 90
5.11 Micrograph of cone crack produced by Hertzian indentation ($P = 980\,N$, $\phi = 2.5\,mm$) on laminated material ($\sigma_r \approx -200\,MPa$) 91
5.12 Crack path obtained for MA, A/AZ and A/2AZ materials, considering the effect of crack shielding and residual stress on the crack propagation 92

6.1 Scheme of transversal flexural testing 94
6.2 Notation for the rigidity and stress calculation of a multilayer subjected to flexion 95

6.3 Normalized stress distribution on laminated A/AZ and A/2AZ, compared with an homogeneous material. σ^*_{eq} is the surface value, defined in eq. (6.2) . 96
6.4 Actual surface stress against equivalent stress in monolithic and laminated material. If the fracture stress is at the right hand of the crossing point, the laminate is weaker than the monolithic material. 97
6.5 Experimental strength degradation as a function of the indentation load of monolithic alumina (MA) and multilayered material (A/AZ) 98
6.6 Fracture energy at the tip of the cone crack on MA and A/AZ as a function of the equivalent stress from eq. 6.3 99

7.1 2D and 3D Schemes of the contact strength testing 102
7.2 Contact strength of monolithic alumina alumina/alumina-zirconia multilayer. Values from numerical (empty symbols) and Finite Elements (solid symbols) solutions are presented. 103
7.3 Electron Fractography of tested multilayer sample, showing that fracture started from the alumina surface layer. 103
7.4 Maximum x-direction stress as a function of the contact area. Values from a previous numerical calculation (circles) and from the present work (squares) 104
7.5 FE representation of the typical x-direction stress field in multilayered material, originated from the combination of residual stresses and testing stress fields 105
7.6 Normalized tensile stress in the surface of monolithic alumina and multilayer. The difference in the maximum values coincides with the compressive residual stress in the latter. 106
7.7 Tensile stress along the y-axis ($x/t = 0$) for monolithic and laminated materials under low load, a) and high load b). 107
7.8 Maximum tensile stress along the surface ($y/t = 1$) and the y-axis ($x/t = 0$) for a multilayer material as a function of normalized load σ_{eq}. 108
7.9 Influence of the thermal mismatch and of the tensile versus compressive stress ratio (labelled as t_1/t_2)on the critical normalized load σ^c_{eq} for the switching of the maximum location from y-axis to surface, on laminated materials . . . 109

A.1 Input request windows 124
A.2 One-to-three elements transition 132

Nomenclature

a	contact radius under spherical indentation
A	contact area
b	width of prismatic samples for bending tests
B	elastic variation coefficient in Hertzian indentation in presence of residual stresss
c	crack length
C	length of the virtual cone, whose truncation is the Hertzian cone crack
c_0	Initial crack length
d	grain size
E	Young's modulus
$(EI)^*$	composite flexural rigidity
f	load frequency in cyclic indentation tests
F	applied force in bending and contact strength testing
G	elastic strain energy release rate in fracture mechanics
G_c	critical fracture energy
h	penetration depth in indentation tests
H	Hardness
I_c	translation factor to define the equivalent time of cyclic fatigue testing
k	elastic mismatch coefficient
K_I	mode-I stress intensity factor (assumed at the crack tip)
K_I^{appl}	applied stress intensity factor
K_I^i	Hertzian stress intensity factor
K_I^r	residual stress-generated stress intensity factor
K_I^{sh}	crack shielding stress factor
K_{Ic}	fracture toughness
K_I^∞	Saturation value of the crack shielding
K_{II}	mode-II stress intensity factor

K_Φ	extrinsic contribution to the stress intensity factor
l	characteristic length of faults
l_1, l_2	rollers spans in bending testing
m	Paris law fatigue exponent
n	number of layers composing a multilayer
N	number of cycles in fatigue testing
p	maximum load-related fatigue coefficient
p	pressure
p_0	mean Hertzian pressure
p_{max}	maximum Hertzian pressure
P	indentation load
P_c	critical load for cracking in spherical indentation
P_{min}	minimum indentation load under cyclic fatigue tests
P_{max}	maximum indentation load under cyclic fatigue tests
P_Y	critical indentation load for the onset of quasi-plasticity
q	load amplitude-related fatigue coefficient
r	radius of the ring crack under spherical indentation
R	sphere radius for Hertzian indentation
s	contact zone in contact strength testing
S	stiffness under instrumented indentation
t	half-thickness of a prismatic bar
t_i	thickness of a layer of material i
t_{eq}	equivalent time
T	temperature
T_f	final temperature
T_i	initial temperature
Y	stress intensity factor geometry coefficient
z	depth
α	angle of Hertzian cone crack or coefficient of thermal expansion
β	kink angle
$\beta(\nu)$	area correction function in instrumented indentation
Γ	elastic constant in the relation between critical load and fracture toughness
$\Delta\nu$	stress-induced shift of the Raman bands
ϵ	strain

θ	radial coordinate of the ring crack
κ	normalization coefficient in simulation of Hertzian indentation
λ	microstructural parameter in R-curve
μ	position and size function for stress intensity factor of a short crack under Hertzian indentation
ν	Poisson's ratio
ξ	elastic scaling coefficient for the maximum stress in multilayered materials
Π_{ii}	trace of the piezo-spectroscopy matrix
σ^*	fracture stress under strength testing
σ_{eq}	equivalent stress in inhomogeneous materials
σ_{ii}	first invariant of the stress tensor
σ_r	residual stress
σ_y	uniaxial compression yield stress
τ_m	maximum shear stress under spherical indentation
τ_y	shear yield stress
ϕ	indenter radius
χ	geometry coefficient for Vickers or long-crack Hertzian stress intensity factors

CHAPTER 1

Introduction

1.1 Advanced ceramics for structural applications

Ceramic materials are widely and increasingly used in many industrial fields, where their excellent properties, either mechanical, thermal, tribological or biological, are needed for advanced, high-performing applications.

Some examples are given by silicon carbides and tungsten carbides, which present, in general terms, low weight and high hardness and or by mullite, excellent for its thermal shock resistance, or alumina and zirconia, whose bio-compatibility and wear resistance are unmatched by almost any other material.

However, their intrinsic brittleness and, specially, lack of reliability are obstacles to further spreading of many of these materials in those applications in which structural resistance is required.

In order to overcome the risk of catastrophic failure, the use of ceramic materials is often limited to small parts of the component, in which they can fulfill their function without affecting the piece reliability. This is specially true for those applications in which the required properties are related to the surface, such as the tribological or biomedical ones, in which, on the other hand, it is impossible to avoid the ceramic to be loaded, either accidentally or for fulfilling the expected function.

The development of fracture mechanics as a design discipline enlightened the importance of the microstructure and of the surface flaws on the fracture response of brittle materials, allowing many advancement in the effort of improving the reliability of ceramics, acting either on the processing parameters (reducing thus the flaws), on the

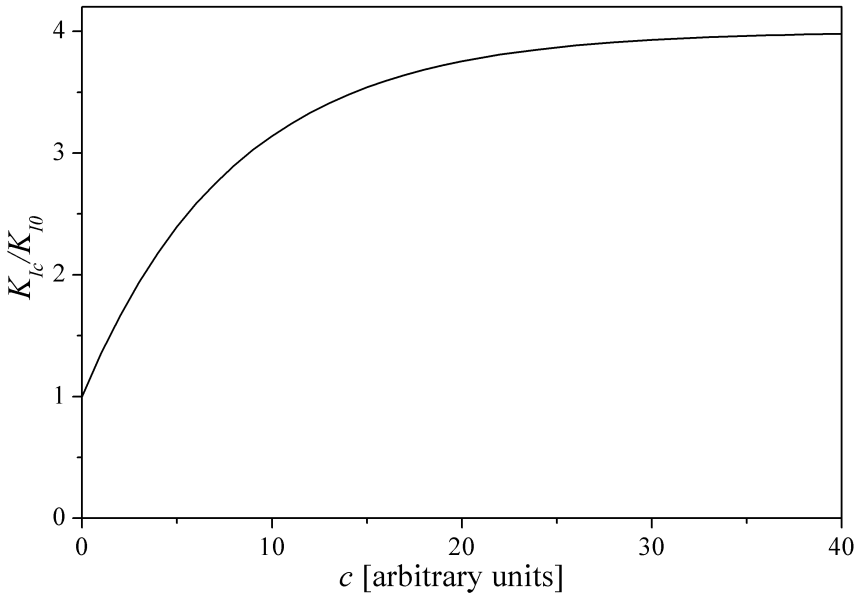

Figure 1.1: Scheme of crack length-dependent toughness, or R-curve

microstructure, or on extrinsic mechanisms.

1.2 Shielding microstructures

An example of microstructure-dependent toughening mechanism is the increasing crack-growth resistance, often referred to as "R-curve behaviour", present in many tough ceramics and caused by several different mechanisms.

In those ceramics, the fracture toughness does not have a constant value, but increases as the crack propagates, as it is shown schematically in Fig. 1.1. The mechanisms causing such effect act either in a *process zone*, as in phase-transforming zirconia or micro-cracking zirconia-toughened alumina, or in a *bridging zone*, as in fiber-reinforced or coarse- and long-grained ceramics. In both cases, the microstructure applies a stress to the crack wake, hindering thus the crack opening.

In the case of alumina, cracks propagate following the high-energy grain boundaries, so that the friction between grains in the crack wake provides the stress shielding. Consequently, the amount of shielding can be related to the grain size and aspect ratio, being higher in coarse-grained materials, although bridging can be present in fine-grained material.

In general terms, the R-curve can be expressed as a term which is subtracted from

the stress intensity factor at the crack tip, as a function of the crack length c:

$$K_I = K_I^{appl} - K_I^{sh}(c) \tag{1.1}$$

The expression of K_I^{sh} depends on many factors, such as the material microstructure, the type of test, the initial crack length (or defect) and the intrinsic fracture toughness K_{Ic} assumed, but in general is formed by a steady state and a transient one, which depends on the crack length and on some microstructural parameter [1].

An important consequence of the R-curve is that crack advancements are accompanied by a reduction of the applied stress intensity factor, so that a load increment is necessary for a further crack advancement, so that the crack propagation is stable (*i.e.* $\Delta K/\Delta c < 0$).

1.3 Layered structures

To build a multilayered structure is another way which is being followed in the effort to increase the reliability of ceramics. As it is common in composite materials, layered materials allow to tailor the mechanical properties to be superior to those of the constituent materials, by means of different strengthening mechanisms.

1.3.1 Multilayers with weak interfaces

The concept of crack deflection is borrowed from the mollusc shells [2], which are formed mainly by brittle aragonite (calcium carbonate) layers, separated by thin protein films. When a crack propagating through a hard layer reaches the interface, it is deflected along the interface itself, dissipating energy and increasing thus the work necessary for fracture (see Fig. 1.2).

Hence, SiC laminates with weak graphite interfaces fabricated by chemical vapour deposition [3] obtained the same effect of crack deflection, which produced an increment in the work of fracture (at the expense of a slightly lower ultimate strength), with the additional virtue of reducing the catastrophic character of the fracture mechanism. In other words, the area under the stress-strain curve is higher, because the fracture of the first layer does not cause the failure of the sample, which can withstand higher displacement. For this reason, such mode of fracture is called "graceful failure".

Other examples of this design philosophy presented layers of SI_3N_4/Si_3N_4-BN, produced by Kovar *et al.* [4], who studied the dependance on the interlayer resistance of

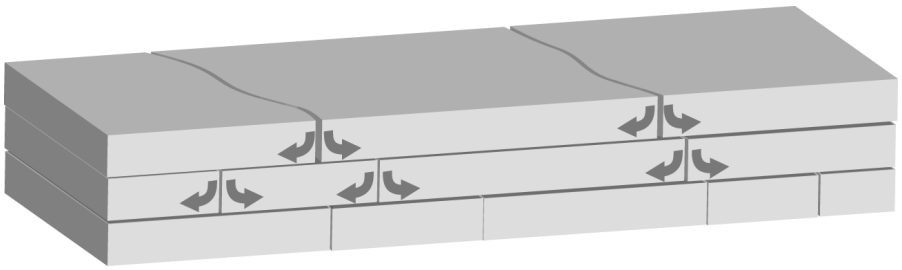

Figure 1.2: Scheme of crack deflection along the weak interfaces in ceramic laminates. The arrows represent crack deflection/bifurcation

the mode of failure, either graceful delamination or brittle failure; $Al_2O_3/LaPO_4$ [5] and $ZrO_2/LaPO_4$ [6] exploited the combination of debonding properties with chemical and morphological stability of lanthanum phosphate, known in nature as monazite.

The drawback of such composites is the low resistance of the interfaces to shear stress, which is detrimental for the multilayer resistance to mixed-mode loading.

1.3.2 Multilayers with strong interfaces

The limitations of the laminates with weak interfaces were partially overcome by alternative laminate structure with stronger interfaces or layers, such as porous alumina between dense alumina layers [7], which provided high work of fracture enhanced at high temperature; unsinterable-platelets-enriched alumina (or mullite) [8], which causes residual porosity, so that crack propagation takes place along a preferential, longer, path; transforming Ce-ZrO_2 and alumina, in which the toughening was given by the influence of the alumina layers on the transformation zone surrounding the crack, which is spread along the interface and truncated at the tip, with the consequence that the crack closure stress is higher [9].

A particular case of this class of composite ceramics is the structure composed by thick layers with small tensile residual stress alternated to thin layers subjected to high compressive residual stress, which cause the crack to arrest and be deflected, so that a threshold-stress effect is achieved [10, 11], meaning that the component strength does not depend on the flaw size, for a wide range of sizes.

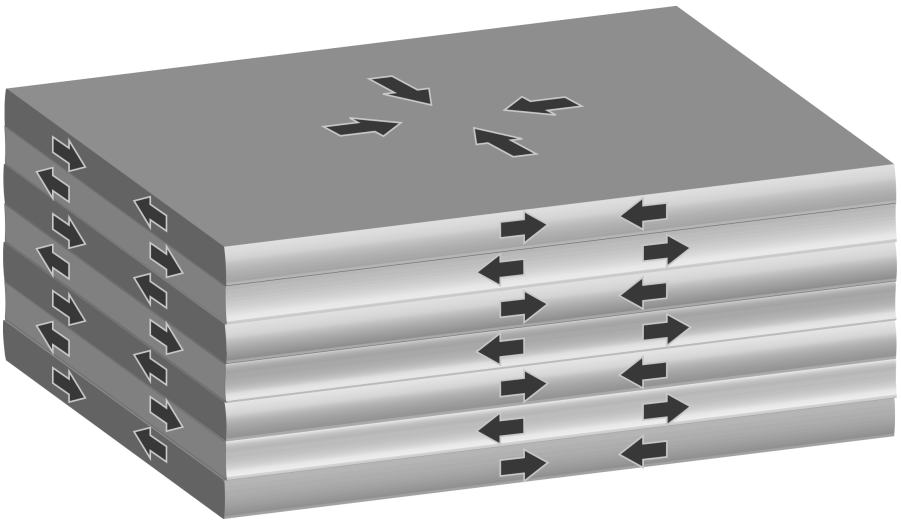

Figure 1.3: Scheme of residual stress generated in multilayered ceramics from differential shrinkage after sintering. Gray layers represent the ones with lower α. The deformation at the edges has been exaggerated.

1.4 Ceramic laminates with residual stress

Stacking and sintering layers of materials with different coefficients of thermal expansion α, results in the generation of residual stresses in the structure, such as the ones represented in Fig. 1.3. The amount of residual stress depends on the geometry and elastic properties of the composing materials. An analytical approximation, considering only in-plane stress, was formulated by Chartier *et al.* [12]:

$$\sigma_r^1 = \frac{nE_1E_2t_2(\alpha_1 - \alpha_2)\Delta T}{n(1-\nu_1)E_2t_2 + (n+1)(1-\nu_2)E_1t_1} \tag{1.2}$$

for a $(2n{+}1)$-layered structure, and the symbols are described in the nomenclature section (p. xvii).

In some case, residual stress can be induced by the use of a transforming material, typically zirconium oxide, as one of the composing material, due to the volume increment [10, 13] (4% for the tetragonal to monoclinic transformation of zirconia). Ceramic laminates are often produced in the alumina-zirconia system, because both materials present excellent properties for tribological and biological applications and can be combined easily, so that the residual stress can be tailored in a wide range of values by using an alumina-zirconia composite as one or both of the composing material, or by modifying the relative thickness of the layers, so that the stress that is generated does not cause failure of the samples during sintering (the so-called "channel cracking" [14]).

Moreover, the bonding created during sintering between layers is strong and with almost no particle interdiffusion.

The strengthening mechanism in such structures is given by the compressive residual stresses acting on the external layer. Such compressive stresses have the effect of reducing the externally-applied stress, increasing thus the material strength or, which is the same, reducing the stress intensity factor at the tip of the existing defects or cracks.

The strength of such composite is improved, with respect to the monolithic counterpart, under bending tests [15], as well as the fracture toughness [16]. Moreover, the force applied by residual stress on the crack wake increases as the crack propagates, because more surface of application if formed, producing an increase in toughness, in other words an apparent R-curve behaviour, as it was shown experimentally [17] and studied by the weight function method [18, 19].

Ceramic laminates with residual stresses have shown enhanced properties also under wear testing [20], with both reduced friction coefficient and increased wear resistance. This result is especially significant, because it is obtained under conditions which are similar to the ones expected in service.

Despite all the noteworthy advancement it is apparent that ceramic materials do not present, currently, the characteristics of reliability, high toughness and ease of processing, which would allow the spreading to real structural applications.

The best design philosophy is, indeed, trying to employ ceramics, either monolithic or in a composite structure, where they are most needed, exploiting their excellent properties and avoiding remote loading. For this reason one of the main characteristics of this class of material should be the resistance to localized loading.

Consequently, damage tolerance against long crack propagation is somewhat not connected to the response of the material under the type of loading expected in service; in order to obtain a proper characterization, new tools are needed, which are different from the classical mechanical tests, such as those provided by spherical indentation.

1.5 Spherical indentation theory

Spherical indentation presents several advantages compared to other testing tools:

- it is material inexpensive: as with many indentation tests, small samples are needed, several indentation can be performed on the same sample (provided that

they are placed far enough one from the other, to minimize the influence on the neighboring) and the samples can be tested on both surfaces;

- compared to sharp indentation, the stress field is elastic at the beginning, with the the maximum stress increasing with the contact load, until plasticity is reached in a point beneath the indenter, which expands as the load increases. It is possible, therefore, to employ spherical indentation techniques to study the fracture in elastic regime or the transitions (either elasto-plastic or related to any stress-induced transformation) taking place in the material;

- it allows testing under different loading conditions, enhancing thus different deformation or fracture mechanisms; as an example, tests on ceramics with a constant load enhance environment-assisted subcritical cracking, while cyclic fatigue produces mechanical degradation of the bridging mechanisms, resulting, similarly, in stable crack propagation, and also in subsurface microcracking;

- as mentioned above, the highly graded and inhomogeneous stress field is representative of the loading which can be expected during service, as in tribological and biomechanical applications;

- is suitable for the evaluation of several types of materials, therefore it can be used as a comparison tool, although the most relevant results are obtained by testing brittle materials or composite structures, such as coatings or multilayers.

The first studies of the elastic stress and deformation fields formed during the contact of two blunt bodies were presented by Hertz [21], who observed the contact between two glass lenses and the modifications of the Newton refraction pattern due to the elastic deformation. He established the basis of the spherical indentation cracking analysis, calculated the stress trajectories and observed the brittle damage in the shape of the characteristic cone crack.

The elastic calculations of the contact, corresponding to the diagram of Fig. 1.4, are here expressed in the form established by Johnson [22]:

$$a^3 = 4kPR/3E \tag{1.3}$$

being a the contact radius, P the indentation load, R the sphere radius, E the Young's modulus, and

$$k = \frac{9}{16}\left[(1-\nu^2)+(1-\nu'^2)\right]\frac{E}{E'}$$

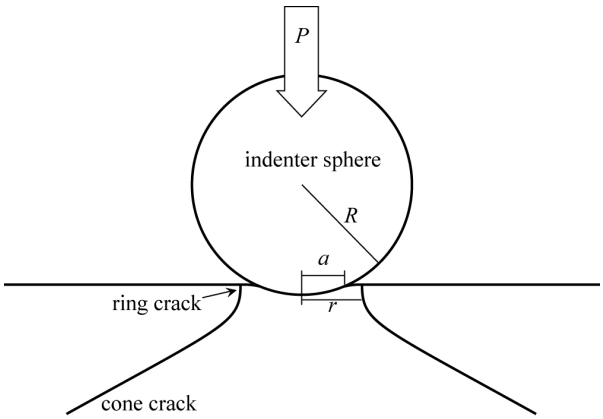

Figure 1.4: Scheme and symbology of Hertzian cone cracking

a dimensionless elastic mismatch coefficient, with ν the Poisson's ratio and the prime denoting the indenter material.

The contact pressure follows a radial distribution:

$$p(r) = p_{max}\left[1 - \left(\frac{r}{a}\right)^2\right]^{1/2} \tag{1.4}$$

where p_{max} is the peak pressure, located under the indenter vertical axis and related with the mean pressure p_0:

$$p_0 = \frac{2}{3}p_{max} = \frac{P}{\pi a^2} \tag{1.5}$$

Eqs. (1.3) and (1.5) can be combined:

$$p_0 = \left(\frac{3E}{4\pi k}\right)\frac{a}{R} \tag{1.6}$$

producing a relation between indentation pressure and relative deformation, which gives information on the stress-strain response of the material, shown in Fig. 1.5 for a brittle and a plastic material. In 1891 Auerbach [23] studied the onset of damage and established the law bearing his name, which states a linear dependance of the critical load for fracture on the indenter radius (or on $R^{3/2}$ in the case of flat punch indentation [24]); this is an unexpected behaviour, often referred to as a paradox, because it states that fracture does not start when a critical stress is reached, which would be R^2-dependant (Fig. 1.6). In 1956 Roesler [25] showed that $P \propto C^{3/2}$ for long-enough cracks, putting the basis for the Fracture Mechanics analysis made in 1967 by Frank and Lawn [26, 27], who could explain the Auerbach's paradox with an energy balance based on the separation in two phases of the damage formation process, ring and cone crack formation,

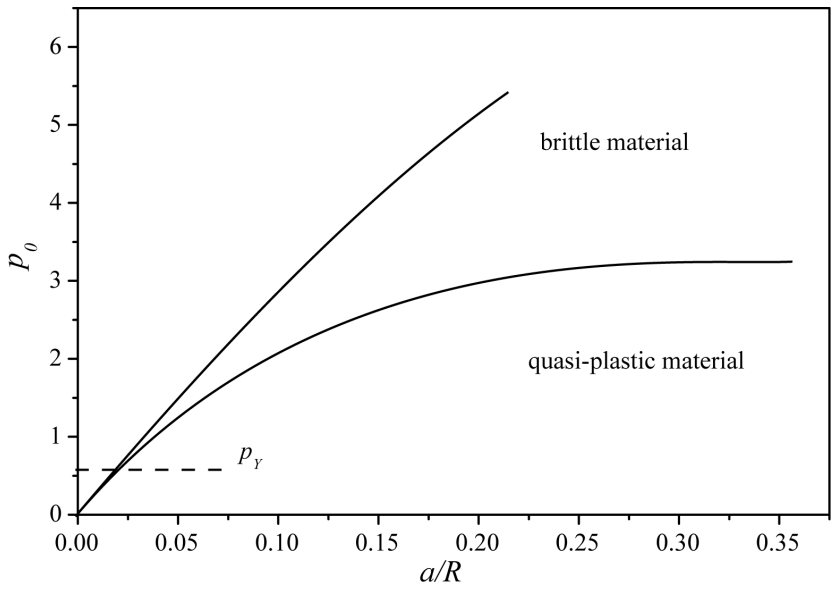

Figure 1.5: Scheme of indentation stress-strain curve

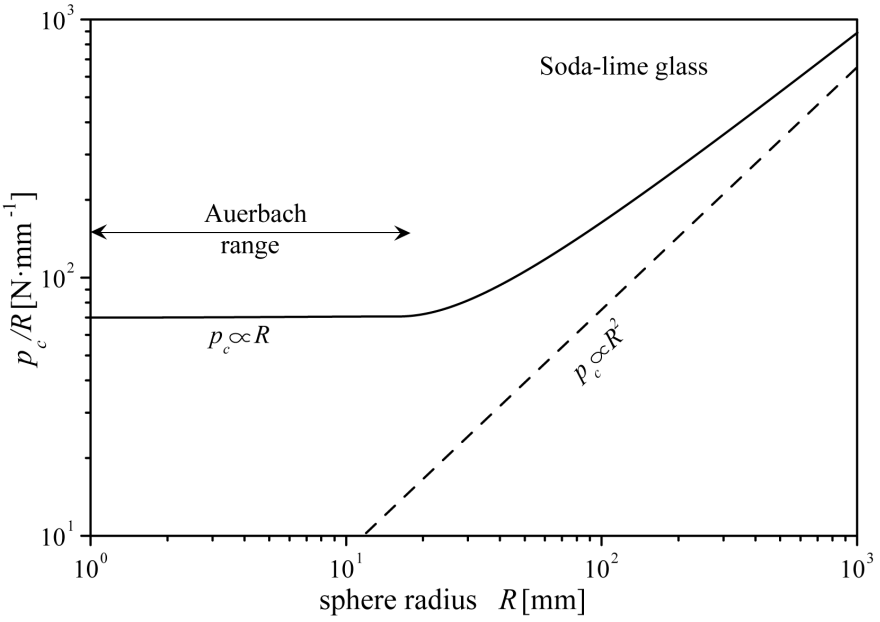

Figure 1.6: Scheme of the Auerbach paradox

respectively. The fracture mechanics approach allowed to express the evolution of the K_I shape along the crack, though in an approximate way[1].

A three dimensional generalization of the in-plane fracture mechanics analysis was provided, in more recent years, by Dai *et al.*, as a study of the tendency to propagate either downward or circumferentially of a semi-elliptical crack subjected to the Hertzian stress field [28]. Recently, Licht *et al.* extended such analysis to general validity with the aid of weight functions and added a statistical analysis via a modified Weibull theory [29].

Several factors which may influence the onset of ring crack were analysed, such as the effect of reactive environment, by Langitan and Lawn [30] in 1970; the influence of elastic mismatch and friction coefficient between substrate and indenter by Johnson, O'Connor and Woodward in 1973 [31], and the effect of Poisson ratio by Warren in 1978 [32], who also introduced the possibility of employing spherical indentation as a tool for measuring fracture toughness from the ring crack radius.

In more recent years, most of the basic issues of Hertzian cracking were analysed to a further understanding and in some cases improved. It is the case of the work by Mouginot and Maugis [33], who extended the Hertzian analysis to the indentation by a flat punch and reviewed the issues of crack initiation, abrupt propagation to form the cone and subsequent stable crack growing, of the Auerbach's law and of the starting crack radius.

In 1975 Lawn, Wiederhorn and Johnson studied the well-developed cone crack as the critical flaw for cracking under bending test, quantifying and rationalizing the strength degradation induced and indicating a parametric optimization for contact damage tolerant design [34].

The concept of indentation as a toughness measurement tool was reprised in 1992 by Zeng *et al.* [35], who proposed a methodology based on cone crack length rather than on onset of ring crack. On the other hand, this approach was improved later by Warren himself in 1995 [36], who reviewed critically the papers appeared on the topic. He highlighted and explained the poor agreement existing in literature, which may be attributed to the complexity of some of the methods and to the inaccurate simplifications often assumed. Eventually, he proposed an improved method based on the onset of ring cracking on a same-material substrate-indenter couple. The method was somewhat improved by Geandier *et al.*, who included the effect of friction between

[1] because the K_I were calculated from the stress field in the uncracked body

dissimilar materials [37].

1.6 Cone crack

The mechanism of cone crack formation and propagation is one of the main points this thesis deals with; for this reason it deserves special attention.

As mentioned above, tensile stress encircling the contact zone causes some favorably oriented defect to propagate circumferentially creating a ring crack. Further propagation needs a load increment, because the stress field below the surface becomes rapidly compressive. The shape of K_I as a function of the crack length, shown in Fig. 1.7, consists of two unstable branches and two stable ones. The former ones (1 and 3 in the figure) correspond to the abrupt ring and cone crack formation, respectively, which start when the critical stress intensity factor is reached, the latter ones (2 and 4) to stable propagation due to load increments. After stability is attained, long-enough cracks follow the Roesler equation:

$$K(c) = \chi \frac{P}{C^{3/2}} \tag{1.7}$$

being C the length of the virtual cone director, whose truncation is the Hertzian crack. Crack propagation, as it is common in ceramics, follows the direction of maximum energy release rate, or, which is the same for brittle materials, the direction of a disappearing mode-*II* stress intensity factor. It is possible to evaluate *a priori* the crack path from the stress field, as a path perpendicular to the first principal stress trajectory, in other words the third principal stress trajectory[2]. This method was followed by Frank and Lawn [26], who nevertheless obtained a realistic path for glass only assuming an unrealistic value of the Poisson's ratio. This is due to the modification of the stress field caused by the crack propagation.

Only in recent years the problem was addressed by Kocer *et al.* [38, 39] and by Fett [40], in the former work with an incremental Finite Element model in which the propagation direction was calculated step-wise by means of a minimum energy criterion at the crack tip, in the latter with weight functions, also derived by Finite Element modeling of parameterized cracks. Both authors obtained results in agreement with the experimental data collected for several brittle homogeneous materials, although discrepancy

[2]because the second principal stress is the hoop component

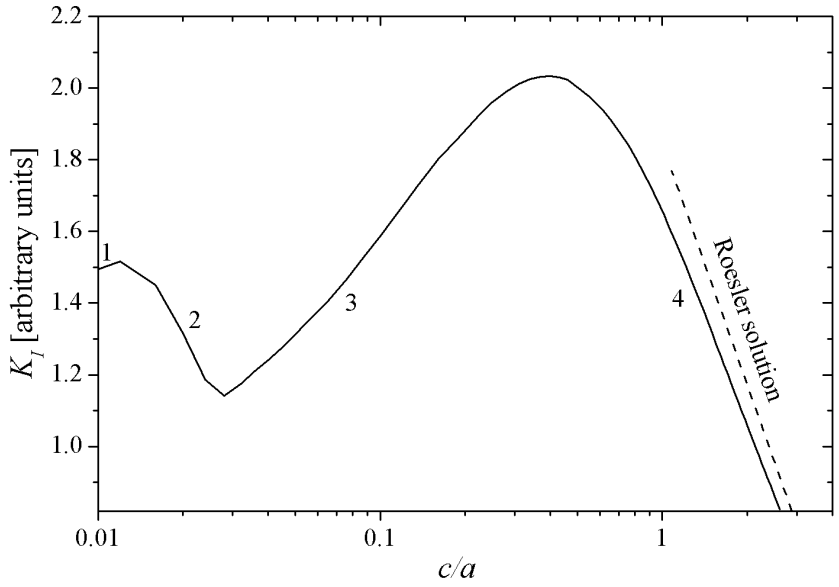

Figure 1.7: Stress intensity factor as a function of the crack length, with the asymptotical Roesler solution

existed for polycrystalline materials, such as alumina, in which microstructural features affect the stress field at the crack tip.

It is argued that such microstructural variables are not captured by models of crack propagation based on fracture mechanics on continuous bodies. This is the case of crack-growth resistance produced by grain bridging, common in coarse-grained alumina but also present in fine-grained alumina[41], as it can be appreciated, for example, in the disagreement in terms of final length in cone cracks between simulation and experimental observations [42]. The mode-II contribution from such effects sums to the shear stress component of the imposed stress field, producing thus a variation of the direction for which the shear stress disappears, in other words the $K_{II} = 0$ path.

There are not many studies in the literature about mode-II R-curve in brittle ceramics [43]. This is due in part to the experimental difficulties in making accurate measurements, respect to mode-I shielding, and to the fact that this latter is generally considered to have more influence on the fracture properties. Furthermore, under both mode-I and mode-II loading, the amount of shielding depends strongly on the type of test performed and on the mode-I/mode-II ratio, so that extrapolation of results from one test to another would give unreliable results. Therefore, an estimation of a mode-II R-curve under a specific type of test should be obtained by the same, or a very similar,

test. In the case of Hertzian indentation, for long enough cracks, fracture is essentially mode-I-driven, with a relatively small mode-II stress intensity factor, which rules the crack propagation. *A priori* knowledge of the K_{II} stress intensity factor is not available, so that a direct experimental measure is not attainable.

1.7 Inelastic contact damage

In 1994 Guiberteau *et al.* proposed the employment of spherical indentation as a damage indicator. They applied cyclic loading to fine-grained alumina, and tried to relate the amount of visible surface damage to the strength degradation of the material [44]. This latter point was deeply studied by Kim *et al.*, who performed a series of cyclic indentation-strength tests on several materials, deducting general laws of damage accumulation and highlighting the existence of mechanical fatigue effect enhancing both brittle and quasi-plastic damage [45].

Quasi-plasticity as a damage mechanism in brittle materials, although foreshadowed since the seventies [46], and deducible from the "indentation stress-strain" curve, was studied in deep only in the 1990s [47, 48]. Such type of damage presents several analogies with the deformation mechanisms in ductile materials, in that is cause of permanent deformation in typically non-plastic materials and is shear-driven. However, the microstructural mechanism is completely different, being not controlled dislocations movement. From a macroscopic observation, point damage starts beneath the indenter when the maximum shear stress τ_m, located along the symmetry axis, reaches the critical value $\tau_m = \tau_y = 1/2\sigma_y$; subsequent loading causes expansion of the damaged zone in a way phenomenologically similar to the "expanding cavity" model in soft metals.

Microstructural observations showed that the permanent deformation is caused by shear-activated microcracking, with extensile mode-I wings forming at the grain boundaries, which propagate and, for high load, coalesce resulting in disintegration of the material [49] and expansion of the affected zone until reaching the surface. Such mechanisms is enhanced by cyclic loading [50].

The exact onset of quasi-plastic yielding is difficult to measure, as permanent deformation starts under the surface; nevertheless it can be deducted from the loss of linearity of the indentation stress-strain curve, as shown in Fig. 1.5 [47] or, if the indentation response is recorded, by measurements of the residual depth as a function of the load and regression of an elastic recovery parameter to the value for which the residual depth

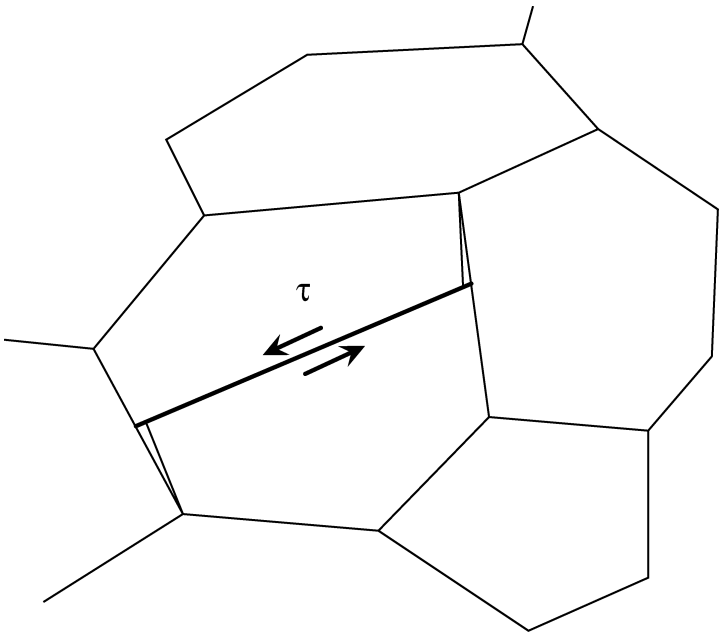

Figure 1.8: Scheme of shear-activated microcracks, with extensile wings at the grain boundaries

tends to 0 [51]. The amount of damage is quantified by a parameter Nl^3, where N is the density and l the characteristic size, respectively, of the faults. Measurement techniques which have given good results at least in relative amounts of quasi-plastic damage are acoustic emission detection [49] and thermal wave imaging [52].

Simulation-assisted representations of quasi-plastic damage gave acceptable results if constitutive laws typical of plastic deformation of metals were used and the non-linear deformation law were included in the material response rather than as an expanding cavity [53]. Nevertheless, an improvement was obtained by Licht *et al.* with a Finite Element model of damage which describes the development of pressure-induced microcracks in brittle solids as an elastic degradation of the material [54].

The prevalence of either brittle or quasi-plastic damage is related to the elastic and mechanical properties of the material, as well as to microstructural and extrinsic aspects. Predictions of the contact behaviour can be inferred from a predictive index, namely a critical loads ratio, proposed by Rhee *et al.* [55], based on the elastic properties and on the toughness of several materials.

$$P_Y/P_c = \Delta(H/E')(H/K_{Ic})^2 R \tag{1.8}$$

with Δ a constant which is a function mainly of the Poisson's ratio.

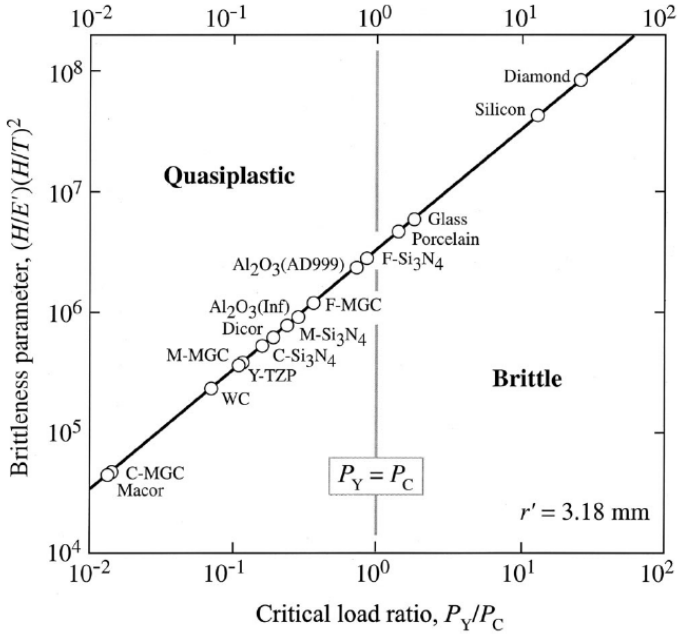

Figure 1.9: Calculated critical load ratio for selected ceramics, for a sphere radius R=3.18 mm [55]

As it can be seen in Eq. 1.8, a smaller indenter will be more likely to cause inelastic deformation rather than fragile cracking. This is due to the fact that the critical load for plastic onset has a quadratic dependence with the indenter radius, while the onset of brittle fracture grows with the radius in the Auerbach range. The results obtained in this work, shown in Fig. 1.9, though useful for an approximative *a priori* evaluation, have the limitation of assuming ideal elastic-plastic response, neglecting any microstructural feature, which often are relevant in defining the damage mode. Moreover the index predicts the onset of the first damage, but both modes of damage can coexist in the same material (especially polycrystalline ones) for higher loading.

The influence of the microstructure can be seen in the studies of Guiberteau *et al.* [44, 49], Lee *et al.* [56, 57], Latella *et al.* [58] who observed that coarse-grained ceramics (alumina, silicon nitride, Ce-TZP, respectively) present higher accumulated plastic damage than in fine-grained materials, which present the classical Hertzian fracture. Such influence can be appreciated clearly in the micrographies presented in Fig. 1.10, taken from [49]. Padture *et al.* observed a similar behaviour, i.e. an enhancement of quasi-plastic damage with respect to brittle cracking, in presence of weak interfaces [59].

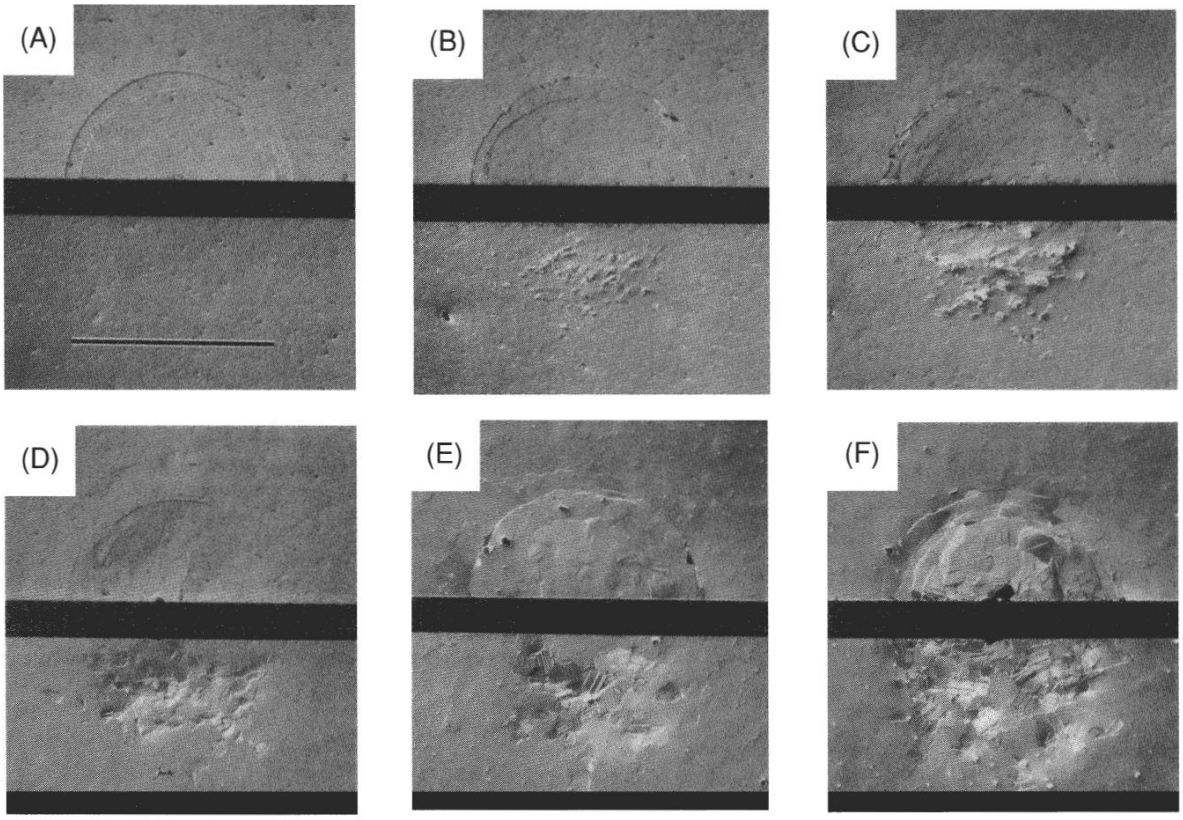

Figure 1.10: Influence of grain size on the Hertzian damage: optical micrographs of half-surface and section views of indentations on aluminas with grain size (a) 3 μm, (b) 9 μm, (c) 15 μm, (d) 21 μm, (e) 35 μm, (f) 48 μm [49]

Although the contact damage generated by Hertzian indentation is localized in a small volume, the material subjected to elastic deformation is much greater, therefore any feature of the component affecting such volume may influence the damage formation and how such damage affects the material strength. Giannakopoulos [60] and Jitcharoen *et al.* [61] showed, both analytically and experimentally, that in presence of an elastic gradient, increasing from the surface to the bulk of the sample, the cone crack formation can be inhibited. Since this is due only to the different shape of the elastic field, the quasi-plastic damage is not enhanced, as it could be expected.

Similar improvements can be obtained in laminated structures, in which layers with different elastic or microstructural properties interact, with the effect of reducing the amount of damage generated by spherical indentation. An *et al.* produced trilayered materials with layers of different microstructure (homogeneous fine-grained alumina and heterogeneous alumina, respectively), piled in two opposite sequences, which behave as

constraint to the damage propagation in the adjacent layer, with a consequent lower strength degradation under spherical indentation [62].

More often the combination of a brittle and a compliant materials has been studied, for example by Lee *et al.* and Miranda *et al.*, who proposed a hard coating-soft substrate coupling as a tough, contact damage-tolerant system [63, 64]. The concept was further developed by Jung *et al.* and Lawn *et al.* as a way to improve the reliability of all-ceramic crowns for dental implants [65, 66]. The use of Hertzian indentation in this case is an especially effective example of application-focused testing: the loading of a dental implant is well represented by spherical indentation, therefore from such tests the component design can be directly derived.

The quantification of the amount of damage generated by spherical indentation can be obtained from measurements of the strength degradation with respect to undamaged material. Both the brittle and quasi-plastic modes of damage can act as the critical flaw for fracture under bending test, although the way a material degrade, as a function of the indentation load or of the number of cycles in the case of contact fatigue testing, varies, as shown by Lee *et al.* in silicon nitride [63] and by Kim *et al.* in fatigued ceramics [45]. If damage is prevalently brittle, the drop in strength is abrupt, corresponding to the formation of cone crack (whose stable length is of the order of magnitude of the contact diameter) and increases slowly as the cone crack propagates in a stable way, either for the increase in load or in number of cycles. If damage is quasi-plastic there is no strength drop, and the degradation is progressive, corresponding to the progressive growth and coalescence of the microcracking.

1.8 Failure caused by contact damage

Although damage produced by spherical indentation is often contained within a shallow volume beneath the indentation, it can cause failure of the component. Evaluation of such surface-related strength can difficultly be attained by traditional strength testing methodologies, because the stress gradient is multiaxial and highly inhomogeneous, rather than the monoaxial homogeneous characteristic of bending tests, which therefore are not appropriate for a strength characterization focused on contact-prone applications.

The loading by opposite spherical contact, for example, causes failure when the cone cracks either meet each other or reach the sample edge. Such test is suitable also for

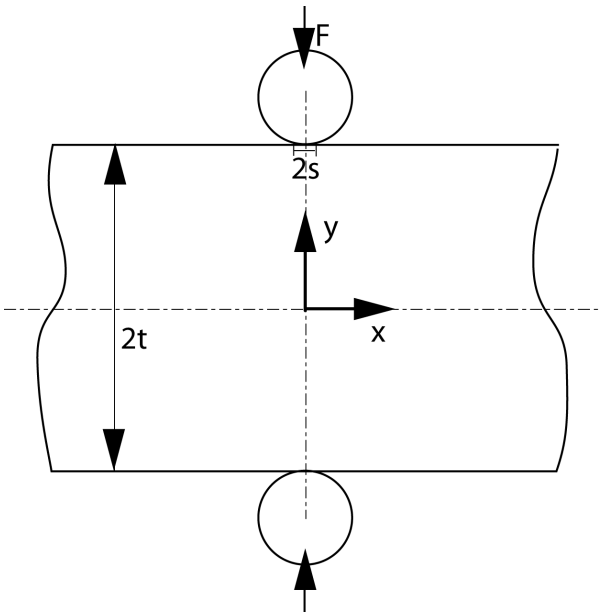

Figure 1.11: Scheme of the contact strength test: parallel strip subjected to compression by opposite rigid cylinders

fatigue crack propagation analysis [67, 68].

An alternative test setup is the contact strength test by opposite cylinders loading: compression applied in such a way generates a Hertzian stress field, similar to the one generated by sphere, with the first in-plane principal stresses tensile and the second negative, the former presenting maxima at the surface near the contact zone and along the vertical axis of symmetry, which causes unstable crack growth and failure of the sample [69].

1.9 Objectives of the thesis

The main focus of this thesis was the characterization of ceramic laminates response to contact loading.

For the sake of completeness and readability, the approach was to divide the work in several sections, with increasing levels of damage, from the first appearance of cracks on the surface to the degradation of the specimen, leading to catastrophic failure.

The laminates herein studied were designed with the aim of improving the performances in surface-related applications, such as tribological and biomedical, therefore the first characterization parameter was the appearance of damage in the surface, which is

a critical issue because is the cause of loss of functionality. The study was conducted trying to embrace a range of modes of testing, which represent loading expectable in service.

Single-cycle loading was the first to be characterized, as a reference test and as model of incidental loading. The results obtained were then extended to long-lasting (static fatigue) and cyclic loading, the former for an evaluation of the environment-enhanced fracture, the latter for an estimation of mechanical fatigue effect.

Cyclic loading was also employed in the next step, the evaluation of the surface degradation caused by more severe loading. The importance of this issue lies in the additional damage which can be caused by debris or material chips detaching from the component.

A major point of research was the study of the cone crack propagation. The knowledge of the subsurface damage in ceramic laminates acquires a special importance, in that containment of the crack within the external layer is extremely critical for avoiding abrupt failure, as it would occur if the crack extends to the subsequent, tension-stressed, layer.

Many features are involved in the fracture properties of ceramic materials; the manufacturing process itself influences properties such as density and grain size, on which the resistance of the material depends strictly. Moreover, the extraction of properties often depends on the specific test methodology and, in the case of laminated materials, it is difficult to isolate the effect of the geometry on the test from the actual effect on the material resistance.

To overcome this limitations, and obtain thus general relations of the modification in the fracture response, the Finite Element method was used in order to take into account all of the intrinsic and extrinsic parameters involved in the mechanical properties of ceramic laminates, namely microstructure-dependent toughness and residual stresses, and infer the net effect of any of the issues, rather than measuring a geometry-dependent improvement, obtaining thus general laws applicable to any material and composite geometry. Simulations were tightly associated with actual tests, in order to produce as quantitative as possible relations.

Although the objective of the thesis was the study of surface and sub-surface damage, the effect of such damage on the strength of the materials studied was also analyzed. The strength degradation from cone cracking was examined for some specific case of ceramic laminates with the aid of the Finite Element methods.

Contact loading, if high enough, can cause by itself failure of the material. This mode of failure was studied by means of an innovative test methodology, which was adapted for ceramic laminates testing. In this case as well, general relations, aimed to improve the design of application-focused laminated materials, were extracted.

The philosophy followed throughout the development of the research was to start from a specific case and, with the aid of numerical techniques, trying to infer conclusions as general as possible on the response to the given test/loading, with special attention to the possibility of improving the design of ceramic laminates towards a higher application-dependant reliability.

CHAPTER 2

Experimental Methods

2.1 Material processing and preparation

All the materials studied were manufactured at the Institute of Science and Technology for Ceramics (ISTEC), Faenza, Italy. Even though the processing was not directly included in the study by the author, it deserves mentioning because it affects strongly many of the properties to be studied.

To obtain the ceramic sheets suitable for the preparation of laminated composites, two powders were used:

- high purity (99.7%) alumina (Alcoa A16-SG, Alcoa Aluminum Co., New York, USA) with an average particle size of 0.3μm,
- tetragonal zirconia polycrystals (TZ3Y-S, Tosho Corp., Japan) containing 94.7% of ZrO_2 and 3 mol% of Y_2O_3 (usually referred to as 3Y-TZP) with an average particle size of 0.3μm

The different powders were mixed with organic binders, dispersant, plasticizers and solvents to obtain suitable slips for tape casting. After mixing with organic components, the slurry containing the ceramic powders was tape casted onto a mylar sheet moved at a constant speed of 200 mm/min (Fig. 2.1. Details on this technique can be found elsewhere [70].

Sheets of pure alumina (hereinafter designated as "A") as well as of the composite alumina-zirconia (hereinafter designated as "AZ") in the volume ratio 60/40 were

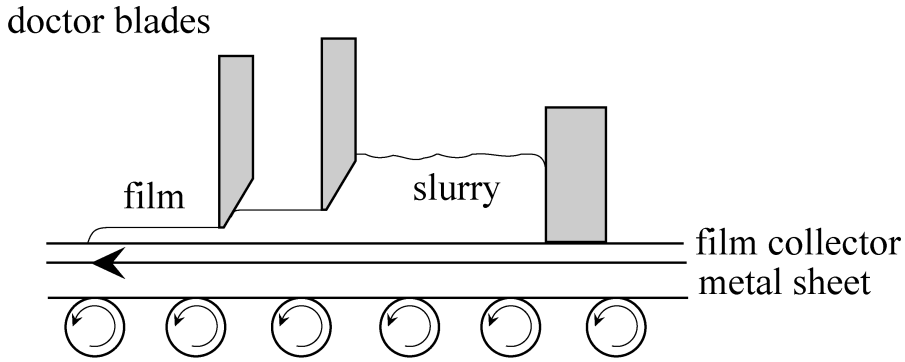

Figure 2.1: Scheme of the tape casting processing for thin ceramic sheet production

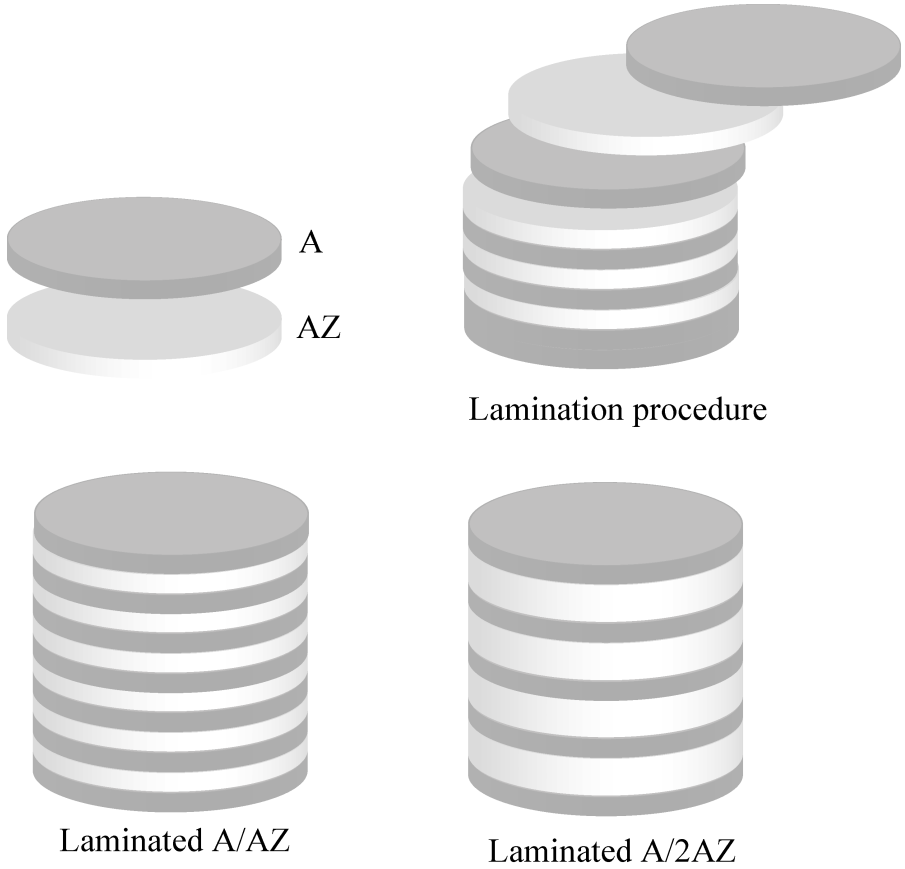

Figure 2.2: Scheme of the A/AZ and A/2AZ samples lamination

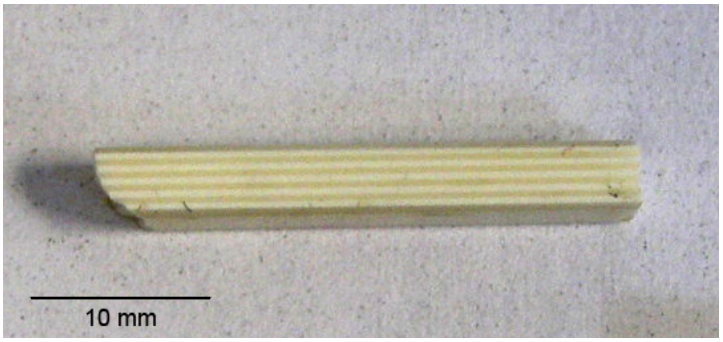

Figure 2.3: Photography of the A/AZ multilayered material. Dark layers are the alumina ones, clear layers the alumina-zirconia ones

prepared. The thicknesses of the green tapes were selected in order to obtain, after sintering, layers of about 200 μm (A) and 250 μm (AZ).

After drying, laminae of 50 mm $\times$ 34 mm were cut from the different ceramic sheets. Hybrid laminates were prepared by stacking and warm pressing the green sheets at 75 °C at a pressure of 30 MPa for 30 min (Fig. 2.2. Different samples were obtained by alternately piling one layer of alumina and one layer of alumina-zirconia (this structure is hereinafter designated as "A/AZ") or one layer of alumina and two layer of alumina-zirconia (hereinafter designated "A/2AZ"). The structures were designed in order to have always an alumina layer in both the outer surfaces. Debonding was carried out with a very slow heating rate up to 600 °C, followed by sintering at 1550 °C for 1 h. We thus obtained dense samples (97% of theoretical density) with a thickness of about 3.0 mm, containing layers with a thickness ratio of about 1/1.3 (A/AZ) and 1/2.6 (A/2AZ), the former shown in Fig. 2.3. In the hybrid samples, due to lower thermal expansion coefficient and shrinkage during sintering, the external alumina layers undergo residual compressive stresses. In order to facilitate the subsequent material preparation, additional sacrificial alumina layers, to be removed during the grounding and polishing process, were piled over the outer layers.

As reference material (*i.e.* nominally stress-free), pure monolithic alumina (MA) was prepared by cold isostatic pressing and sintering at 1550 °C for 1 h.

Once the laminated plates were produced, they were cut into prismatic bars of about 4mm$\times$3mm$\times$20mm with a diamond saw. The top layer of alumina (which was in compression) was polished with diamond suspension up to 3 μm with a low applied force in order to avoid excessive loss of material (30 μm at most), and to produce a similar sur-

face flaw size distribution for all the samples. Several samples were polished in the cross section area and thermally etched (1400 °C, 30 min) for observing the microstructure of the material nearby the interface.

Particular care was taken during the polishing of laminated materials, in order to avoid variation of the outer layers thickness from one zone to another of any sample and among the samples, because an excessive, or insufficient, amount of removed material would cause a redistribution of the residual stresses and, therefore, affect the experimental results.

Additional pure alumina samples were produced starting from the same powders, in which the sintering time was varied (3, 5 and 12 hours, respectively) in order to tailor the grain size. Such materials were used, as discussed in chapter 5, for isolating the influence of microstructural effects on the damage formation from the variations provoked by the laminated structure. The samples were labelled based on the sintering time, A03, A05 and A12, respectively.

2.2 Physical and mechanical characterization

Fig. 2.4 shows the SEM picture of the interface between two layers of alumina and alumina-zirconia, where it can be observed that the interface is well bonded. MA samples were prepared in the same way, and their microstructure was also observed by SEM. The grain size of the alumina layers of the laminates and the monolithic alumina MA, together with the A03, A05 and A12 samples, were measured using the average feret method, and are presented in table 2.1. The fact that the grain sizes are similar, together with the fact that both the laminates and the MA materials were produced in a similar way, suggests that the materials are similar at the microstructural level, and that any difference in the mechanical behaviour can be attributed to the differences in residual stresses produced by the laminated architecture.

2.2.1 Mechanical properties

The basic mechanical characterization was performed prevalently by means of indentation techniques. Such choice was dictated by the reduced size and the non-standard geometry of the samples. Traditional techniques were compared to instrumented indentation, which gave an additional insight of the local properties at nano-scale.

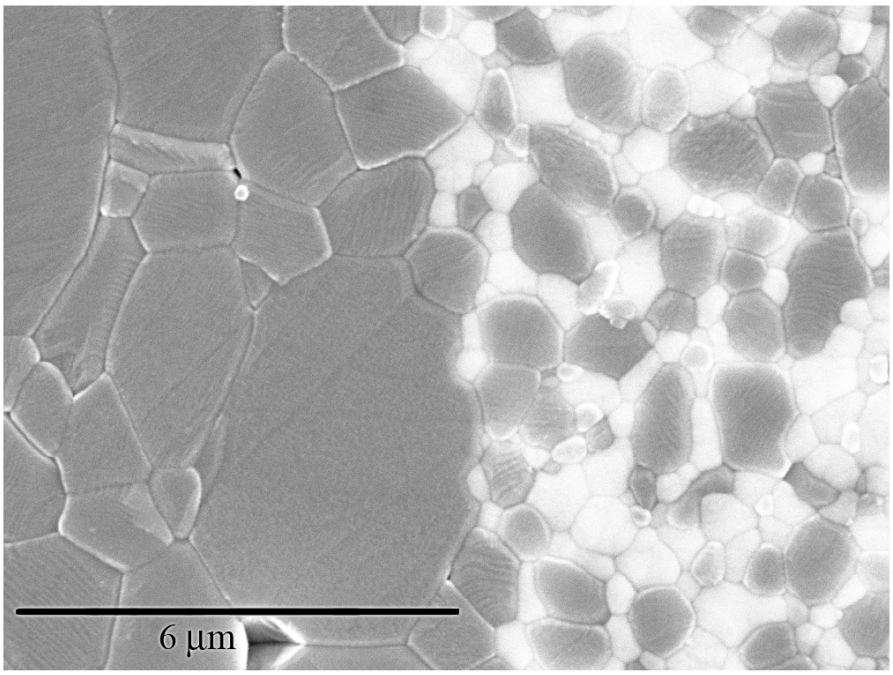

Figure 2.4: Microstructure of the interface between A (left) and AZ (right) layers. Zirconia grains appear as white for the higher atomic weight of zirconium with respect to aluminium

Table 2.1: Grain sizes, measured with the average feret method, of the materials studied. Alumina grains in A/AZ are finer due to the constraint provided by the surrounding zirconia grains

	MA	A/AZ	A03	A05	A12
d [μm]	1.9±0.7	1.1±0.8	2.6±1.6	2.9±1.7	3.8±2.3

Vickers hardness measurements were carried with different loads (200 g, 300 g, 500 g, 1 kg). For this load range, hardness proved independent of load, and therefore no size-effect was found, as expected. In the A/AZ laminate, measurements of hardness were performed at the top surface, perpendicular to the interface. To measure the hardness in the AZ layer, the top A layer was carefully removed by grinding and polishing on both sides of the sample in order to avoid unbalanced stresses and samples deformation. The mean hardness values of the alumina-zirconia was $H_V^{AZ} = 15.1 \pm 0.7$ GPa and the hardness of the alumina was found to be $H_V^A = 16.9 \pm 0.5$GPa. In the monolithic alumina the hardness was $H_V^A = 16.7 \pm 0.9$GPa. It can be seen that the MA and the alumina layer present comparable values of hardness.

Instrumented indentation tests were performed in a fully calibrated MTS Nanoin-

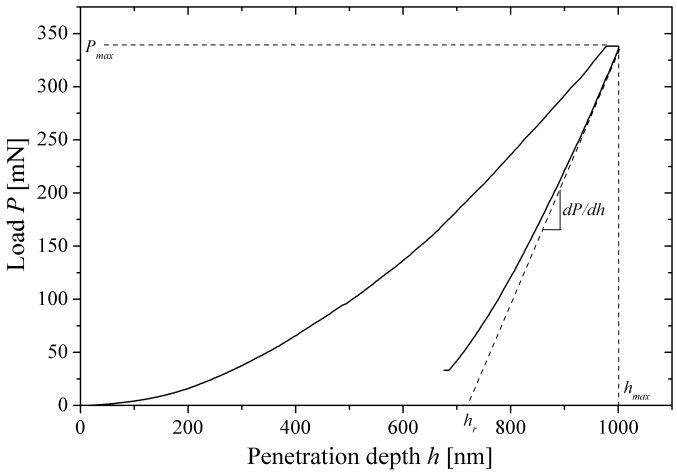

Figure 2.5: Typical *P*-*h* curve obtained by instrumented nanoindentation

denter XP (Nanoinstruments Innovation Center, MTS Systems, Oak Ridge, TN, USA) equipped with CSM (Continuous Stiffness Measurement). For the extraction of the properties mentioned above, a Berkovich indenter was used. The values obtained, as a function of the penetration depth, are presented in Fig. 2.6. The discrepancies with macro-indentations depend on the different scale at which the measurements are conducted and on the different approach for the calculation: with instrumented indentation the contact area is deduced from the penetration depth under the maximum load, while with the traditional method the contact area is measured optically after unloading, so that the elastic recovery is not taken into account.

The Young's modulus, following the well-known Oliver and Pharr method [71], can be extracted from the stiffness S measured on the unloading portion of the curve:

$$S = \beta(\nu)\frac{2}{\sqrt{\pi}}E\sqrt{A} \tag{2.1}$$

where A is the contact area and $\beta(\nu)$ is a function given by Hay *et al.* [72]. The values obtained, shown in Fig. 2.6 as a function of the penetration depth, were in agreement with the literature, although slightly higher, due, again, to the limitations of the method.

Fracture toughness of both MA and A/AZ (measured in the top alumina layer, so the interface was located below the indentation, and perpendicular to the indentation load) was evaluated by measuring the crack lengths produced by a Vickers indentation of 10 kg. The fracture toughness of the AZ layers was not measured because their thickness was too small for producing suitable crack lengths without reaching the interface.

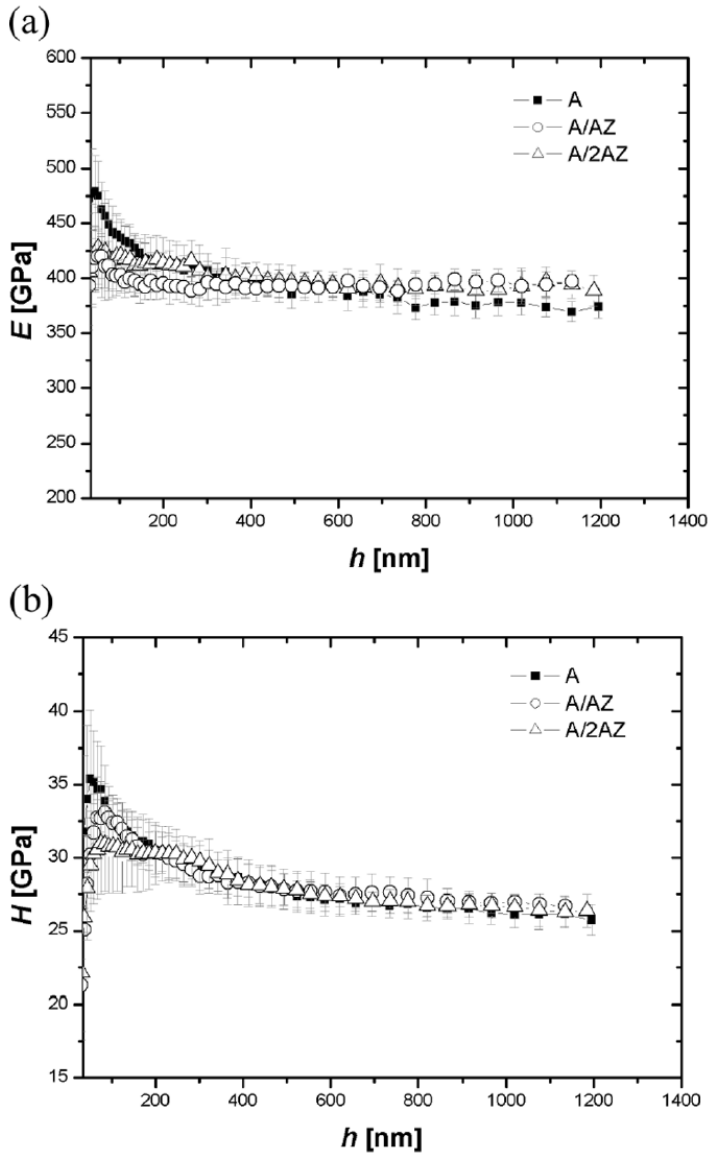

Figure 2.6: a) Young modulus and b) hardness as a function of the penetration depth under instrumented indentation

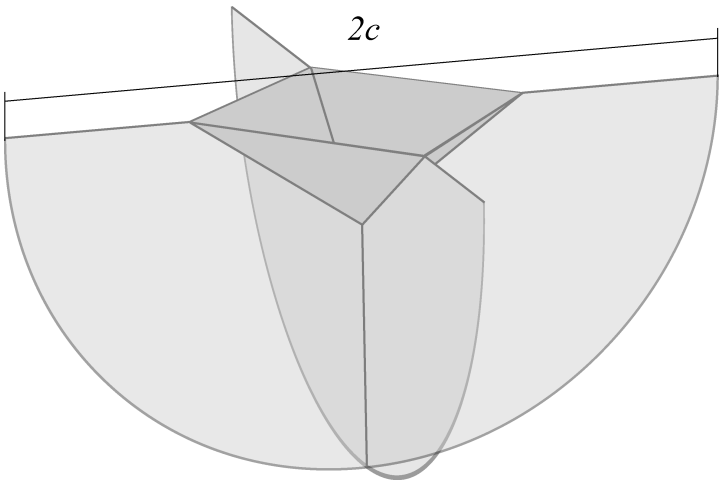

Figure 2.7: Scheme of fracture toughness measurement by Vickers indentation

Also, the fracture toughness of the A/2AZ composite was not measured because Vickers indentations produced excessive chipping in the material due to the higher compressive residual stress.

Fracture toughness evaluation by the method proposed by Antsis [73] is based on the assumptions of penny-shaped cracks generated upon unloading and a constant value of toughness. Due to the presence of *a priori* unknown residual stresses and microstructural features affecting the toughness (the mentioned R-curve), both assumptions are acceptable only on a first approximation. Acknowledging that the values obtained in this way have to be considered as approximate due to the limitations of the method, the fracture toughness (K_{Ic}) was then evaluated through:

$$K_{Ic} = \chi \frac{P}{c^{3/2}} \tag{2.2}$$

where P is the load, c the crack length and $\chi = 0.016(E/H)^{1/2} = 0.08$ a geometry coefficient, calculated for the monolithic material, and assumed as constant in the A/AZ for sake of simplicity. Substituting the values of the measured crack lengths, the fracture toughness obtained for both materials were $K_{Ic}^{A} = 3.5 \pm 0.8$ MPa·m$^{1/2}$ and $K_{Ic}^{A/AZ} = 6.0 \pm 0.8$ MPa·m$^{1/2}$. For the sake of simplicity, any effect of R-curve is neglected, therefore K_{Ic}^{A} is taken as the intrinsic value of the toughness. The value of the A/AZ has to be taken as an apparent value, as there the toughness is influenced also by the residual stresses.

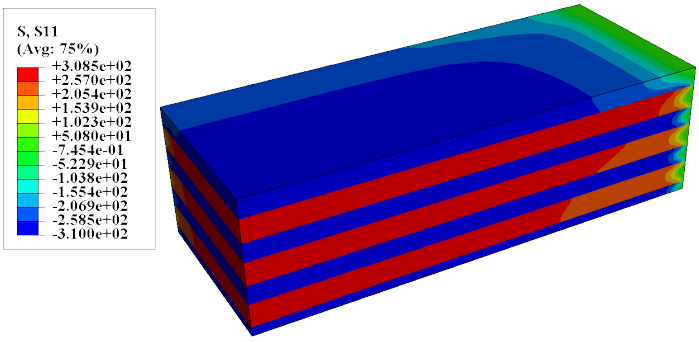

Figure 2.8: Residual stress distribution, as calculated by Finite Element analysis

2.2.2 Residual stresses

A correct evaluation of the residual stress that is generated by differential shrinkage during cooling after sintering of the laminates is required for a proper analysis of the properties extracted and, in general, of the variations in the material response. The issue was approached with different techniques, which are hereinafter presented and summarized in table 2.2.

The analytical approximation (see eq. (1.2)) is based on the assumption of purely biaxial stresses on an infinite body, neglecting therefore the influence of free surfaces at the edges. A similar *a priori* analysis was conducted by means of a Finite Element model, whose details will be further discussed in the next chapter, based on the simulation of the shrinkage and on the assumption of constant coefficients of thermal expansion α.

2.2.2.1 Indentation techniques

An evaluation of the amount of residual stress can be extracted from comparison of the apparent toughness in laminates with the intrinsic toughness, as measured in the monolithic material. Considering both the indentation and the residual stress contributions to the apparent toughness, the following relation can be deduced:

$$K_{Ic}^{A/AZ} = \chi \left(\frac{P}{c_{MA}^{3/2}} \right) + Y\sigma_r \sqrt{c_{A/AZ}} \tag{2.3}$$

with $Y = 1.29$ a geometry coefficient. From there:

$$Y\sigma_r = \frac{K_{Ic}^{A} - K_{Ic}^{A/AZ}}{\sqrt{c_{A/AZ}}} \tag{2.4}$$

2.2.2.2 Instrumented indentation

Instrumented indentation is, *a priori*, a suitable technique for local evaluation of residual stresses and, thus, several methods have been developed, especially for metals with relatively low yield stress and that do not work-harden appreciably when indented with sharp indenters. Most of these methods are based on the change in penetration depth (which does not affect the hardness value) with and without residual stress [74, 75] or the change in elastic penetration depth [76, 77]. Swadener *et al.* [51] used spherical indenters instead of sharp indenters and showed that blunt indentation is more sensitive to residual stress during the elastic to plastic transition than sharp indentation, and developed a methodology for extrapolating the onset of plasticity and, from there, the amount of σ_r.

Nevertheless, the mentioned techniques were applied to the laminates under study. Under any indentation condition and with any indenter, no difference was appreciable in the $P - h$ curves, and Atomic Force Microscopy measurements of the residual imprints showed no change in the area, as it can be appreciated in Fig. 2.9. This is attributed to the high hardness and, consequently, yield stress in alumina, especially compared with the amount of residual stress, much below the range of application of all the techniques presented. It was concluded that, for the studied case, the variations in the nanoindentation response produced by residual stress is not appreciable.

2.2.2.3 Raman diffraction

The issue of residual stresses measurement and distribution was studied deeply by de Portu *et al.* [78], who employed Raman and fluorescence piezo-spectroscopy to evaluate the amount and distribution of residual stress. The fluorescence lines of Cr^{3+} impurities present in alumina are shifted in presence of stress, as well as one of the Raman bands of 3Y-TZP, of an amount which can be expressed as

$$\Delta\nu = \frac{1}{3}\Pi_{ii}\sigma_{jj} \tag{2.5}$$

where σ_{jj} is the first invariant of the stress tensor and Π_{ii} the trace of the piezo-spectroscopic matrix.

From Eq. (2.5), after calibration and with a narrow enough laser beam (1 to 5 μm wide spot), it is possible to obtain linear two-dimensional stress maps with a high resolution (depending on the laser spot size, typically some μm). Moreover, the beam

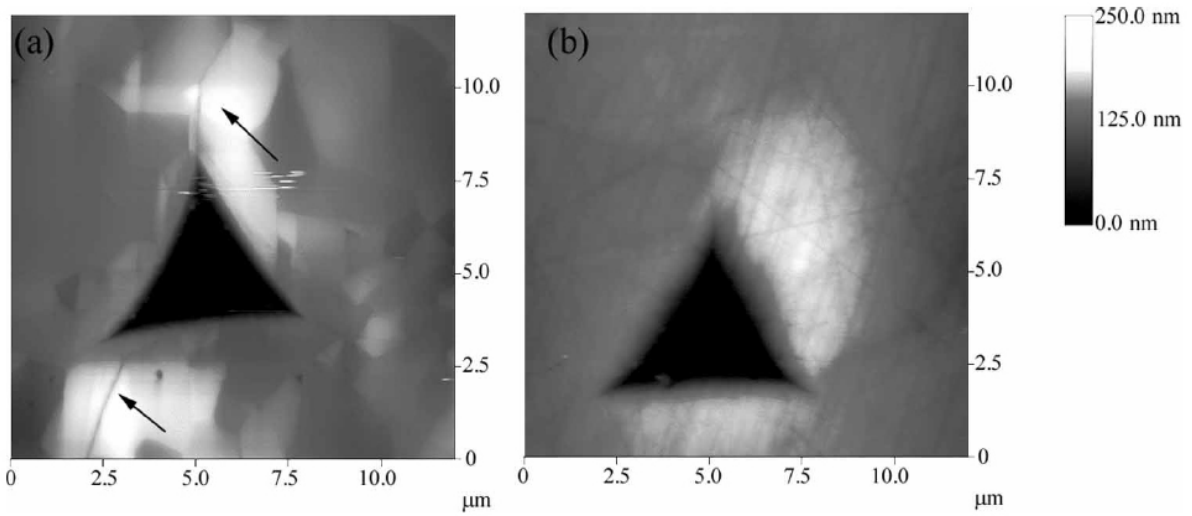

Figure 2.9: AFM of the indentations imprints produced with a Berkovich indenter in alumina (a) and A/AZ laminated composite (b), with a total penetration depth of 1 μm. Arrows in the alumina image show the existence of radial cracks.

penetration varies as a function of the laser spot size, yielding the possibility to overcome, to some extent, the limitation, typical of spectroscopy techniques, of small volume tested. In the mentioned work, the authors evaluated the amount of residual stress far from the edges by means of a semi-analytical calculation.

The values of residual stress on the top alumina layer evaluated with each technique are reported on table 2.2. Comparison between the values obtained with each technique needs caution, because the definition of residual stress can vary: the analytical approximation (Eq. (1.2)) assumes and evaluates purely biaxial stresses, *i.e.* the first and second principal component of the tensor; similarly, fracture mechanics expression is based on uniform uniaxial stress acting on the crack; on the other hand the piezo-spectroscopy techniques measures the first invariant of the stress tensor, which is a measure of the average pressure; Finite Element Analysis provides a complete estimation of the stress tensor, allowing thus to estimate the residual stress by both approaches.

Under these considerations, the values measured show to be good agreement one with another: the near-the-edge value by piezo-spectroscopy, which is probably the most reliable among the techniques presented, and the analytical approximation, credible in the center of the sample, are both corroborated by the simulation results, which confirms also values obtained from indentation.

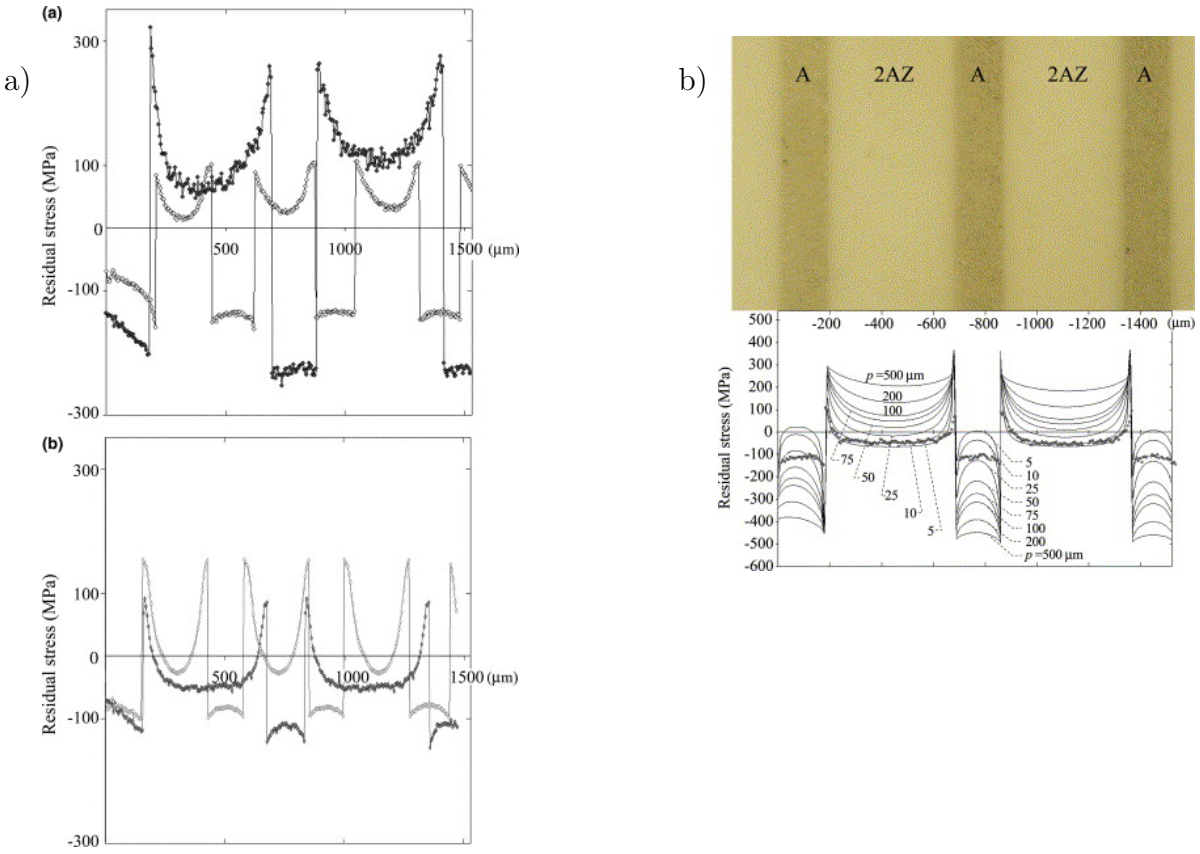

Figure 2.10: a) Residual stresses linear map measured by piezo-spectroscopy on the cross-section of A/AZ and A/2AZ multilayers, b) theoretical calculation of near-edge stress [78]

Table 2.2: Summary of residual stress in ceramic laminates as measured with different techniques. The value refers to the top alumina layer

	A/AZ		A/2AZ	
technique	edge	center	edge	center
analytical	-283	-283	-374	-374
FEM	-65	-183/-271[a]	-80	-234/-355[a]
indentation	–	-180	–	[b]
spectroscopy	-70	–	-140	–

[a]Values corresponding to both $1/3\sigma_{jj}$ and σ_{11} are reported
[b]Residual stress of A/2AZ was not measurable for strong chipping under Vickers indentation

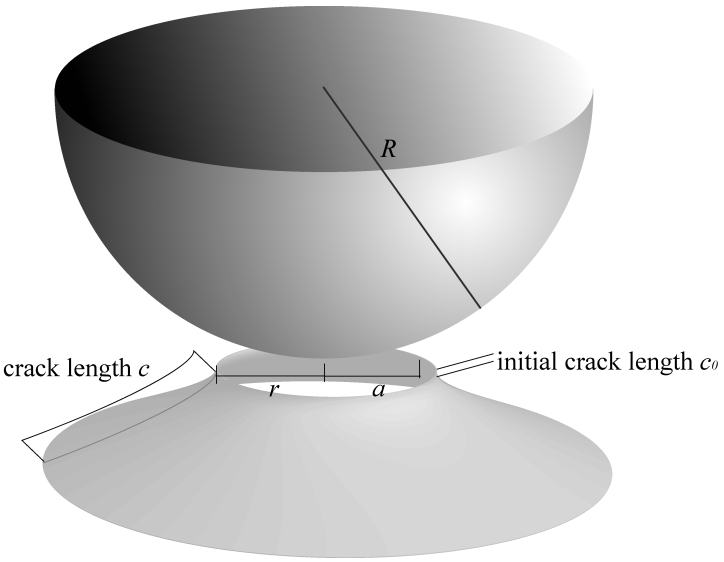

Figure 2.11: Scheme of Spherical indentation

2.3 Spherical indentation techniques

As discussed already, spherical indentation was chosen as the main contact characterization tool, for the advantages such technique offers, allowing flexibility in the tests design and being representative of the in-service loading conditions.

All the contact tests were performed with WC-Co (E=600 GPa, ν=0.3) spheres as indenters. The indenter radius was varied according to the type of test; the most common choice was R=1.25 mm, which guaranteed most of the stress field to be contained within the top layer and far enough from the stress-free edges. A disadvantage produced by the choice of the material for the indenter is the elastic mismatch between indenter and substrate, which influences slightly the stress field, with the effect of affecting the critical load for appearance of brittle damage. In some cases of high-frequency fatigue, moreover, the friction between the two bodies could produce fretting damage. Nevertheless, hard metal presents other advantages, primarily high toughness and resistance, which reduces the risk of failure during tests. Moreover, the high Young's modulus allows to simulate the indenter in the FE models with a hard non-deformable body, with benefit in terms of calculus velocity and simplicity.

Indentations were performed on universal testing machines, either an electromechanical Instron 8562 or a servohydraulic Instron 8500, both equipped with a 5KN load cell, for static and cyclic loading, respectively. Sample holders (Fig. 2.12) were designed at

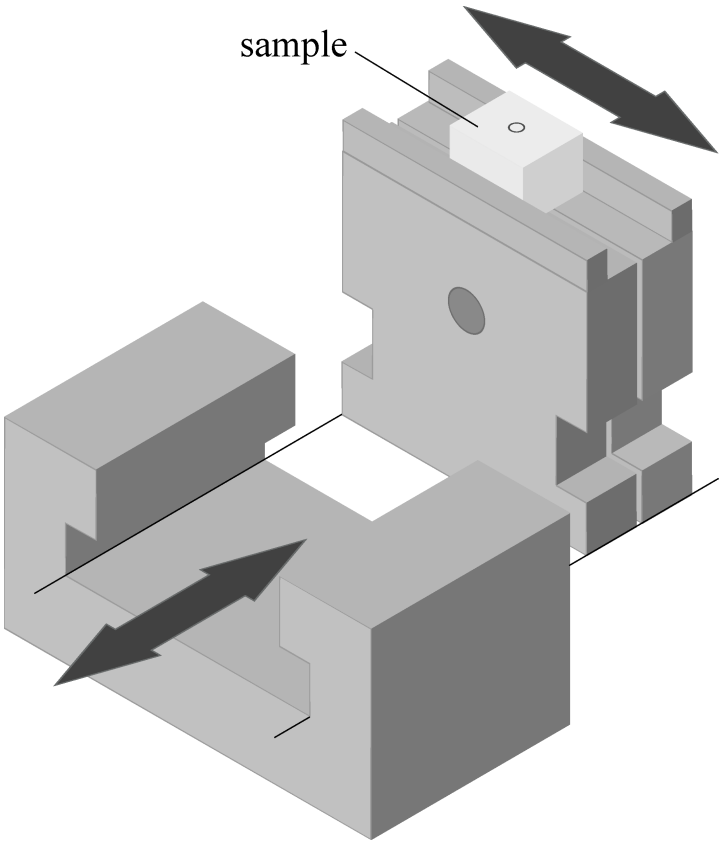

Figure 2.12: Scheme of the sample holders employed in the spherical indentation tests, which allow accurate placement in both axis

purpose to allow accurate sample placement and avoid undesired small displacements. Protocols were developed for the calibration of the gain parameters of the machines, before every experimental session, in order to avoid accidental load fluctuations and peaks and assure reproducibility.

The indentation procedure for single-cycle followed the scheme in Fig. 2.11: load was increased at the constant rate of 50 N/s, then maintained for 15 s and retired. The same procedure was applied to static-fatigue tests, with longer maintaining times. In the case of cyclic tests, load was increased up to the mean value, and sinusoidal oscillations were applied of increasing amplitude and frequency, until the test conditions were attained.

The local nature of indentation tests allowed performing several indentations on every sample, all in the top layer, taking care of indenting in the constant-stress zone, which is to say, far enough from the edge, and of separating the indentations each from the other of not less than 2 mm.

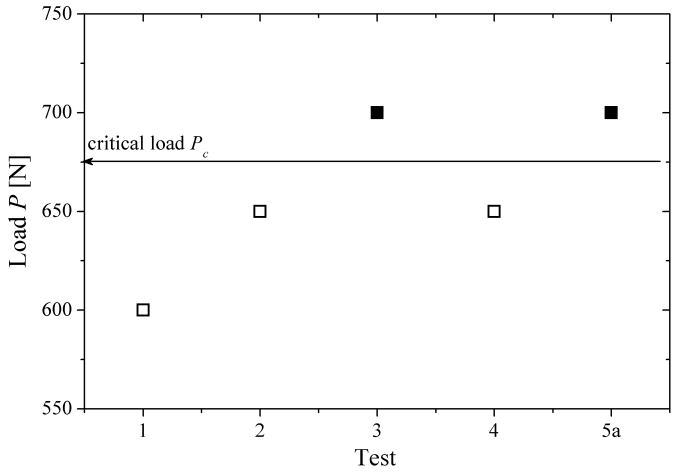

Figure 2.13: Typical staircase plot for the determination of critical load P_c for ring cracking. Empty symbols mean no visible damage, filled symbols mean detectable ring crack

For the first part of the study (see section 4.1) the appearance of ring crack was considered the damage criterion. The range of load for damage formation was sought iteratively with a staircase plot (Fig. 2.13): after testing, the surface was examined in search of a well-developed ring crack; as a standard criterion, only cracks with an opening angle greater than 180 °, in other words half the circumference long, were considered. In the subsequent test the load was either reduced or increased whether damage was visible or not, respectively, and the procedure was repeated until three consecutive load reversions were observed. A critical load range for the appearance of ring crack was therefore defined.

In cyclic and static tests the procedure was repeated for different numbers of cycles or maintaining times (varying between 1 to $3{\cdot}10^5$ cycles and from 10 to 10^6 seconds, respectively), so that it was possible to extract fatigue curves by plotting the critical load range as a function of the test duration.

The remaining parameters of the cyclic loading during fatigue tests were defined as follows: the minimum load was kept constant P_{min}=50 N; the maximum load P_{max} was one of the input variables of the test, ranging from 200 to 700 N (for load ratios $R = P_{min}/P_{max} = 0.07 - 0.25$), as well as, consequently, the average load $P_{av} \equiv (P_{max} + P_{min})/2$ and the amplitude $\Delta P \equiv (P_{max} - P_{min})/2$.

Additional fatigue tests were conducted on one of the materials (A/AZ) under a constant amplitude $\Delta P = 200$ N and varying the maximum load, and under a constant

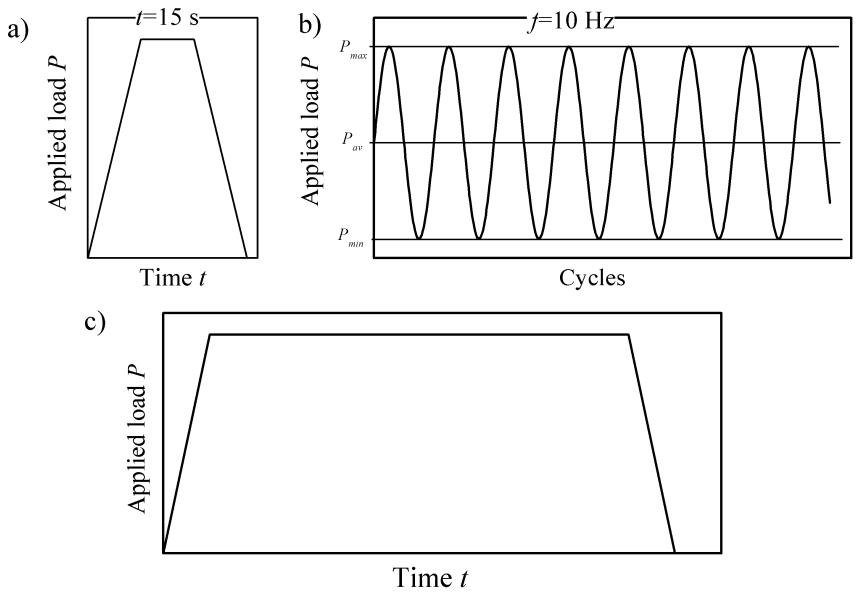

Figure 2.14: Scheme of the types of loading tested: a) monotonic, b) cyclic and c) static

maximum load $P_{max} = 500$ N and varying the amplitude.

2.4 Damage observation techniques

An important part of this work is dedicated to the analysis of subsurface damage; observation of such damage is in some cases challenging, and needed special techniques to be developed.

The cut-and-bond technique, applied to the Hertzian system by Guiberteau *et al.* [49], involved sectioning of the sample on the direction perpendicular to the layers, fine polishing of both parts on the lateral surface and, after bonding the halves, on the surface to be indented. After indenting carefully in the interface, it is possible to separate again the parts of the sample and observe the damaged surfaces. The limitations of this technique reside in the application to laminated materials: cutting the samples produces release of the stresses near the edges, so that the response is not the same of the uncut material. Moreover, the reduced size of the samples and the layers (200-250 μm thick) makes it difficult to couple correctly the layers, and polishing subsequent to the bonding is also problematic.

The transverse polishing technique overcomes these limitations: after indentation,

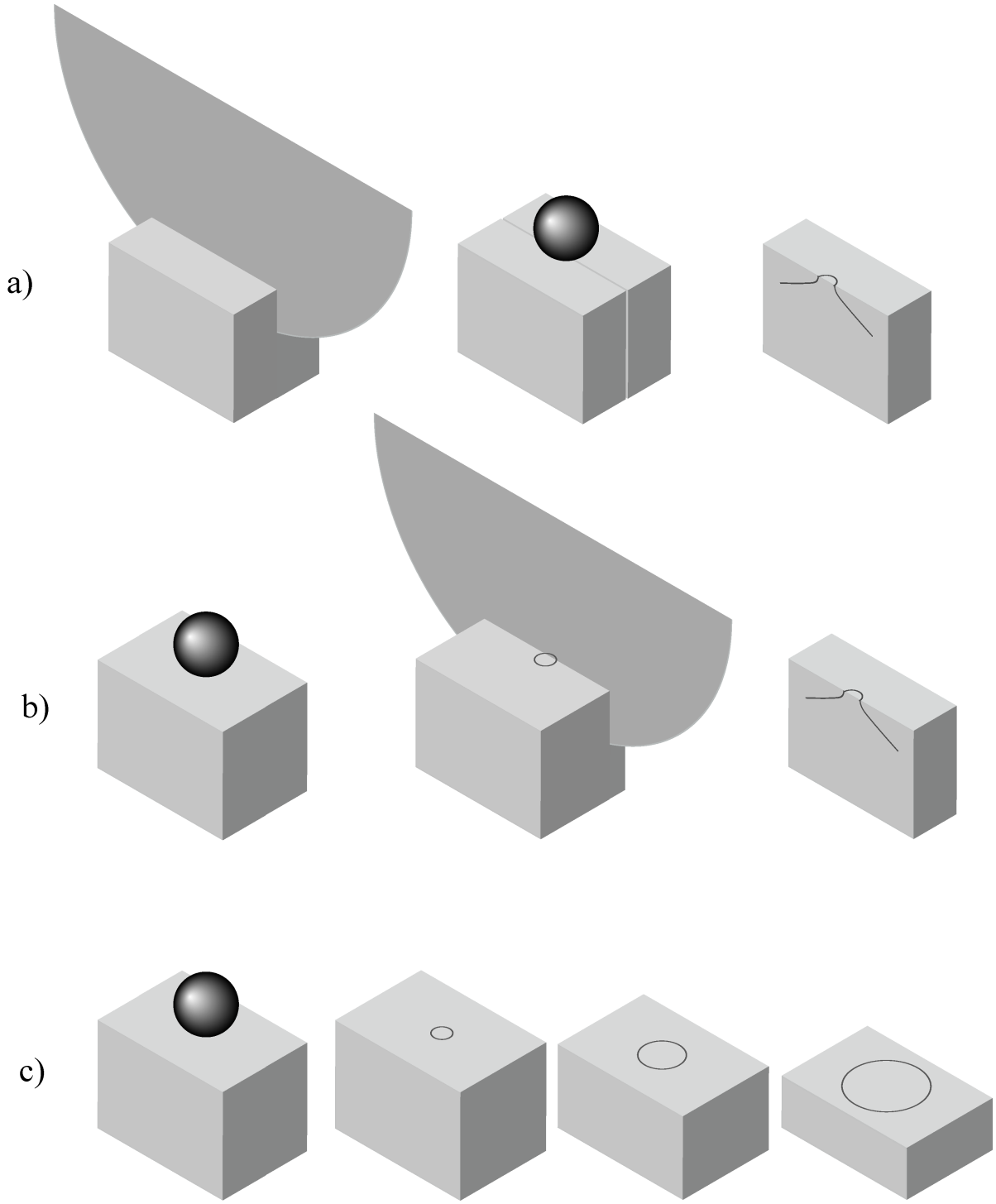

Figure 2.15: Scheme of the sectioning techniques employed for damage evaluation: a) cut-and-bond, b) transverse sectioning, c) parallel grinding

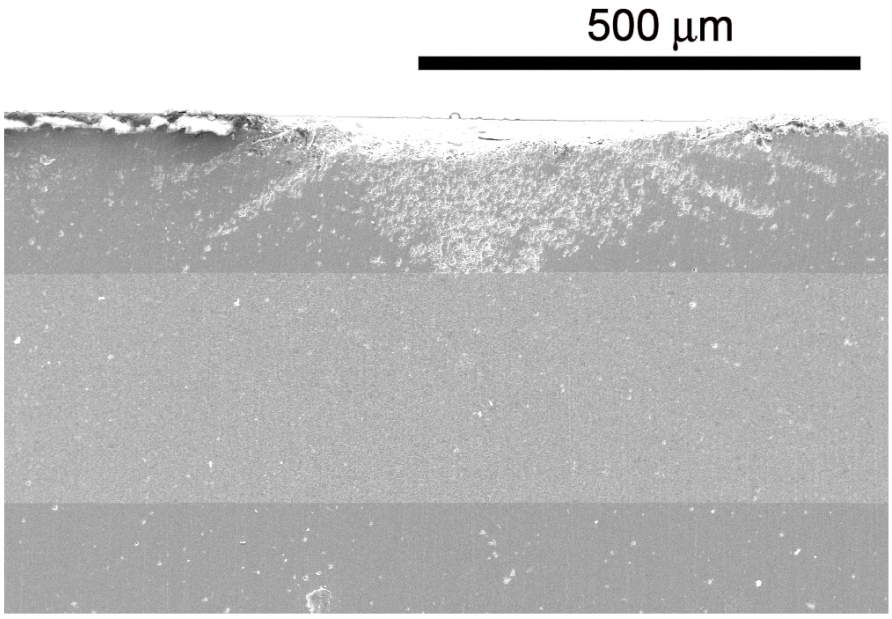

Figure 2.16: Example of grinding-enhanced quasi-plastic microcraking after application of the transverse sectioning technique

samples were cut nearby the damaged zone, then carefully ground and polished perpendicular to the indented surface until the center of the ring/cone. The drawbacks of such technique are the longer time necessary and the grain pull-out during polishing, which is especially strong at the crack lips, making it difficult to measure both the crack length and angle. On the other hand, such pull-out is enhanced by microcracking, evidencing thus the zones damaged by quasi-plastic deformation.

This latest technique was extensively employed for the part of the thesis presented in chapter 5, dealing with the propagation of cone crack in ceramic laminates.

As a faster alternative, the parallel-grinding technique was employed when accuracy was not needed in the measure of the crack angle and a qualitative assessment of the presence and nature of damage was required, such as in section 4.2. For this technique, after indentation the sample thickness was measured, then a thin layer of material was removed by grinding, the surface was coarse polished for the ring crack observation and measurement; this procedure was followed several times, until the crack was not visible anymore. From the values of ring radius at different depths, calculated from the difference to the original thickness, the cone crack was reconstructed. This technique allows also observation of quasi-plastic damage, just as the transverse polishing methodology.

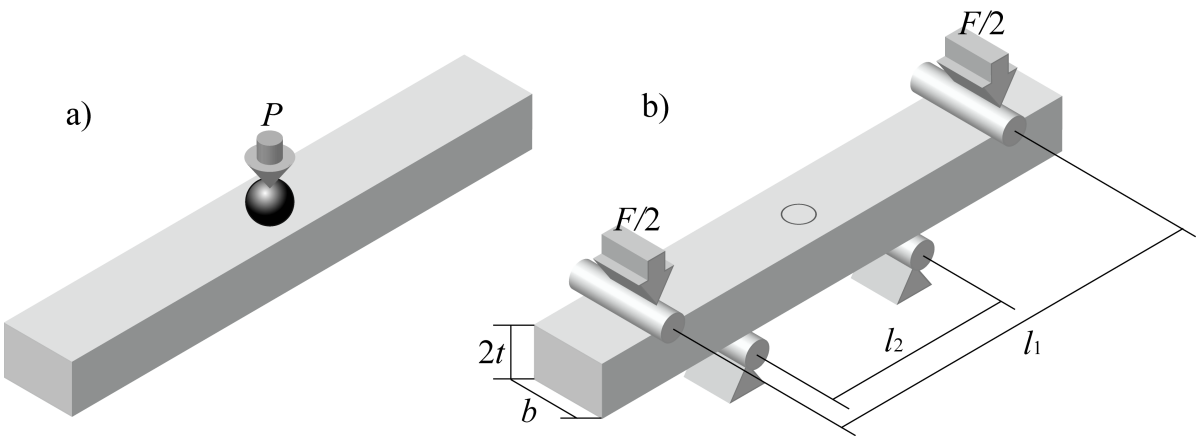

Figure 2.17: Phases of residual strength measurements: a) indentation, b) bending

2.5 Residual strength testing

The effect of contact damage on the strength degradation of ceramic laminates was studied by means of indentation-bending tests. Indentations in the center of the bars were performed in an Instron servohydraulic machine. Due to the microstructure dependence and to the stability of the crack, it was decided to apply cyclic loading in order to guarantee completely developed and uniform cracks. The indenter used was a WC-Ni 2.5 mm radius sphere, two applied maximum loads straddling the critical load for appearance of cone crack (500 N and 900 N, respectively) were chosen in order to achieve different crack conditions and consequently amounts of strength degradation. The minimum load was kept constant to 50 N, the duration of the cyclic test was kept constant to 10^5 cycles in order to reach the higher damage possible for the given load. Four to six bars were tested for each loading condition.

The indented bars were successively subjected to four points bending tests, with spans l_1= 20 and l_2= 10 mm, respectively and a loading rate of 200 N/s, high enough not to allow environment-assisted crack propagation. Unindented bars were tested as well to obtain the strength of undamaged material. After testing, fracture surface of the bars broken from the cone crack was observed with optical and scanning electron microscopy.

From the load at the moment of fracture, the fracture strength was calculated, following the equation

$$\sigma^* = \frac{3}{2}\frac{F(l_1 - l_2)}{(2t)^2 b} \tag{2.6}$$

with the symbols as defined in Fig. 2.17.

The fracture stress σ^* thus defined is, in the case of the laminates, an *apparent* strength, and does not correspond to any actual value of local stress inside the material. The importance of the values deduced this way resides in the comparison with materials with no residual stresses. Differences arising in unindented materials depend mainly on the presence of residual stresses in the top layer, where the bending stress is higher.

Moreover, as it will be presented in chapter 5, damage generated whether in ceramic laminates or in monolithic materials under the same indentation condition, is different in type and amount, consequently the outcome of the bending test is influenced by the different starting flaw.

The issue was analyzed by means of Finite Element simulations of actual aimed bending tests on cone-cracked materials, as it will be discussed in the next chapter.

2.6 Contact strength testing

The stress field generated by symmetrical compression by cylinders was computed numerically by Fett *et al.* [69], who established the simple relation

$$\sigma_x^{max} = 0.490\sigma_{eq} \tag{2.7}$$

for point-load, with $\sigma_{eq} = F/tb$, normalized load, t half the sample thickness, b the sample width and the other symbols as in Fig. 1.11. Under pressure load in a contact zone of width $2s$, expressed with the Hertzian pressure distribution $p(x) = p_0\sqrt{1-(2x/s)^2}$, the maximum stress is slightly reduced, no more than 1%, as s increases. Tensile stress is generated also along the symmetry axis; in case of point-load Eq.(2.7) is fulfilled, with the maximum located on the loading point; however, if the contact zone is non-singular, the ratio $\sigma_x^{max}/\sigma_{eq}$ drops down rapidly as s increases, so that fracture is normally expected on the surface rather than within the material.

Reported results of contact strength tests showed strength values in agreement with those from bending tests, while Weibull exponents were roughly halved [69]. This latter is due to the high stress gradient generated [79] and should not be seen as a limitation of the method, but rather as an indication of how dangerous multiaxial contact loading can be and that a specific testing methodology is recommended, whenever such a type of loading is expected in-service, as in the case of ceramic multilayers.

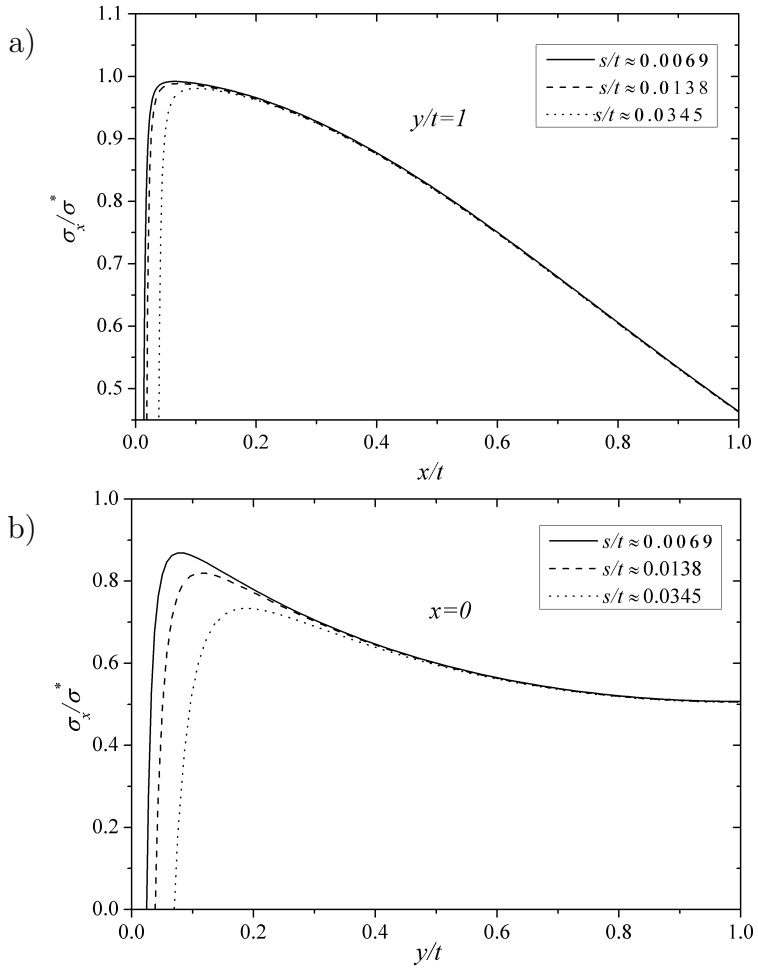

Figure 2.18: Normalized stress σ_x under contact strength test at the surface (a) and along the axis (b) for different values of the contact zone width $2s$

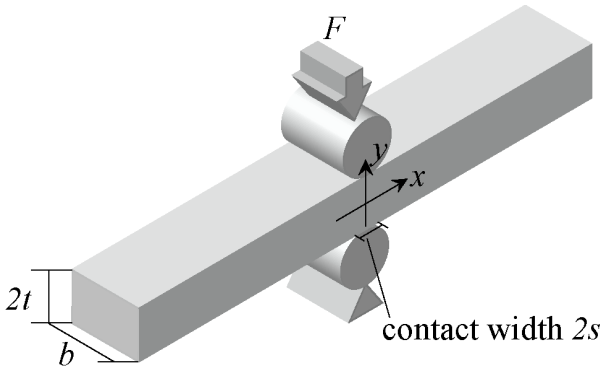

Figure 2.19: Scheme of the contact strength testing

The tests were performed on an UTS testing machine. Samples were placed with the external, compressive layer in contact with the rollers. Load was applied by two opposite $4mm$ radius hardened steel rollers at the constant rate of 100 N/s. The rate chosen is slightly lower than suggested for strength tests, in order to better identify, with visual aid, the fracture load, as mentioned below; however, no subcritical crack growth is expected under this kind of test [79]. Tests were interrupted when fracture occurred, with either or both extremities of the sample falling apart, and often the remaining portion shattering for compression. Fracture loads were recorded and the critical load for the first fracture event, sometimes coinciding with the ultimate strength, sometimes with an earlier pop-in.

CHAPTER 3

Finite Element Analysis

3.1 Introduction to FEM

Finite Element Analysis (FEA) is a computer simulation technique used in engineering and physical analysis. In its application, the system or object of study is represented as an unstructured grid of discrete regions, composed by *nodes* and a web (*mesh*) interconnecting them. Equations of equilibrium, in conjunction with proper physical considerations, such as compatibility and constitutive relations, are applied to each element, and a system of equations is constructed, and solved iteratively by means of linear algebra techniques. Probably the most common application of FEA is for determining equilibrium stress and displacement in mechanical systems, however, it allows solving many other types of problems, such as heat transfer, electromagnetism, fluid dynamics, and virtually any phenomenon expressible by partial derivative equations.

The mathematical part, the Finite Element Method in itself, is based on finding an approximate solution of partial differential equations. The basic idea is to replace the infinite dimensional linear problem with a finite dimensional version, expressed as a linear combination of an appropriately chosen basis of first- or superior-order functions, typically polynomials functions. The equations thus obtained are written in a matrix form (including the so-called *stiffness matrix*), which can be solved by means of several techniques, depending on the specific problem.

The potentiality and versatility of FEA makes it a powerful tool, widely and increasingly employed in finding solutions to engineering and physical problems. While in industry-related applications FEA is powerful mainly as a design tool, in that it allows

to characterize *a priori* the in-service behaviour of the studied component, with benefits in terms of time and cost, the asset of FEA as a tool for fundamental research lies in the assistance in the formulation and verification of models, which are the basis for a deep understanding of the phenomena acting on the material. In material science, specifically, this translates into a characteristic *modus operandi*, consisting of tightly connected experimental and computational tasks, the latter intended, as anticipated, as an assistance and verification tool of the data collected with the former.

This procedure tries to provide an answer to the controversial issue of credibility of the results obtained by FEA. To which point the mathematical, continuum representation captures with realism and accuracy the complex deformation mechanisms (to stick up in the field of mechanical analysis) acting at multi-scale level inside the material? *Ab initio* analysis are far too resources consuming to be applicable to the majority of the practical cases and materials. Constitutive equations are strongly consolidated and effective in the simulation of many metallic materials, but less developed in ceramic materials, since deformation is usually associated to cracking, either macroscopical or at a grain-sized scale. On the other hand, a common risk is to disconnect completely from actual tests, so that the output of a simulation is by itself not believable, lacking of the fundamental corroborations.

The approach taken in many parts of this work was to couple in a bilateral way experiments and simulations: the physical hypothesis (e.g. elastic and thermal constants, sample geometries, ...) were measured, as much as possible, directly from the studied materials; the tests were designed in light of the posterior simulation; the models formulated were checked with cases from literature or simple analytical examples before being applied to the case of study. The results of simulations helped to rationalize the behaviour observed and to deduct general considerations, in the effort to provide quantitative or, where not possible due to the complexity of the phenomena studied, semi-quantitative relations useful for the design of improved materials.

In the same manner, the continuous feedback from and to actual tests resulted, especially in the study of cone crack propagation (section 3.5), in a progressive evolution of the models, wherever some hypothesis showed to be ill-founded or some unexpected feature worth analyzing emerged from experimental results. For sake of clarity, only the final version of the models is hereafter presented, therefore the reasons for some features may appear arbitrary or not supported by data; they are expanded and explained in the following chapters, where the issues here established only from the simulation point of

view are treated in their completeness.

3.1.1 `Abaqus`

All the Finite Element models were carried out with the commercial software `Abaqus`, versions 6.5 and 6.6, developed by *Abaqus Inc.*, a brand of *Dassault Systèmes S.A.* [80].

`Abaqus` is a multi-purpose package, in that it presents a wide range of element types and loading conditions, embracing many fields of physics and opening also to problems, such as fracture mechanics, which are not approachable with the traditional FEM methods. Another feature of Abaqus which makes it attractive for academic institutions is the high flexibility granted by the open-source scripting language Python, which allows scripting, customization and automatization of most of the steps of all the phases of FEA.

Like many commercial packages, Abaqus covers the three main phases of FEA:

Pre-processing is included in the `Abaqus/CAE` module, and comprehends the model creation, the mesh generation, the definition of boundary conditions, loading and material, and all the calculus variables (elements choice, order of integration, user-defined functions,...),

Calculation is performed by the calculation engines, `Abaqus/Standard` for traditional implicit finite element analysis and `Abaqus/Explicit` for transient dynamics and quasi-static analysis,

Post-processing is included in `Abaqus/CAE` and in the stand-alone `Abaqus/Viewer` product, allows to visualize the desired output with the aid of graphical and numerical tools.

3.2 Application: residual stresses evaluation

As anticipated in the previous chapter, and consistent with the philosophy expressed above, an evaluation of the residual stresses present in the studied laminated ceramics was conducted by FEA, in order to obtain a complete characterization of the distribution, which could corroborate and assist in the interpretation of the values measured locally in the center of the layers or at small depth, by indentation techniques and by piezo-spectroscopy, respectively. It is worth highlighting that these latter techniques allow to

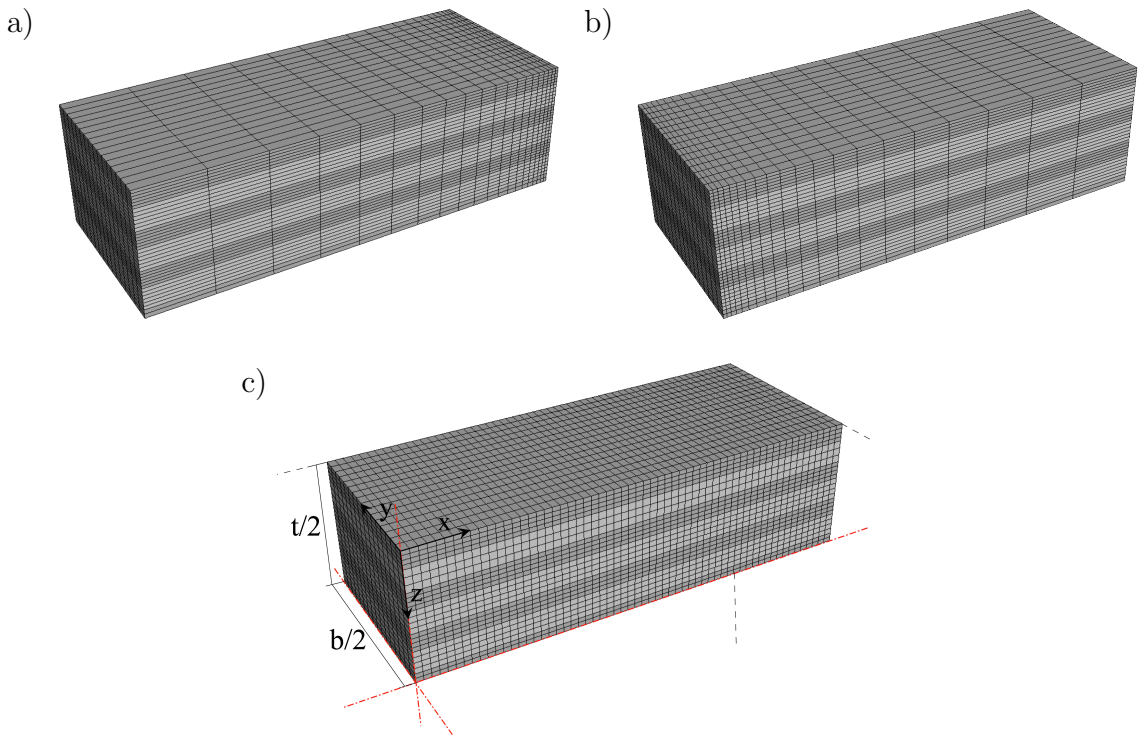

Figure 3.1: Meshes employed in the residual stress evaluation of the stress map a) near the edge, b) in the center and c) on the surface, respectively, representing one eight of actual samples. In c) the symbology and the symmetry axis are also reported

evaluate the residual stresses in the center of the sample and near the edges, respectively, and that therefore the evaluation obtained by means of FEA can act as a link between them.

The residual stresses were calculated by simulating the shrinking taking place during cooling after sintering. Three-dimensional models were created, reproducing the geometries of the actual A/AZ and A/2AZ samples. The appropriate symmetries were imposed to three of the faces in order to simulate only one eight of the sample, reducing thus the time and resources consumption. The materials were represented as purely elastic, with elastic constants taken from previous works [20]. Cooling was simulated as a steady state transition from an initial temperature T_i=1200°, above which zirconia deforms with an elasto-plastic behaviour, and therefore no stress is generated [81], to the room temperature T_f=30°. The values of the thermal expansion α were taken from direct measurements on the starting materials [20], and assumed as constant in the entire temperature range.

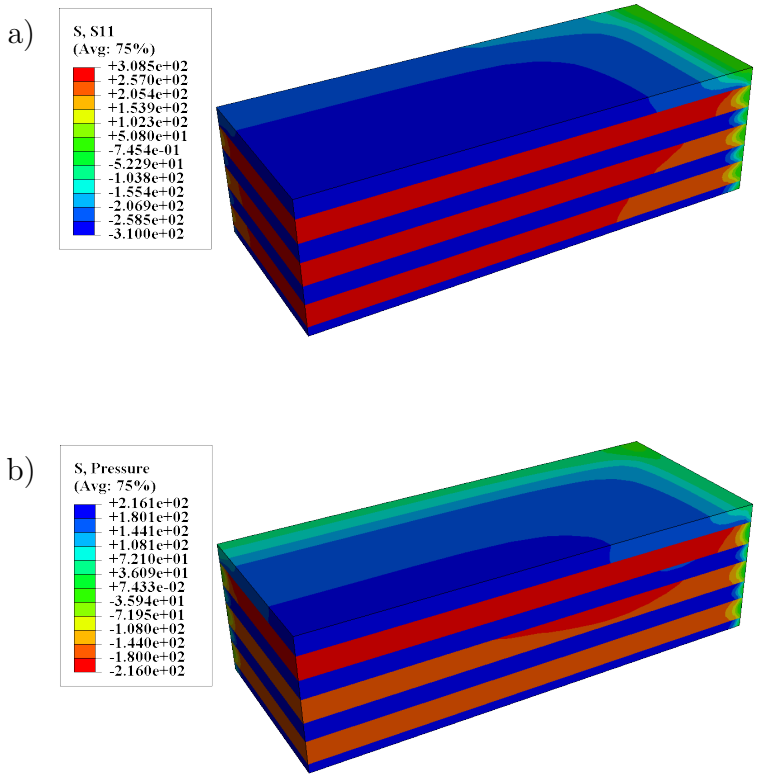

Figure 3.2: 3D maps of a) the σ_{xx} and b) the average pressure present on the sample

In order to reduce the calculation times[1], several meshes were created, shown in Fig. 3.1, each one finer in a different zone of the model, in order to produce accurate local stress maps. All the meshes were composed by approx. 20000 linear elements.

Linear maps corresponding to the center of the sample and to the near-edge zone are shown in Fig. 3.3. In the former the σ_{xx} component is represented, for comparison with the analytical expression. In the latter the average pressure $1/3\Sigma\sigma_{11}$, allows comparison with the piezo-spectroscopy measures. Employing, in this case, the σ_{xx} would provide incorrect results, because near the edge the stress redistribution generates a non-negligible normal component.

The values are in good agreement, which suggests that, despite the simplicity of the model created, Finite Element analysis is effective in evaluating quantitatively the stress amount and distribution in ceramic laminates.

The stress relaxation is shown in Fig. 3.4, in terms of σ_{ii} as a function of the linear

[1]because augmenting the elements number increases the calculation time exponentially

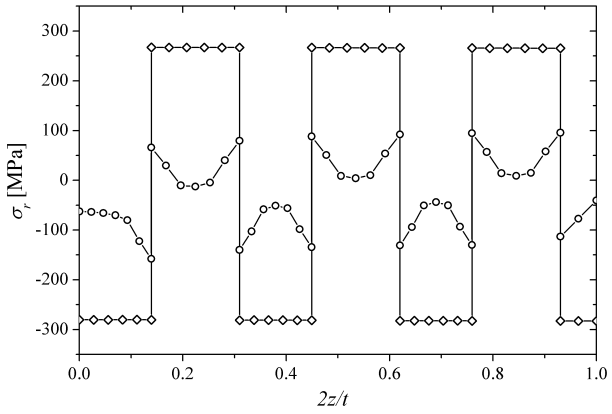

Figure 3.3: Center (squares) and near-edge (circles) stress maps, resulting from FE analysis. The former are presented as the σ_{xx} component, the latter as the average pressure $1/3\Sigma\sigma_{11}$

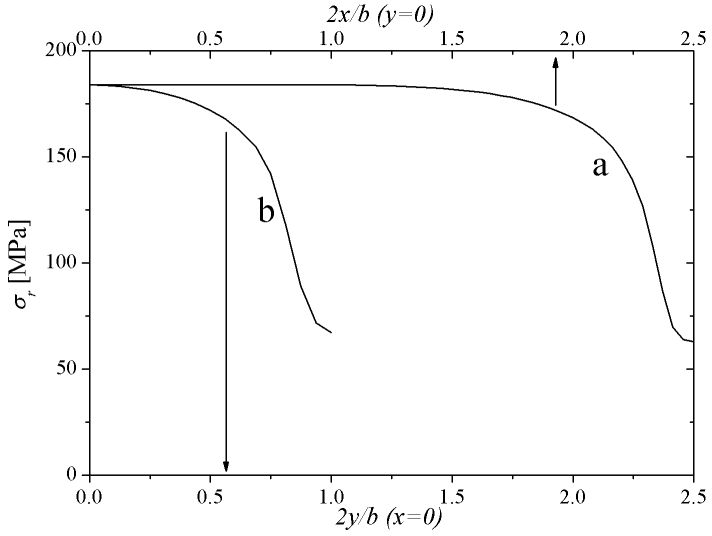

Figure 3.4: Uniaxial stress relaxation for the free surfaces at the edges along the a) x and b) y directions, both normalized over the sample width b, for $y = 0$ and $x = 0$, respectively

dimensions in the x and y directions (symbols as in Fig. 3.1). The zone of validity of the constant stress assumption confirms the importance, as observed in the methodology section 2.3, of performing the tests in the center of the sample, at a distance from the edge of at least twice the layer thickness.

3.3 Application: strength degradation

The strength degradation caused by contact brittle damage was evaluated by means of Finite Element analysis. The purpose of such simulations was to provide an additional tool for the evaluation of experimental results, reducing thus the uncertainties generated by the stochastic nature of fracture in brittle materials, enhanced in this case by the two-steps character of the test.

One load condition was chosen from the actual tests: cyclic loading with P_{max}=500 N, P_{min}=50 N, 10^4 cycles. In order to overcome in part the uncertainties derived by the results scatter, the entire test was replicated by FEM, divided in two steps:

1. Spherical indentation on stressed material
2. Bending test

The first part was formulated as a two-steps 2-dimension axisymmetrical model, in which the equilibrium condition of a cracked body subjected to 1) shrinking, 2) indentation was sought. In other word, straight cracks of arbitrary angle and length were included in the model, which was then subjected to the steps mentioned above. The stress intensity factors K_I and K_{II} were the output, and the crack geometry was varied iteratively until the equilibrium conditions

$$\begin{aligned} K_I &= K_{Ic} \\ K_{II} &= 0 \end{aligned} \tag{3.1}$$

was fulfilled. The same procedure, with no residual stress calculation, was followed to determine the cone crack length and angle in monolithic alumina.

It should be noticed that both the residual stress calculation and the cone crack geometry are simplified formulations of problems which are studied in deep in other sections (3.2 and 5, respectively); the former because the 2D model does not capture the complex stress distribution, the latter because the hypothesis of straight crack is not fulfilled, especially in presence of residual stresses, as it will be shown when befitting. Moreover, the effect of cyclic loading was neglected in the simulation for the lack of a proven model of crack propagation, therefore the resulting equilibrium cracks are expected to be shorter than the measured ones, and some length overestimation is also expected, because crack shielding is not included in the model, for sake of simplicity; therefore, it is considered, as a rough approximation, that the two effects compensate

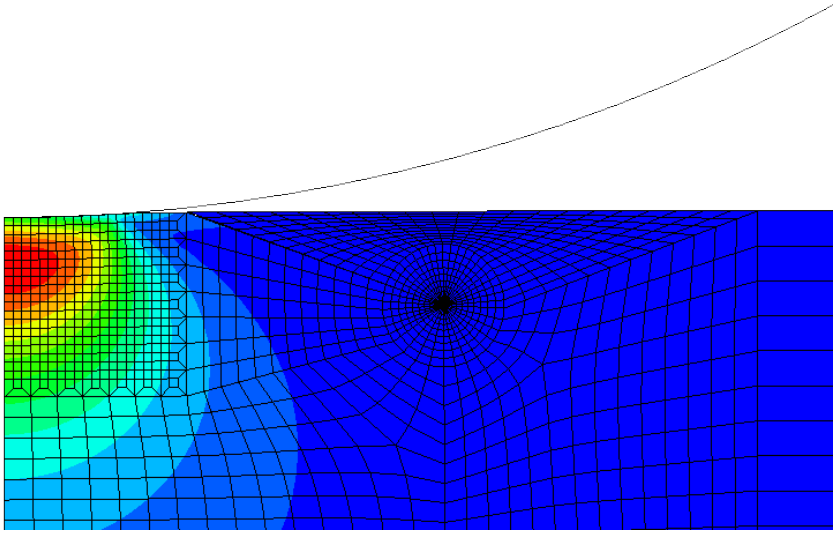

Figure 3.5: Mesh of the model for the cone crack equilibrium geometry. The crack is represented as straight, the indenter as a rigid sphere

in a certain extent each other, so that the resulting length is acceptable, under the assumption that the purpose of this section is to provide a qualitative assessment of the mechanism of strength degradation, without focusing on unreachable accuracy of the results; for this reason the models were built as simple as possible.

The cone cracks geometry thus obtained, and confirmed, within the measurement error, by experimental observations, were included in the second step, the simulation of the bending test. In this case, the stress distribution is expected to play an important role in the location of the "weak point" of the cracked sample, therefore a 3-dimensional linear model of actual A/AZ samples was created, with symmetries along the x and y axis, representing thus one quarter of the bar. Bending was simulated by a constraint corresponding to the inner span and an increasing load in the outer span. The mesh was homogeneous on the model, apart in the zone of the cone crack, where high refinement was necessary for the high stress gradient.

The mode of loading at the tip of the crack is mixed, therefore the output chosen for formulating the fracture criterion was the strain energy release rate G, calculated along a contour at the crack tip. The critical value was calculated as $G_c = K_{Ic}^2/E$, defined from the specific case of mode-I loading.

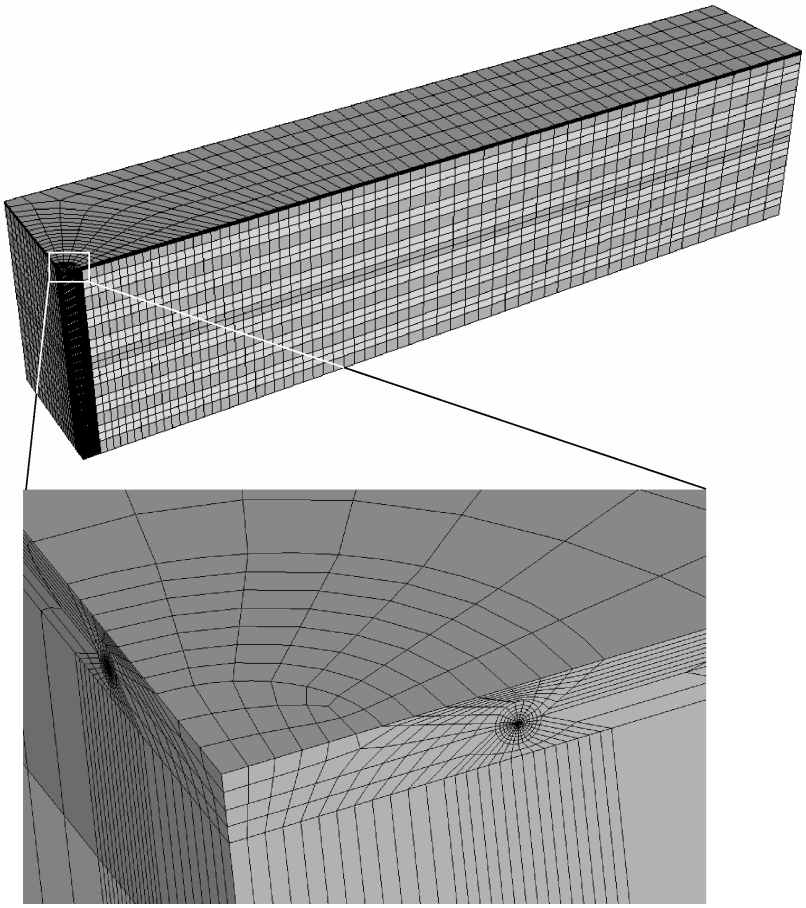

Figure 3.6: Mesh of the 3D model of bending test; in small a detail of the mesh at the cone crack is shown

3.4 Application: contact strength

Consistently with the original analytical formulation in eq. (2.7), failure from contact strength tests was treated as a critical-stress problem, rather than with the fracture mechanics formulations. A bidimensional Finite Elements model was developed, representing one quarter of a bar, whose geometry and size were taken from actual samples. A coding script was created in the Python built-in language to allow automatic generation of any symmetrical odd-layered structure, given the layers number and thickness. The validity of the model, including mesh convergence, was verified by simulating testing of monolithic materials and comparing with the analytical expression.

The mesh consisted of approx. 25000 quadratic elements, as established after mesh convergence tests, and was refined at the contact zone, where higher stress gradient was

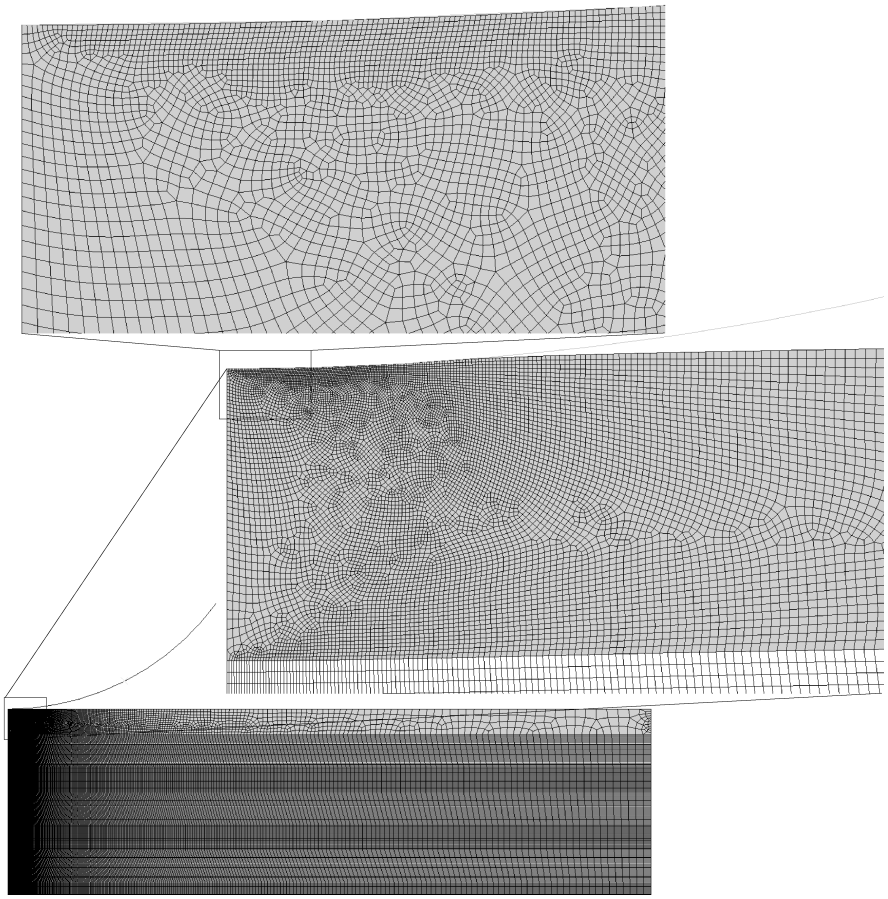

Figure 3.7: Typical mesh of the model for contact strength evaluation, with a detail of the contact zone

expected. The length of the bars was three times the thickness, guaranteeing negligible influence of the free boundary to the stress field [69]. The rollers were represented with a rigid analytical body, applying a progressive displacement on the bar surface. The corresponding load was calculated from the reaction forces at the roller. As for other calculations, a step of shrinkage was included for generating the residual stresses in the laminated structures, starting from the temperature of 1200°C, above which zirconia behave as plastic and therefore no stress is generated [81], to room temperature (30°C).

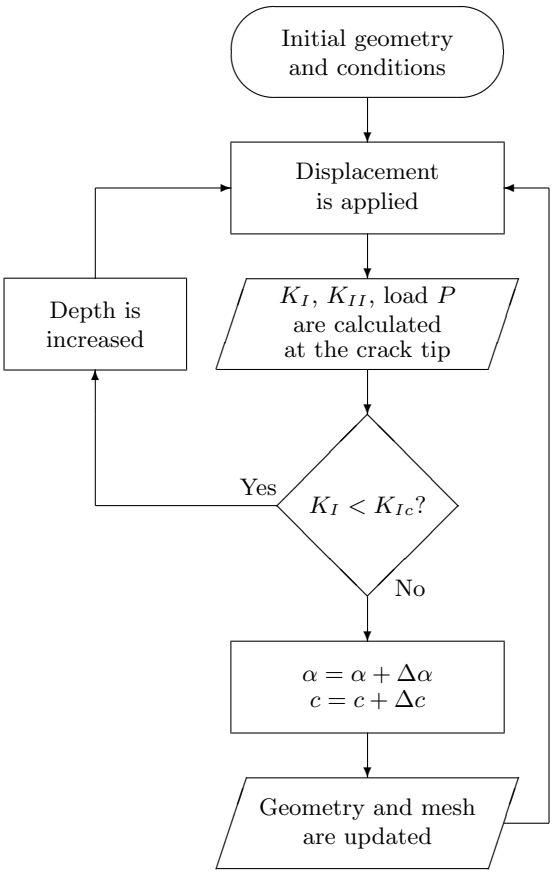

Figure 3.8: Flow diagram of the Python automatic incremental model of crack propagation

3.5 Automated Algorithm of crack propagation

An incremental FE model was developed, similar in some aspect to the one proposed by Kocer [38], for simulating crack propagation. The Python code allowed interacting both with the pre-processor and with the output reading, making it possible to modify iteratively the model, depending on the output of the previous step.

An outline of the model is presented in Fig. 3.8. The algorithm was divided in three scripts:

`propcrack.py` the algorithm itself, reads the user input, check the propagation conditions and writes the output

`model.py` creates automatically the model with the given input and the step-wise crack geometry

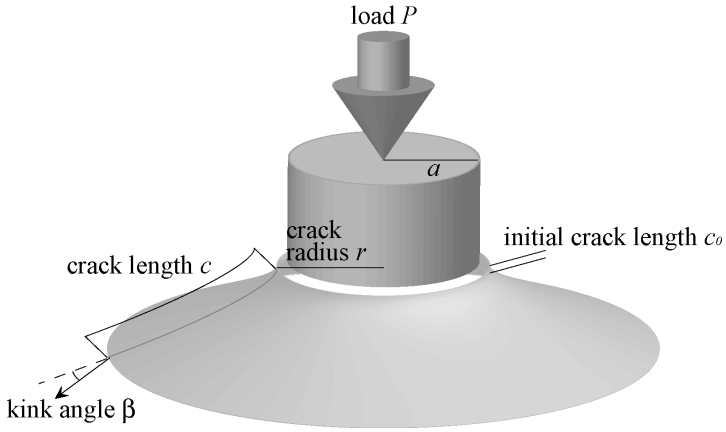

Figure 3.9: Scheme of flat punch indentation

`output.py` calculates the output of every step (stress intensity factors, propagation angle, indentation load), including external effects

3.5.1 Model of punch indentation

The generation of the model was conducted on the `Abaqus/CAE` module by the `model.py` script, according to the following outline:

- Creation of the body, including the cone crack
- Partition of the body for the subsequent mesh generation
- Definition of the boundaries and symmetry conditions and of the load
- Seeding of the edges and faces and mesh generation
- Choice of the output and of the calculation parameters

Flat punch indentation was represented on an axial-symmetric model on `Abaqus` version 6.6 [80], represented schematically in Fig. 3.9 by applying vertical displacement h on the nodes of the contact zone of radius a. The corresponding indentation load was calculated from the reaction forces at the same nodes. It was assumed that indenting either with a sphere or a flat punch produces similar results in terms of cone crack propagation [33]. A short crack of length c_0 (typically $a/c_0 > 100$) was placed near the contact zone. After the first crack increment c_0 is replaced by the updated crack of length $c_0 + \delta c = c$ and so on.

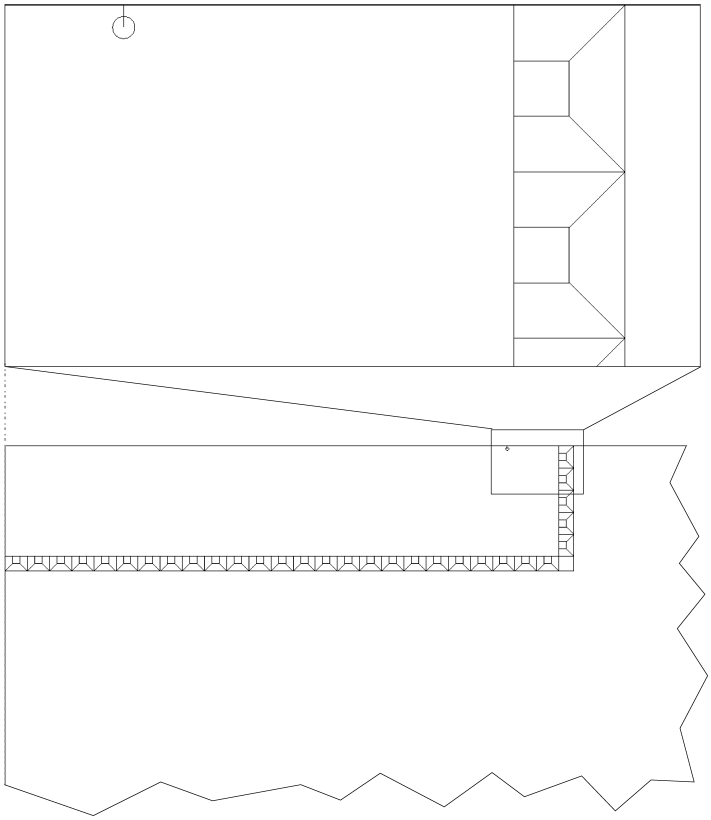

Figure 3.10: Initial geometry of the flat punch model. r_0/a, P, δc are user-defined input

The materials properties were represented as linear elastic, with values taken from previous studies [20]. The crack tip singularity was represented with collapsed quadratic nodes, as shown in Fig. 3.11. The stress intensity factors on encircling contours yielded the propagation direction, as explained in section 3.5.2. In order to guarantee lower computation time as well as accuracy, the mesh was highly inhomogeneous, finer in the contact zone and around the crack, coarser where the stress gradient is lower. For that, a transition from fine (near the contact zone, enveloping the entire crack) to coarse mesh was included, whose size was established on every step as a function of the crack tip position.

Additional loading types can be taken into account within this script file, such as, in the study of ceramic laminates, the residual stresses, as a constant pressure acting on the layer edge. As an additional feature, the possibility of applying different stress distributions was included, as user-defined `fortran` functions. Such feature resulted

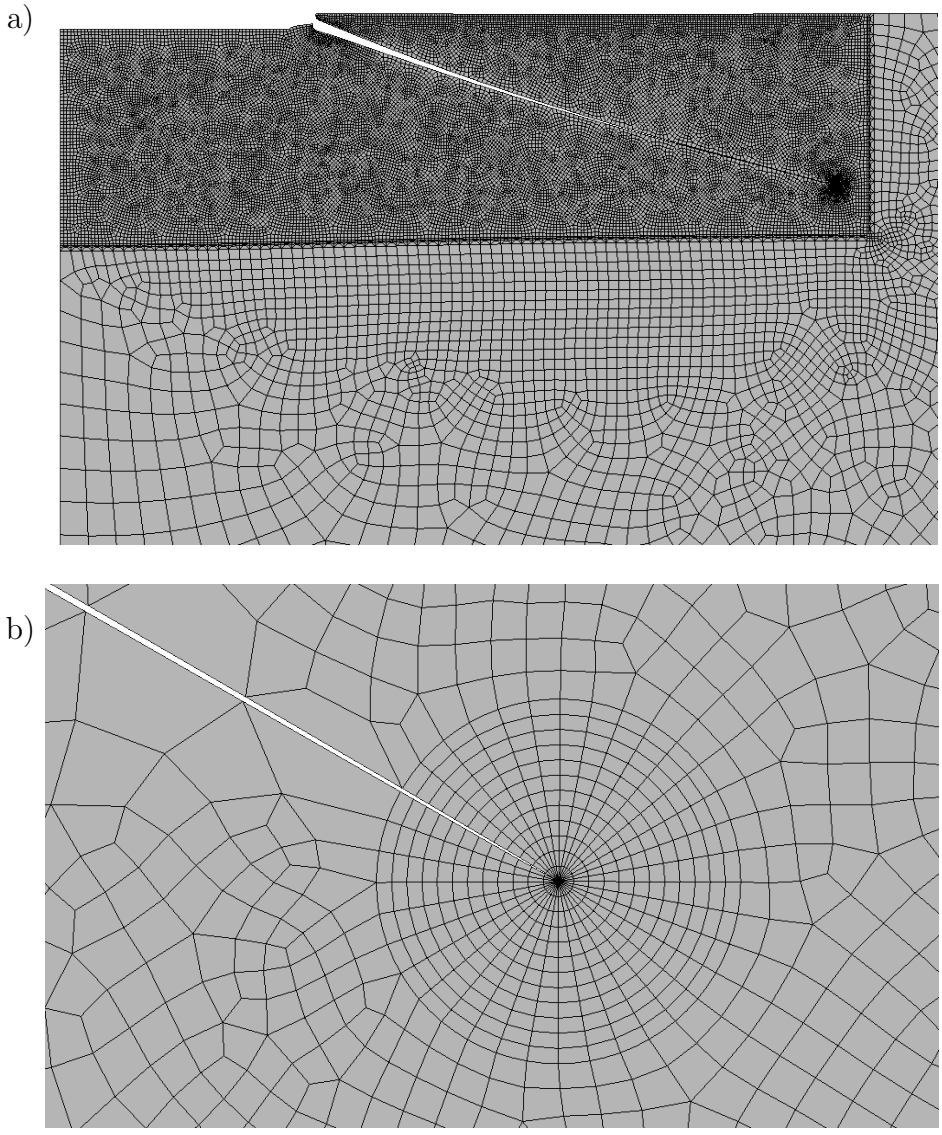

Figure 3.11: a) Mesh of a well-developed crack and b) mesh refinement with collapsed nodes for the stress intensity factors measurements at the crack tip

to be unnecessary during the study of ceramic laminates, nevertheless there are cases in which the assumption of homogeneous residual stresses is not applicable, such as in strengthened glasses.

It is worth highlighting that, although the model was expressly designed for simulating spherical indentation, any type of loading which is "simple enough" to be generated and updated automatically with script commands can be inserted in the automatic procedure of crack propagation.

3.5.2 Output handling

The script `output.py` reads the file containing the results of the calculation and provides the output which rules the crack propagation:

- The propagation direction, expressed in general terms as the kinking angle

$$\beta = f\left(K_I, K_{II}, K_\Phi\right) \tag{3.2}$$

  where Φ represents all externally applied contributions, such as shielding effect, as it will be presented in section 5.1.

- The penetration depth increments, from the toughness condition

$$K_I + K_\Phi > K_{Ic} \tag{3.3}$$

  again including all external effects Φ.

- The indentation load, as the sum of the reaction forces at the contact nodes.

More in detail, K_I, K_{II} were calculated by the software from the displacement field along contours around the crack tip. The tip itself was represented by quadrilateral elements, with an edge collapsed corresponding to the crack tip. The strain singularity $\varepsilon \propto r^{-1/2}$ was represented by displacing the midside nodes of the radial edges to one quarter of the edges, as shown in Fig. 3.12

Several criteria for the prediction of the propagation angle β are built in the software [80]: the maximum tangential stress (MTS), the maximum energy release rate (MERR) and the $K_{II} = 0$ criteria; however, in order to guarantee higher flexibility in the output handling, and to include the external effects mentioned in Eq. (3.2) as K_Φ, it was decided

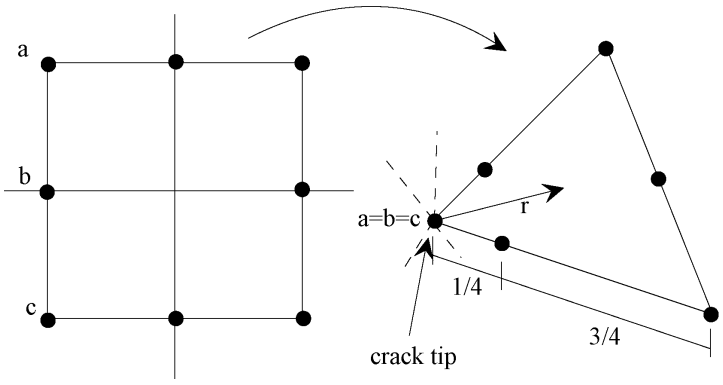

Figure 3.12: Collapsed vertex nodes and moved midside nodes for representing the crack tip and the strain singularity of perfectly elastic materials

to employ an alternative definition of the kink angle β, calculated from the raw output, namely:

$$\beta = -2K_{II}/K_I \tag{3.4}$$

valid for small β [82, 83]. In the studied case, such condition may be not fulfilled for short cracks, because the stress mixity is high and, therefore, the kink more pronounced. Since the most relevant portion of the crack is straight, if the increments are small enough, as it was determined by convergence tests, the approximation is considered acceptable. Such assumption was confirmed by calibration with a reference material, soda-lime glass ($E = 72\,GPa, \quad \nu = 0.21$), which gave results in agreement with literature [39].

In a similar way, it was possible to induce the model to increase the penetration depth h to a new value h', and therefore the indentation load, whenever the condition in Eq. (3.3) was not fulfilled. The depth increment was calculated so that the total stress intensity factor approached the value of toughness; from the simple relation $K \propto P$:

$$h' = h\frac{K_{Ic}}{K_I + K_\Phi} \tag{3.5}$$

so that $K_I + K_\Phi = K_{Ic}$, the rigorous condition for stable propagation, is fulfilled.

Although the model was designed on the purpose of studying cone crack propagation, the possibilities offered by the interaction with the model itself and the handling of the output allows to conduct different kind of studies. As an example, if a short-enough initial crack is imposed, to reproduce a defect or flaw existing in the surface, it is possible to evaluate the strain energy release dependence on the flaw size and location, and on many additional effects, such as residual stresses.

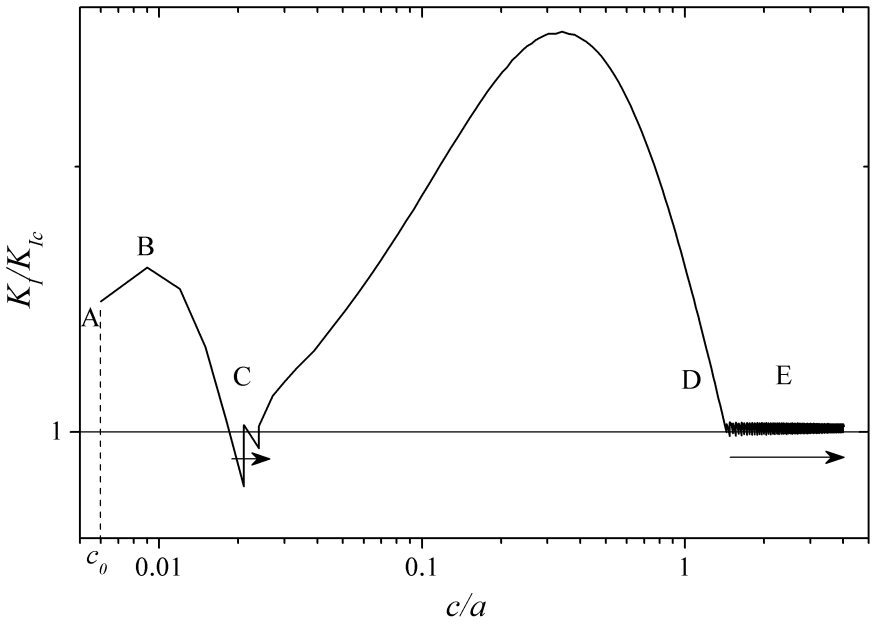

Figure 3.13: Typical evolution of the stress intensity factor K_I with the cone crack propagation. Arrows indicate increments in load

3.5.3 Input normalization

Although the input handling of the model allows varying, among other parameters, the indentation characteristics (mainly the contact radius a), the size and mesh seeding were optimized for an initial contact radius $a_n = 100\mu m$; in order to simulate actual experiments benefitting of optimal simulation parameters, it was necessary to normalize the relevant properties (stress intensity factors, crack length) to the experimental contact radius a. A normalizing parameter $\kappa = a_n/a$ was included in the variables definition in the `propcrack.py` script, to modify the properties which depends on a: the indentation load P, the material toughness K_{Ic} and toughness parameters, such as the shielding parameters that will be defined in the next section ($K^{\infty}_{I,II}$, λ), by the following relations:

$$\begin{aligned} K_{\Phi}n &= \sqrt{\kappa}K_{\Phi} \\ P_n &= \kappa^2 P \\ \lambda_n &= \kappa\lambda \end{aligned} \tag{3.6}$$

with K_{Φ} representing all the toughness-related quantities and the lower index n indicating the normalized quantities.

This feature broadens the range of cases suitable to be represented by the automatic algorithm, both within the frame of ceramic laminates herein addressed (such as, influence of indenter radius, microstructure features) and to any other substrate-indenter system, presenting almost any scale of geometrical and intrinsic characteristic sizes.

3.5.4 Example of crack propagation

The stress intensity factor evolution as a function of the crack length, obtained from Finite Elements simulation, is presented in Fig.3.13. The shape, for a constant load, is in agreement with the classical solution reported in literature [48], and additionally in this case the propagation was calculated considering unstable and stable propagation branches: at the point A a small crack is present; K_I is higher than the toughness, therefore the crack propagates under a constant load. After reaching a maximum (point B) K_I decreases to the value of the toughness; it is therefore necessary to increase the load until the minimum is reached (point C). After that, unstable propagation begins, until the fracture toughness is reached again (point D). The subsequent propagation is stable, represented analytically by the classical Roesler equation

$$K_{Ic} = \chi \frac{P}{c^{3/2}} \tag{3.7}$$

and in this simulation by step-wise increments either in penetration depth or crack length (saw-shaped zone E).

3.5.5 Example of crack initiation

As an additional verification, considering now a constant indentation load, the strain energy release calculation by Fischer-Cripps [24] was reproduced. The algorithm was modified to execute a short amounts of increment, and to produce an output file including the fracture energy G, which was associated to the corresponding crack size size and starting radius. The results are in good agreement with the cited work, as shown in Fig. 3.14, apart from the difference caused by the fact that the energy is calculated on the cracked body, and not from the pre-existing stress field as in the cited reference. The different approach has not significant influence on the results because the crack here considered are short enough, and the crack paths can be approximated with the trajectories of the third principal stress, although some discrepancy can be seen for the longest crack lengths.

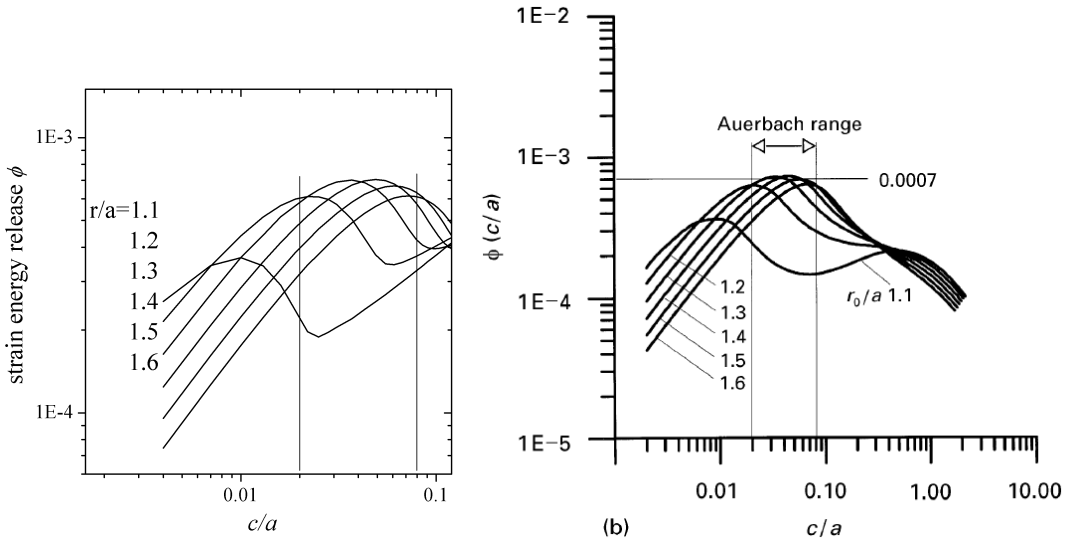

Figure 3.14: Fracture energy as a function of the crack length for a range of starting radii, a) from the presented FE study and b) as extracted from [24]

CHAPTER 4

Surface damage by Hertzian indentation

As said in the introduction, the resistance to the formation of surface damage is a critical issue in many surface-focused applications. In most cases the presence of, albeit small, cracks is sufficient for discouraging further utilization of the component. In other cases, the presence of such damage can be taken as a warning of upcoming failure. However, the design philosophy of damage tolerance, nowadays common in many high-level applications, is not affordable in other fields, such as bio-replacement interventions, which require damage to be completely prevented. A similar aspect of the fatigue-related contact resistance is that of quasi-plastic damage, which can produce grain pull-out, detrimental for the tribological properties, before visible brittle damage appears.

4.1 Ring crack appearance

Damage produced by spherical indentation can present brittle or quasi-plastic character depending on several parameters, among them the microstructure and the indenter size. For this reason, it is difficult to define as "brittle" or "quasi-plastic" a material, without considering such parameters.

Nevertheless, if the indenter radius R is large enough, alumina can be considered mainly brittle, in that the first visible damage under monotonic indentation is ring

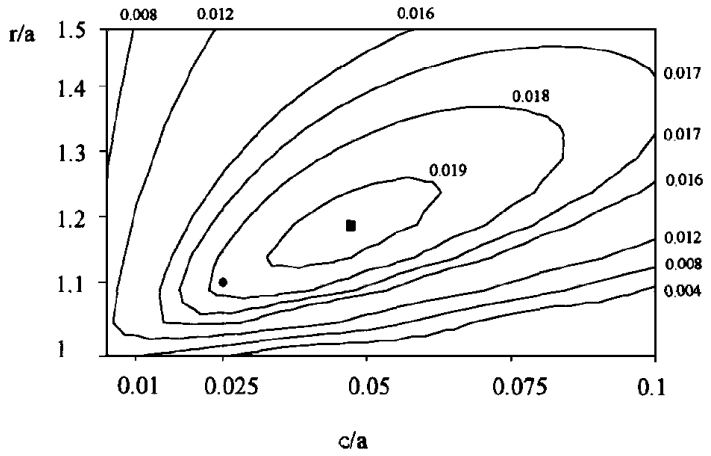

Figure 4.1: Contours of normalized K_I as a function of the relative crack depth c/a and position r/a [36]

cracking [55], and for this reason is herein held as the first damage parameter for the comparison of monolithic with multilayered materials.

4.1.1 Monotonic loading

The critical load for appearance of cone crack can be calculated, following Warren and coworkers [28, 36], as

$$P_c = \Gamma \frac{K_{Ic}^2 R}{E'} \tag{4.1}$$

with Γ a dimensionless constants that formally depends on the elastic properties of the substrate and indenter materials and on the friction coefficient between them, but is related also to the relative initial defect size and position, as it corresponds to the maximum of the geometry factor, in other word to the most favorable combination of the c_0/a and r/a parameters, as illustrated on Fig. 4.1.

Assuming, therefore, that the ring crack propagates from an existing favorably-oriented defect, representable as a semi-elliptical crack of length $2b$ and depth c shown in Fig. 4.2, the stress intensity factor can be expressed in terms of peak indentation pressure p_{max}, as

$$K_I = p_{max}\sqrt{\pi a}\mu\left(\frac{c}{a}\right) \tag{4.2}$$

where p_{max} is given by:

$$p_{max} = \frac{3P}{2\pi a^2} \tag{4.3}$$

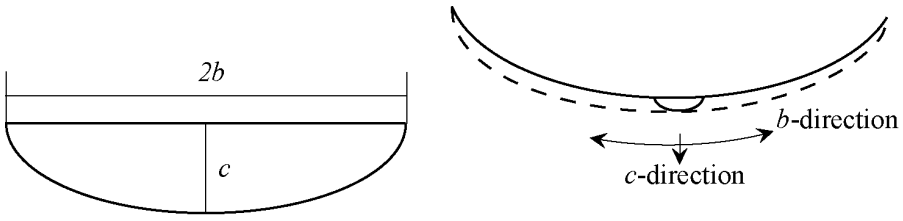

Figure 4.2: Scheme of semi-elliptical crack, origin of the ring crack under Hertzian indentation

The contact radius a can be expressed as function of the load P, the radius of the indenter sphere R and the composite Young modulus indenter-material E^*, as:

$$a = \left(\frac{3RP}{4E^*}\right)^{1/3} \tag{4.4}$$

with:

$$\frac{1}{E^*} = \frac{1-\nu_m^2}{E_m} + \frac{1-\nu_i^2}{E_i} \tag{4.5}$$

being E and ν the Youngs modulus and Poisson's ratio of the material (subscript m) and the indenter (subscript i). The function μ, as well as Γ, is a dimensionless function that depends on the relative crack position, Poisson ratio of the material, crack ellipticity and crack depth. Combining Eqs. (4.2)-(4.4), the stress intensity as a function of the applied indentation load can be expressed as:

$$K_I = \left(\frac{3E^*P}{\pi R}\left(\mu(c/a)\right)^2\right)^{1/2} \tag{4.6}$$

The function μ changes as the crack grows in both circumferential and depth directions. It has to be noted that during the crack growth, the stress intensity factor in the b-direction is larger than the stress intensity factor in the c-direction, and only in some cases $K_I^c = K_I^b$, and when such condition is fulfilled the crack grows in both directions. However, as the crack progresses in the depth direction, the value of $\mu(a/c)$ changes drastically and the b-direction is favoured again. That implies that ring cracks penetrate only slightly on the material while they grow along the perimeter.

For the case of a material with residual stress, the value of μ is affected by the relative value of these residual stresses with respect to the peak indentation pressure [84]. If this relative value is lower than 20%, the modified value of μ by the residual stresses, labelled as μ', can be related through the value of μ without residual stresses

by the approximation:

$$\mu' = \mu B^{-\sigma_r / P^{1/3}} \tag{4.7}$$

where B is a constant, which depends on the elastic properties of the material and the indenter, and has to be calibrated numerically.

The values of critical load obtained with a 2.5 mm radius indenter were $P_c^{MA} = 607 \pm 50$ N, $P_c^{A/AZ} = 675 \pm 50$ N and $P_c^{A/2AZ} = 725 \pm 50$ N, respectively, meaning that all were calculated as the ΔP=100 N range in which ring crack appearance was detected.

4.1.2 Static and cyclic loading

The results, obtained with the procedure explained in section 2.3, of the static and cyclic tests are reported in Fig. 4.3, as the ranges of time and number of cycles necessary for the appearance of ring crack for a given load.

It can be seen that the laminated composites present a better resistance to damage than pure alumina, both under constant and cyclic loading. Moreover, it can be seen that, in both cases, A/2AZ presents better results than A/AZ. This can be correlated to the existence and amount of compressive residual stresses at the surface in the laminated materials, being the A/2AZ material the one with the highest magnitude of residual stresses. Additionally, it is seen that the relationship between load and time or number of cycles may be adjusted by a powerlaw relationship. The slope of the $\log - \log$ representation of the data is comparable among the three materials, and data are only displaced upwards with increasing amount of surface residual stress. There is however a slight disagreement with the A/2AZ material, which can be attributed to the experimental scatter produced at high loads and low times. The fact that the slopes are comparable, suggests that the micromechanisms of damage in all the materials are equivalent, and that the compressive residual stress decreases the apparent stress intensity factor. This equivalent behaviour is consistent with the fact that all materials have a comparable microstructure and therefore, the chemical and microstructural mechanisms that provoke damage can be considered as similar for the laminates and the MA.

In the case of static loading the mechanisms of degradation can be attributed to stress corrosion cracking: when the load is applied, the natural flaws are opened and water vapour penetrates to the crack tip, where it reacts with the glass particles of the alumina, diminishing thus the cohesive strength of the material and enlarging the crack.[85]

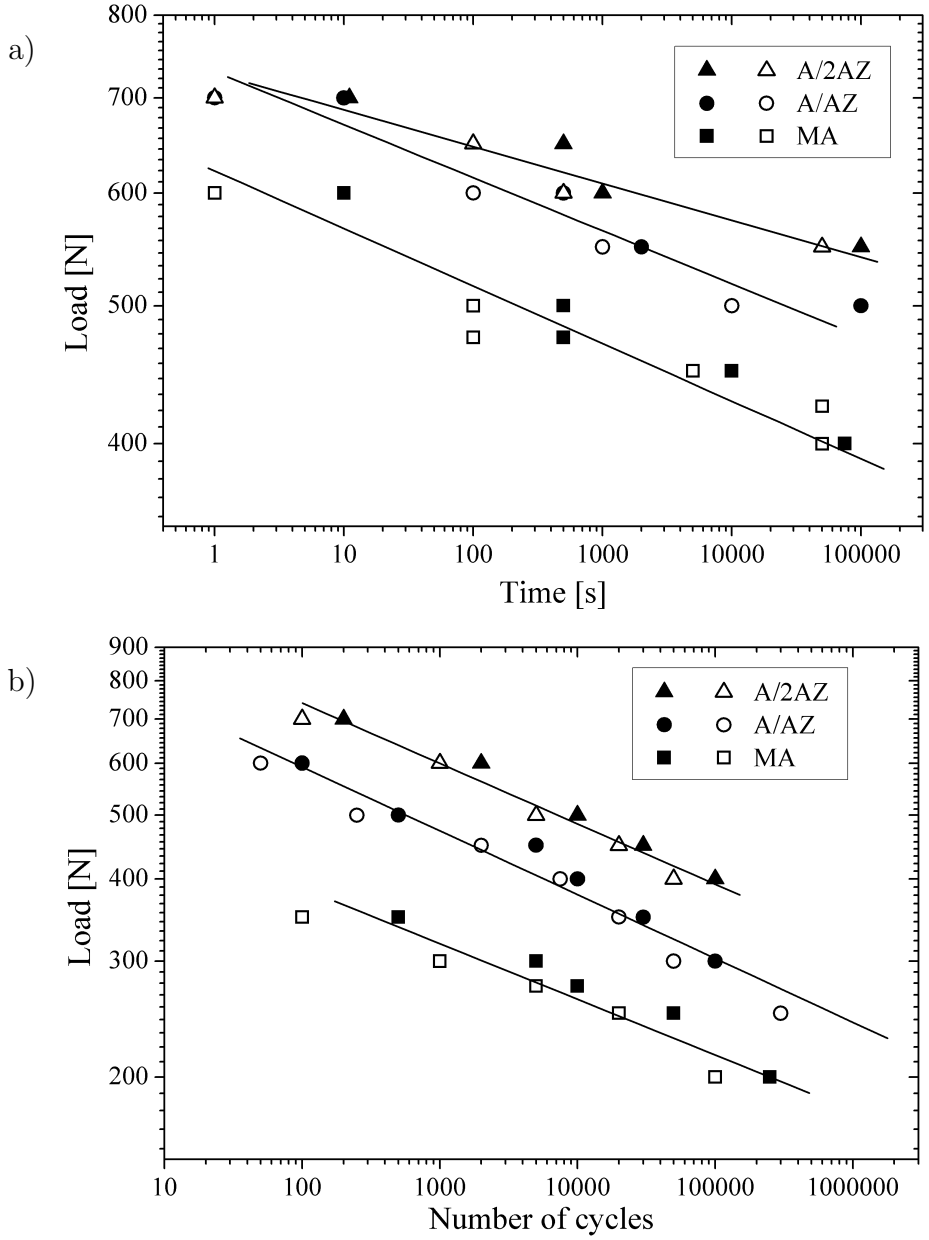

Figure 4.3: Indentation load against time or number of cycles under a) stress corrosion cracking and b) cyclic fatigue tests. Empty points indicate no apparent damage, filled points the existence of well-developed ring crack

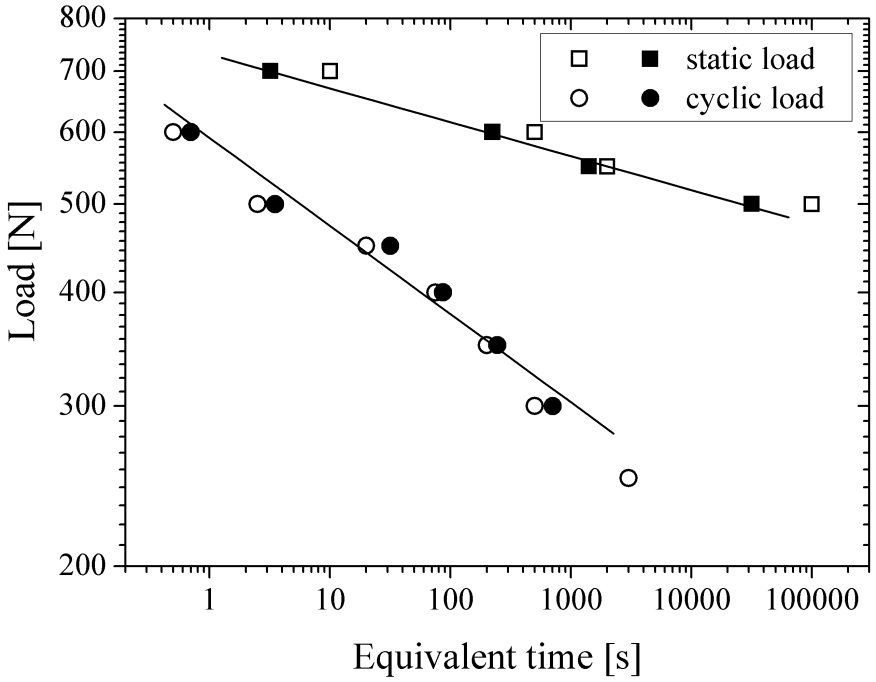

Figure 4.4: Comparison between the damage evolution under static and cyclic loading, represented as applied load against equivalent time, for the A/AZ laminated composite.

It is also seen that all three materials under cyclic loading (Fig. 4.3b) present damage much earlier than under static loading. This is better seen in Fig. 4.4, where the behaviour under both static and cyclic loading of the A/AZ composite is presented, and where the number of cycles of cyclic loading have been converted into equivalent time (t_{eq}), defined as:

$$t_{eq} = I_c \frac{N}{f} \tag{4.8}$$

where N is the number of cycles, f is the frequency of the test (10 Hz in our case) and I_c is a translation constant that takes into account the effective time when the stress intensity factor is above the threshold value for stress corrosion cracking. In Fig. 4.4, the value of I_c has been taken equal to 0.1 [45], corresponding to a subcritical crack growth exponent of 30.

If the same degradation mechanism were operating under cyclic and static loading, the experimental results of both cyclic and static loading would be equal after conversion of number of cycles into effective time. In this case, no fatigue effect would appear during cyclic loading. However, this is not the case, as cyclic loading produces damage much earlier than static loading. Moreover, it has to be noted that degradation under cyclic

loading would be higher than under static loading even if the effective time was defined as the total time of the test, $t_{eq} = N/f$ ($I_c = 1$), assuming the limit case where stress corrosion cracking is acting all the time and is not related to the crack opening.

There appears to be, therefore, a real fatigue effect, consequence of the cyclic loading and the degradation observed is not only due to the stress corrosion cracking, in accordance with previous studies in alumina [86, 87, 88, 89]. Moreover, the crack growth rate in our systems may be larger than the growth rate measured in larger specimen configurations because the fatigue effect can be enhanced by a short crack effect. This short crack effect is due to the fact that the crack is shorter than the fracture process zone, defined as the volume where the crack-tip shielding mechanisms occur, that are the responsible for the R-curve behaviour. In the case of alumina, the main toughening mechanism is grain bridging [90, 91]. In the case of Hertzian indentation, the crack is short not only in the perimeter direction of the ring, but specially in the depth direction, as the crack is just some micrometers deep because of the sharp gradient in tensile radial stress with depth, which becomes compressive just after a short depth [92, 29]. That is, while in the case of stress corrosion cracking the fracture process zone develops without impediment, in the case of cyclic loading this fracture process zone degrades continuously, reducing the effect of the grain interlocking, and, therefore, the R-curve. The fatigue effect can be clearly seen in Figs. 4.5 and 4.6, where the Hertzian crack produced under subcritical static loading (Fig. 4.5a and Fig. 4.6a) and cyclical loading (Fig. 4.5b and Fig. 4.6b) are presented, observed by optical and SEM microscopy, respectively. In the former ones, it is appreciated that the crack runs smoothly, while in the latter it is appreciated that the crack runs tortuously, which indicates that the bridging in that region of the crack have degraded through grain sliding[86] and rotation[89].

4.1.3 Crack growth analysis

The subcritical crack growth rate (dc/dt) can be related to the applied stress intensity factor through a logarithmic relationship:

$$\frac{dc}{dt} = v_0 \left(\frac{K_I}{K_{Ic}} \right)^n \tag{4.9}$$

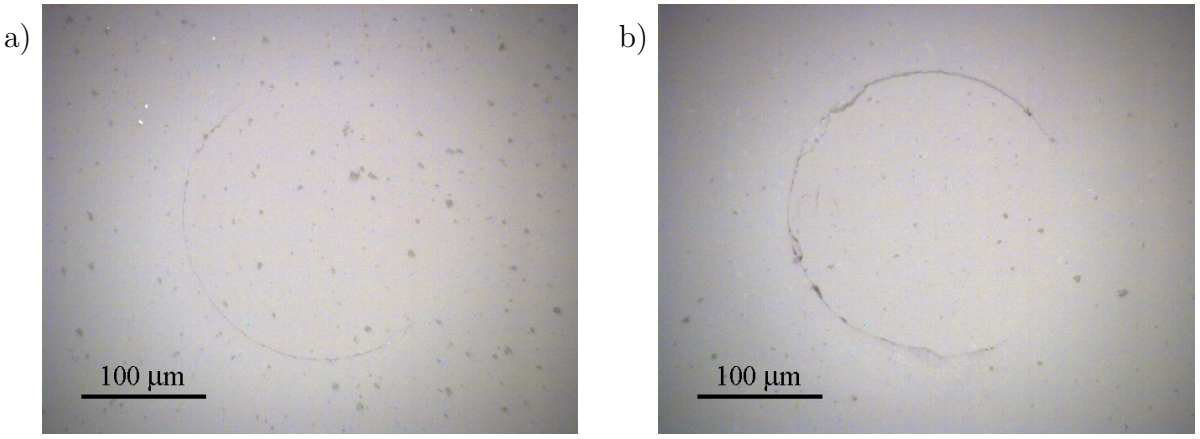

Figure 4.5: Optical pictures of typical ring cracks of A/AZ material produced under: (a) static loading and (b) cyclic loading. Ring crack in panel (b) is not perfectly circular and regions of grain bridging are visible.

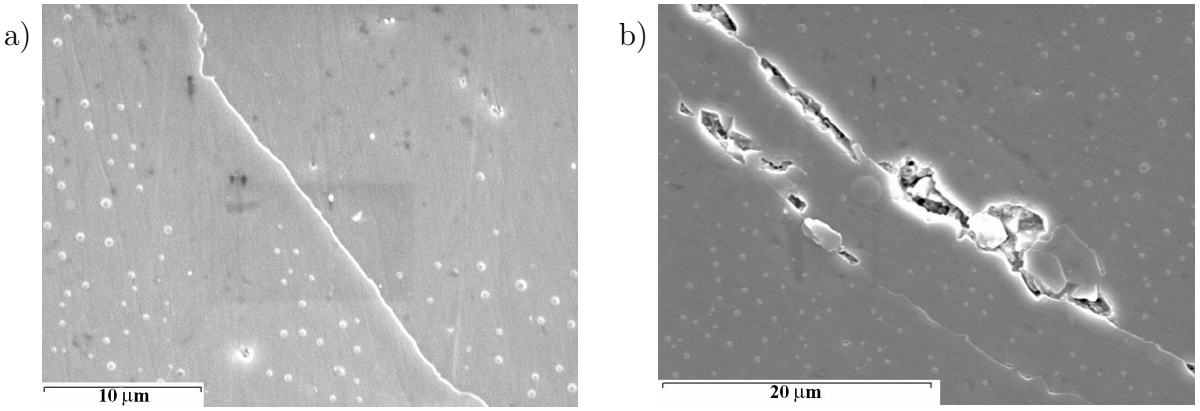

Figure 4.6: SEM pictures of typical ring cracks of A/AZ material produced under: (a) static loading and (b) cyclic loading. The crack in panel (a) is smooth, while in panel (b) the grain removal typical from fatigue mechanisms of ceramics is evident.

where v_0 is a material-dependant constant and n is the crack velocity exponent. By inserting Eq. (4.6) in Eq. (4.9), and integrating, we obtain:

$$\int_{\theta_i}^{\theta_f} \frac{d\theta}{\left(\mu\sqrt{c/a}\right)^n} = v_0 \left(\frac{4E^*}{3R}\right)^{1/3} \left(\frac{3E^*}{\pi R K_{Ic}^2}\right)^{n/2} P^{(3n-2)/6} t \tag{4.10}$$

where θ is the radial coordinate of the ring crack, θ_i is the initial defect size, that can be taken as 0, and θ_f the final defect size, that in the case that the ring crack is fully developed can be taken as $2\theta_f{=}2\pi$. The left size of the equation is dimensionless and almost independent of the applied load, for the values of applied load considered here.

Therefore, Eq. (4.10) can be reduced and approximated to:

$$P^{n/2}t \approx A \tag{4.11}$$

where A is constant for that given material and indenter.

A similar equation can be derived for materials presenting residual stresses, as a combination of Eq. (4.7) and (4.11):

$$P^{n/2}B^{-\sigma_r n/2P^{1/3}}t = A \tag{4.12}$$

The values of residual stress in the studied cases are around 6% of the peak pressure, therefore Eq. (4.12) can be approximated as:

$$P^{n/2}\left(1 - \frac{\sigma_r n}{2P^{1/3}}\ln B\right)t = A \tag{4.13}$$

That is, when residual stresses are small, the experimental data are shifted to an higher load, in comparison with the unstressed material. If the range of loads is not too large, this shift will appear almost constant for all the values of P, (i.e.) the apparent slopes of the experimental data will appear equal for the stressed and unstressed materials. For larger range of applied loads, the apparent slope will be affected by the residual stresses. It important to note that the crack velocity exponent n is not affected by the residual stresses, as its value is given by the chemical interaction between the material and the medium.

If the data presented in Fig. 4.3a are fitted with Eq. (4.12), a value of n=53±9 is obtained as an average of the slopes of all three materials. This value is in reasonable agreement with the values of stress corrosion cracking exponent previously reported in literature, between 40 [93] and 60 [94].

We can follow a similar reasoning for the case of cyclic loading of alumina, and arrive to similar relationships as Eq. (4.11). Starting from the Paris law:

$$\frac{dc}{dN} = DK_{max}^{m} \tag{4.14}$$

where m is the Paris law exponent, D is a constant and K_{max} is the maximum applied stress intensity factor, we can arrive to the relationship

$$N_f P_{max}^{m/2} = M \tag{4.15}$$

where N_f is the number of cycles to failure, P_{max} is the maximum applied load and M is a constant. Alternatively, if we start from the modified Paris law:

$$\frac{dc}{dN} = FK_{max}^{p}\Delta K^{q} \tag{4.16}$$

being p and q exponents and F a constant, we arrive to the relationship:

$$\left[P_{max}^{p/2}\left(P_{max}^{1/2}-P_{min}^{1/2}\right)^{q}\right]N_f = L \tag{4.17}$$

with L a constant.

Data presented in Fig. 4.3b can be fitted by Eq. (4.15), and the mean slope of the three materials can be used to evaluate the value of the exponent of the Paris law, obtaining m=22±4. The values obtained are in relatively good agreement with literature. For example, Guiu and coworkers report values of m between 13 and 20 [86, 87], Healy *et al.* report a value of m of approximately 30 [88].

In order to evaluate the parameters of the modified Paris law, additional tests were performed on the A/AZ multilayer maintaining either the maximum load or the load amplitude constant, as mentioned in section 2.3, p. 35. The results, presented in Fig. 4.7,were used to obtain the values of p and q, through Eq. (4.17) without considering residual stresses, giving p = 19.0±2.8 and q = 2.4±0.4, which are again in accordance with literature, where p is always larger than q.

Hence, it is seen that, despite the approximate nature of Eqs. (4.12), (4.15) and (4.17), they yield stress intensity exponents that are relatively similar to values reported in the literature, taking in mind that the experimental data do have an inherent high scatter which may affect the value of the exponents and that these equations are approximations for small load ranges and relatively small values of residual stresses at the surface.

4.2 Severe damage

The onset of visible damage in alumina-based composites can be analysed in terms of brittle fracture; however the response to more severe damage is affected by other deformation mechanisms, typically related to microcracking (as mentioned in section 1.7), in other words to quasi-plasticity, which can have an effect on the subsurface of the material but also influence the surface resistance. For this reason, the surface damage caused by a high number of cyclic contact loading was studied in MA and A/AZ, in order to highlight the differences in terms of quantity and type of damage, and relate them to the modifications provided to the stress field by the presence of the laminated structure.

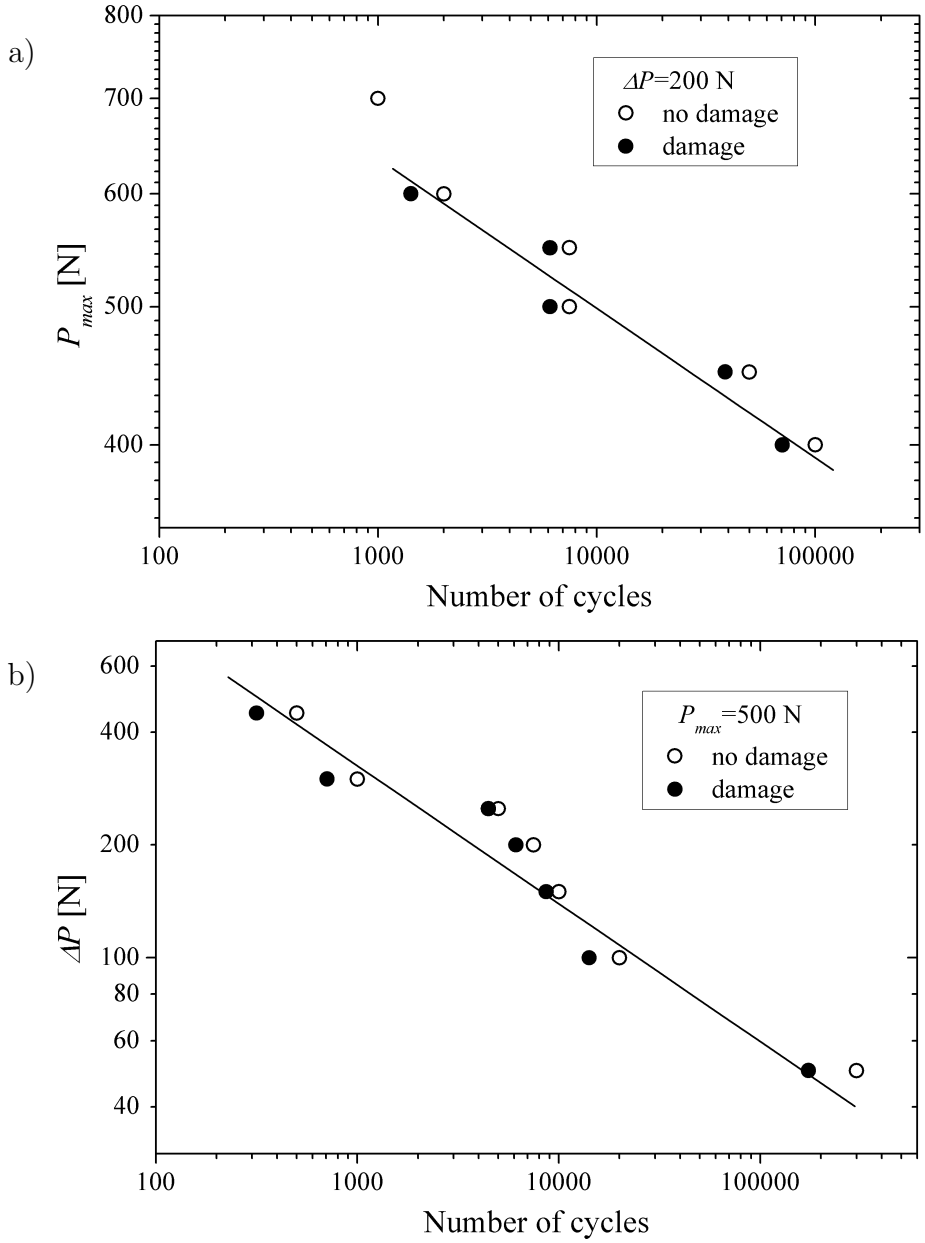

Figure 4.7: Cyclic loading tests of A/AZ laminate composite with: (a) difference between maximum and minimum load constant, with maximum applied load against number of cycles; (b) constant maximum load, with ΔP against applied number of cycles.

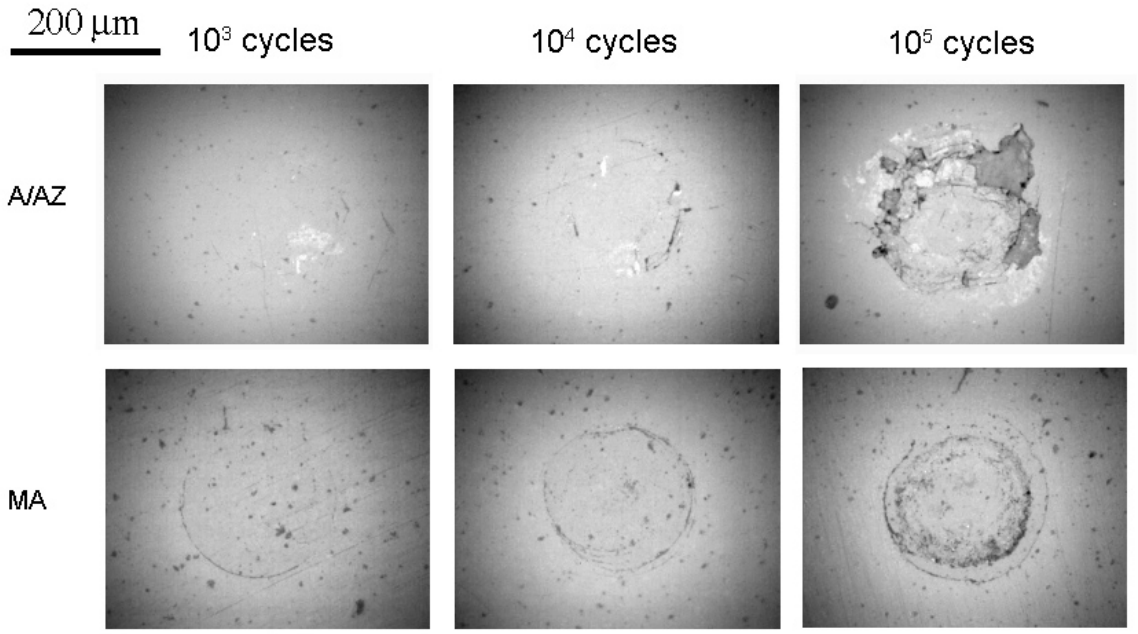

Figure 4.8: Damage produced in A/AZ and MA by Hertzian fatigue tests under load of 500 N and different numbers of cycles. Although A/AZ has a better resistance to appearance of ring crack, it presents an apparent higher surface degradation (chipping) for severe conditions (N = 10^5 cycles).

Fig. 4.8 presents the surface damage obtained for different number of cycles (N = 10^3, 10^4 , 10^5) on MA and A/AZ for a fixed maximum load of 500 N. At a low number of cycles (N = 10^3), it is seen that a ring crack appears in the alumina, while there is little appreciable damage in the A/AZ material. For an intermediate number of cycles (N = 10^4), the cracking in the alumina becomes more severe, while there is only minor ring cracking in the A/AZ. These results are consistent with what shown in the previous section, that laminated materials present better resistance to contact damage.

However, after a large number of cycles (N = 10^5), the type of damage is essentially different in the A/AZ laminated composite than in the monolithic alumina: while in the alumina, secondary ring cracks appear at the surface, together with radial cracking, in the A/AZ material there is a spalled off surface around ring cracking, in other words there is a mild chipping in the contact area.

This may be due to the fact that quasi-plastic damage under contact loading is

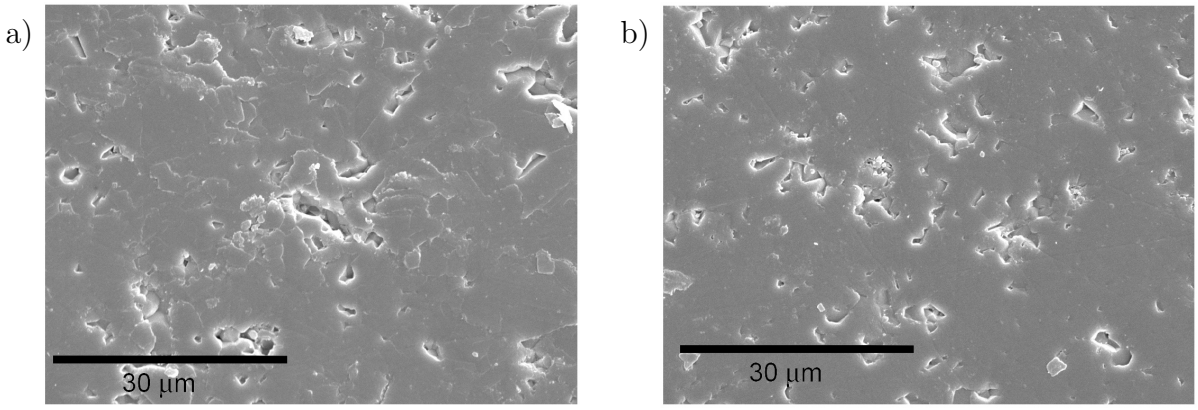

Figure 4.9: Scanning electron microscope pictures of the alumina layer in A/AZ composite showing: (a) damage zone underneath the indenter, where the severe microcracking produced by shear loading can be appreciated (b) undamaged microstructure of the same material far from the indentation site. Both pictures have been taken at a depth of 50 μm from the surface.

enhanced, with respect to monolithic alumina, due to the higher apparent toughness of the laminated material. The presence of a quasi-plasticity can suggest the formation of a shear-driven microcracking volume under the contact area, which is cause of inelastic deformation.

Fig. 4.9 presents the microstructure observed in the A/AZ material beneath the indentation site for 10^5 cycles, together with the microstructure of the same material on an unindented zone. It can be seen that beneath the indentation site, a large amount of microcracking can be found, in comparison with the relative crack-free microstructure. This microcracking is produced by the strong shear stresses generated in that volume during the indentation, which results in a macroscopic inelastic deformation, that is, in quasi-plasticity.

According to the model proposed by Rhee *et al.* [55], it is possible to predict the tendency to brittle or quasiplastic behaviour of a given material, as the ratio of the critical loads for the appearance of the two kinds of damage (P_Y, critical load for quasi-plasticity; P_c, critical load for ring/cone cracking), as:

$$P_Y/P_c = (D/\Gamma)(H/E^*)(H/K_{Ic})^2 R \tag{4.18}$$

where $D = (1.1\pi/3)^3[3(1-\nu^2)/4]^2$, $\Gamma = \Gamma(\nu)$ from [84], K_{Ic} in this case taken as the apparent fracture toughness.

Eq. (4.18) means that, when the ratio P_Y/P_c is high, the damage produced in the

material will be mainly ring and cone cracking, while when the ratio P_Y/P_c is low the predominant damage will be quasi-plasticity. In the case of monolithic and laminated alumina, as it has been shown before (section 2.2.1), both materials present similar values of hardness and elastic properties (E, ν), and, therefore, similar values of the parameters D and Γ; moreover, the indenter size and material used are the same for both materials. The only difference lies in the apparent toughness, which equals to approximately 3.5 MPa$\sqrt{m}$ in the monolithic alumina and 6.0 MPa$\sqrt{m}$ in the laminated composite, due to the presence of σ_r.

This difference in apparent fracture toughness for the two materials implies that the ratio P_Y/P_c for the laminated material is approximately three times smaller than the ratio for monolithic alumina. That means that the A/AZ material has a more pronounced quasi-plastic behaviour than the MA. This behaviour, as said before, is evidenced as extensive microcracking produced in the A/AZ material, generated by the higher shear stresses suffered, because the cone cracking cannot form, due to the higher apparent fracture toughness. This inability to generate cone cracking causes that build-up internal stresses cannot be relieved by the opening of the cone crack and therefore, more microcracking will be generated for the same applied load.

This enhanced microcracking in the A/AZ generates a weakening and loss of strength of the material under the indenter and near the surface, specially if cyclic loading is applied, which results in a faster crack growth. Upon repetitive loading, some of the microcracks coalesce and reach the surface, producing spalling of material. This effect is also enhanced by the fact that the indenter and the indented material are not the same material, so that a certain degree of friction and lateral movement in the contact zone is produced by the mismatch in elastic properties [95]. This lateral displacement will enhance the exfoliation of parts of material. In addition, the compressive residual stress could also enhance the chip-off of surface microcracks in the laminated composite. It is also acknowledged that the laminate may be subjected to larger strains due to the delayed cone cracking, which will, consequently influence the fatigue behaviour.

In Fig. 4.10, the different damage evolution for both MA and A/AZ is presented as a function of depth, after 10^4 cycles at 500 N. During polishing under the conditions described in section 2.4, it is usual that a number of alumina grains are pulled away from the surface [96]. This tearing of grains is enhanced in the case that microcracking exists already in the material, because it weakens the material and the cohesion between grains, as a microcrack can be considered as a gap between materials. In Fig. 4.10 it is seen

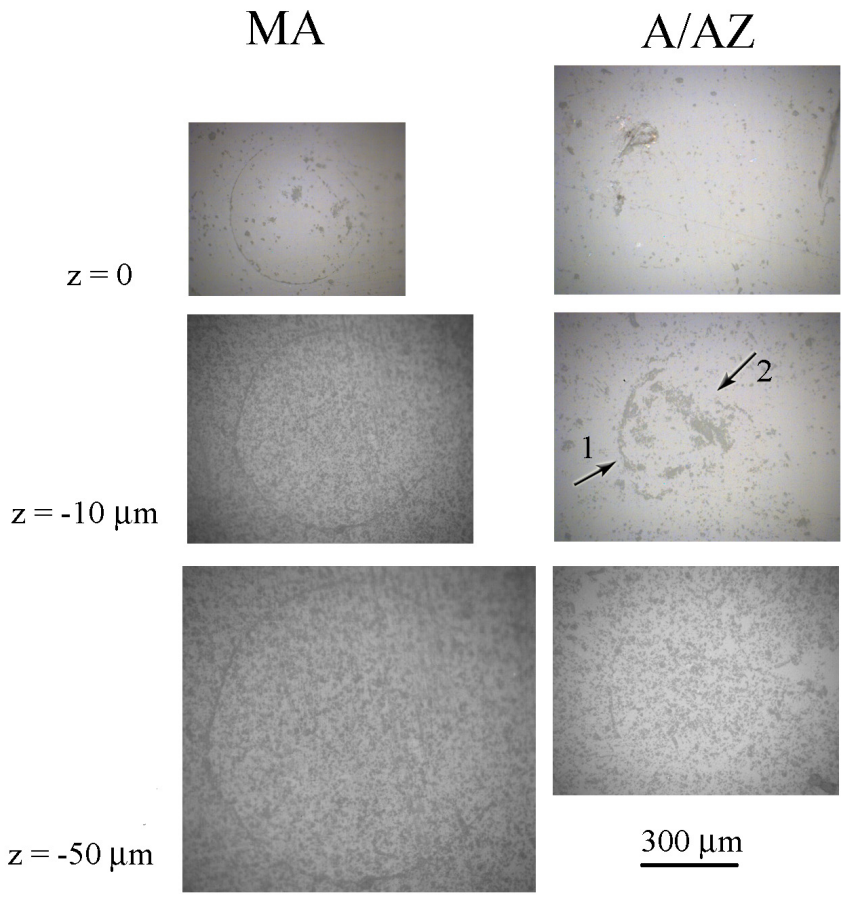

Figure 4.10: Damage present in the MA and A/AZ materials as a function of the depth (z) for an applied load of 500 N and 10^4 cycles. It can be appreciated that in the MA a cone crack is formed, whereas in the A/AZ it exist both ring crack (partially developed into cone crack) and quasi-plastic damaged, as it can be appreciated in z = -10 μm, where the ring crack is marked with (1) and the quasi-plastic damage is marked with (2).

how the MA exhibits a typical cone crack fracture, which is presented as an expanding ring crack feature as the depth is increased. This type of cracking is the expected one for brittle materials. However, in the A/AZ material, the fully developed cone crack it is not observed, and instead, in addition to a ring crack, a highly damaged zone is observed after 10 μm of material removal, which almost disappears after removing 50 μm of material. This region can be identified with the area with microcracks, which produces the quasi-plasticity of the material. In Fig. 4.10 it is also seen that damage is fully localized in the first layer of material, (50 μm, against a total depth of layer of 200 μm), so that the second and subsequent layers of the laminated composite do not appear to have a direct role in the response of the material. After these observations, indeed, we can say that the A/AZ material behaves more quasi-plastically than the MA material, due to the higher apparent fracture toughness.

CHAPTER 5

Cone crack propagation

The study of cone crack propagation was conducted by means of the automatic Finite Element model of crack propagation presented in section 3.5. The objective was to reach a comprehensive insight of the factors involved in the crack geometry definition, starting from simple assumptions of ideally brittle materials, to the complex cases object of this study, in order to deduce general design rules to assist the design of multilayered ceramics.

5.1 *R*-curve

Crack propagation in polycrystalline materials follows the high-energy grain boundaries; for this reason, especially in coarse-grained material, the crack path is tortuous. Friction between adjacent grains on opposite lips of the crack acts as an applied stress, opposing to both opening and sliding forces and increasing progressively the resistance to propagation as the crack becomes longer, up to a value coinciding with a crack length equal to the zone of effective shielding.

5.1.1 Analytical expression of *R*-curve and implementation in the FE model

Several relations for both the bridging stress and the R-curve shape have been formulated, as reviewed recently by Munz [1], depending on the initial assumptions, on the shielding mechanisms and on the type of test and stress distribution. In this work, a

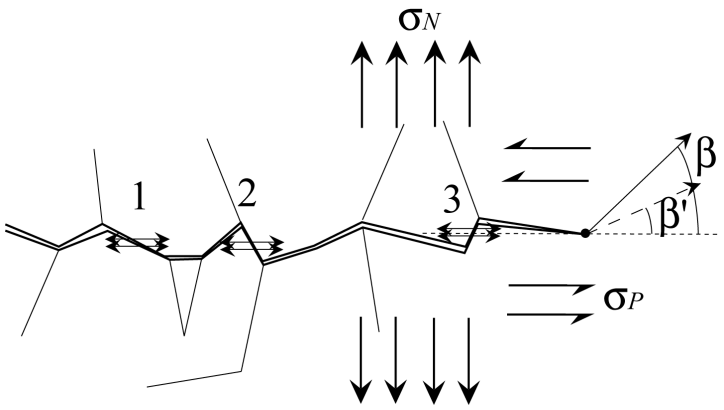

Figure 5.1: Scheme of mode-*II* grain bridging: intergranular friction (points 1,2 and 3) acts against the shear stress σ_P, producing a reduction of the kink angle from β to β'

simple and well-accepted two-parameter empirical relation, proposed by Ramachandran *et al.* originally for toughened alumina and silicon nitride [97] was assumed:

$$K_I^{sh} = K_I^{\infty}\left(1 - \exp\left(-\frac{c}{\lambda}\right)\right) \tag{5.1}$$

with c the crack length, K_I^{∞} a saturation value and λ a normalizing length parameter; the two latter variables are related to the microstructure characteristics, and are obtained in [97] from fitting of experimental data.

In presence of mixed loading, the same bridging mechanisms which resist to the crack opening, act against the shear component of the stress field, which is the cause of the crack deviation β from the straight path. Such deviation is a function of the local K_{II}, that is, the following crack extension takes place in a direction for which such K_{II} disappears. Therefore, a reduction of the shear stress (and, consequently, of the K_{II}) causes a variation of β, as it is schematically represented in Fig. 5.1.

For the following considerations, it will be assumed that resistance both to opening and sliding are provided by the same inter-granular bridges, so that it is reasonable to assume that shielding to shear stress and to opening stress are related, so that the former can be expressed with a similar relation:

$$K_{II}^{sh} = K_{II}^{\infty}\left(1 - \exp\left(-\frac{c}{\lambda}\right)\right) \tag{5.2}$$

The value of the ratio $K_{II}^{\infty}/K_I^{\infty}$ depends mainly on the type of test and can be considered as an index of the weight of the shielding mixity for the given methodology.

Expressions (5.1) and (5.2), superimposed to the un-bridged stress intensity factor, change the crack path; the kinking angle β presented in eq. (3.4) can now be expressed

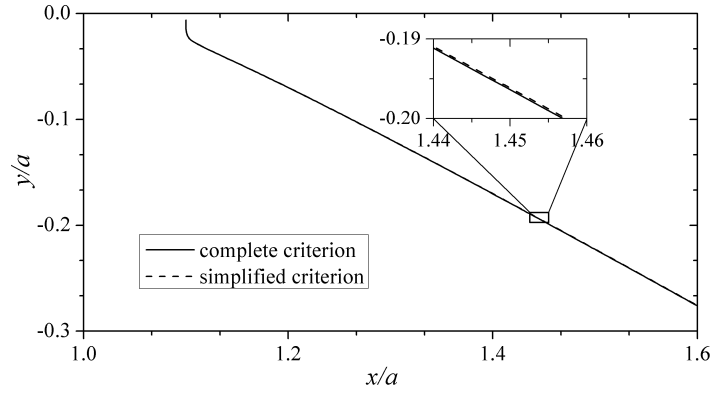

Figure 5.2: Comparison of the crack paths obtained with the kink criterion from Eq. (5.3) and (5.5), respectively, normalized over the contact radius a

as:

$$\beta = -2\frac{K_{II}^i - K_{II}^{sh}}{K_I^i - K_I^{sh}} \tag{5.3}$$

with the upper index i indicating the contribution from the applied indentation load, and the denominator fulfilling the propagation condition (see the scheme in Fig. 3.8), now expressed as

$$K_I^i - K_I^{sh} \geq K_{Ic} \tag{5.4}$$

Eq. (5.3) defines the local kinking of the crack; nevertheless, the crack path is eventually defined by the disappearing K_{II} stress intensity factor; for this reason, if the opening contribution to shielding is neglected from the kinking criterion, the path should be very similar, especially for values of the ratio tending to 0, *i.e.* in the straight portion of the propagation. Such approximation modifies the kinking angle as follows:

$$\beta = -2\frac{K_{II}^i - K_{II}^{sh}}{K_I^i} \tag{5.5}$$

The validity of such simplified expression was verified by direct comparison of the crack paths obtained with the criteria given in Eq. (5.3) and (5.5), respectively, which indeed confirmed that the paths are almost overlapping, as shown in Fig. 5.2.

From the computational point of view, the paths obtained with the definition of β given in Eq. (5.3) are affected by numerical oscillations, which are due to the fact that the lower-term of the ratio is formed by a growing contribution (K_I^{sh}) and a decreasing one (K_I^i). For this reason, small angle oscillations were observed, which in some case lead

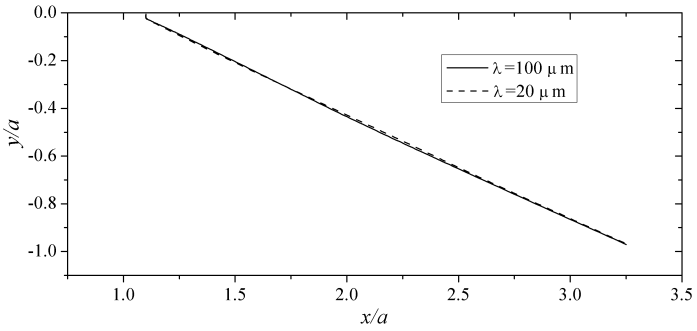

Figure 5.3: Influence of the microstructural coefficient λ on the crack path, for arbitrary values of the remaining variables. It can be seen that such coefficient is irrelevant in the path definition.

to instability in the propagation. Conversely, Eq. (5.5) guarantees the same accuracy of the crack path with higher numerical stability, and was used thereafter as the kinking angle formulation.

Determination of the parameters K_I^∞ and K_{II}^∞ involved in Eqs. (5.1) and (5.2) was performed by an iterative fitting of the result output, crack angle and length, to experimental data, whose scatter was used for deriving a correspondent scatter in the shielding evaluation.

The third coefficient, λ, is related to microstructural variables, toughness and elasticity of the material. The approach followed in this work is focused on the final effect of the shielding on the crack trajectory, which is not affected by the local value along the transition portion (*i.e.* for $K_I^{sh} \ll K_I^\infty$). The influence of λ was hence studied by varying arbitrarily the value, from 20 to 150 μm, for a given set of the remaining parameters. The crack path was found to be not significantly influenced by λ, as shown in Fig. 5.3, therefore a constant value λ=100 μm, in agreement with the experimental results on similar materials in Ref. [97], was assumed.

5.1.2 Results

Experimental measurements of crack length and angles for A03 and A05 materials are reported on table 5.1, together with the relevant magnitudes computed with the FE model; observation of crack geometries in both materials showed that, despite the high experimental scatter, the crack angle in both materials is almost constant throughout the propagation, and is wider in the material with the coarsest microstructure, while the

Table 5.1: Experimental results and corresponding R-curve parameters obtained for alumina with different grain size tested with a 2.5 mm radius sphere under the indentation load P=4000 N. As a comparison, results obtained from simulation for non-shielding alumina (labelled as NS), which are in agreement with previous works [38], are also reported.

	grain size	$\alpha[^\circ]$	c/a	$K_I^\infty\,[MPa\sqrt{m}]$	$K_{II}^\infty\,[MPa\sqrt{m}]$
NS	–	18.5	2.8	–	–
*A*03	2.6±1.6	26.8 ± 1.1	1.7 ± 0.4	2.5 ± 1.0	2.3 ± 0.7
*A*05	3.8±2.3	27.4 ± 2.2	1.8 ± 0.3	2.25 ± 0.75	2.5 ± 1.0

crack length is reduced, as it was expected, corresponding to a larger mode-I shielding effect. For the longest sintering time, 12 hours, the microstructure obtained proved to be too coarse for the formation of cone crack, which was inhibited by quasi-plastic deformation, associated with subsurface microcracking [49].

Observation of the crack paths obtained from the simulations confirmed that, after the initial transition from ring to cone, the angle of propagation is constant along the length for long-enough cracks (approx. $c/a > 0.5$), with only a slight progressive increase until the saturation value of the shielding is reached. However, as observed above and shown in Fig. 5.3, the length necessary to reach such steady shielding, in other words the value of the coefficient λ, has a negligible influence on the crack trajectory.

Considering the transition from unstable to stable propagation, it is worth noting that the denominator in either of eqs. (5.3) or (5.5) undergoes a discontinuity, because the indentation contribution K_I^i passes from a decreasing trend (point D in Fig. 3.13) to a constant value, associated to the load increments necessary to produce crack propagation. This could lead to expect a crack kink; however, in agreement with the above-mentioned remark that K_I is not relevant for defining the $K_{II} = 0$ direction, such kink is almost imperceptible in any of the calculated paths, as it is confirmed by experimental observations. Nevertheless, in order to consider both portions of propagation, allowing thus a more realistic comparison with experimental values, it was decided to measure the angles from graphic representations of the crack paths rather than directly from the output of the simulations, obtaining thus an average value, more representative than the local value at the crack tip.

Results were employed in the fitting procedure for determination of the parameters involved in defining the R-curve: from the value of final crack length under the given load, the parameter K_I^∞, *i.e.* the value of the opening shielding, was first deducted

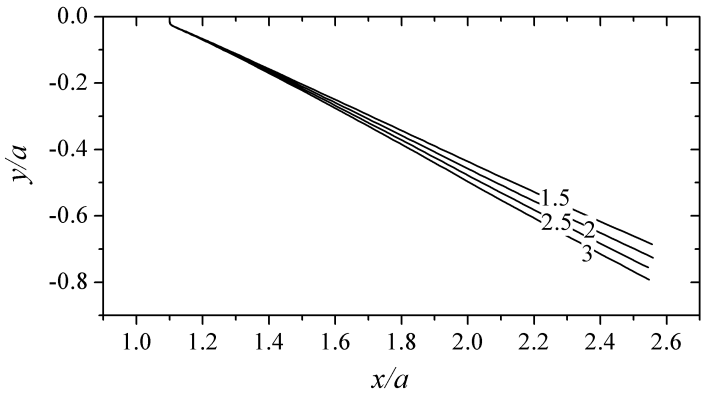

Figure 5.4: Crack paths obtained by varying the coefficient K_{II}^{∞} (expressed in $MPa\sqrt{m}$) for a constant $K_I^{\infty} = 2.0 \quad MPa\sqrt{m}$. Each path presents a constant angle, meaning that the discontinuity in the lower term of eq. (5.5) does not affect the crack trajectory

iteratively from the variation in final crack length; successively the shear parameter K_{II}^{∞} was varied, and the fitting value was obtained from convergence of the propagation angle to the experimental value. It was important to follow this order, because both the opening and the shearing shielding contribute to determine the angle of propagation α. As an example, the crack paths obtained in alumina for a constant mode-I shielding, by varying the mode-II contribution are shown in Fig. 5.4.

The influence of both the opening and shearing shielding factors on the crack angle can be visualized in Fig. 5.5, where the angles obtained are plotted as functions of the mode-II shielding coefficient, for various values of K_I^{∞}, each one corresponding to a different crack length. From such plot the range of parameters corresponding to several crack geometries can be easily deducted.

The results obtained are summarized in table 5.1, together with a comparison with the values expected (calculated) for an elastic material with the same elastic properties and toughness of alumina but without taking into account any shielding, in other words an ideally brittle alumina, whose angle is in agreement with the prediction from the works of Kocer [39] and Fett *et al.* [40]. The difference in terms of both crack length and angle is noteworthy, and corresponds to values of shielding that are not negligible, as they are of the same order of magnitude as the toughness of the material; such high values were not expected, because the fine microstructure would suggest a smaller amount of bridging. They are attributed to the highly inhomogeneous stress field and to the small crack opening under spherical indentation, which implies that the grains

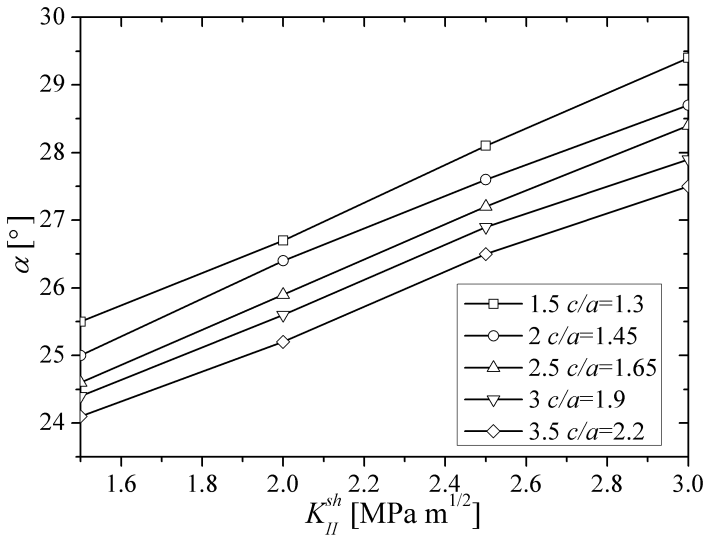

Figure 5.5: Cone crack angles as function of K_{II}^{∞}, for various values of K_I^{∞} (expressed in $MPa\sqrt{m}$) corresponding to different crack lengths

friction and interlocking are favoured.

The value of the ratio $K_{II}^{\infty}/K_I^{\infty}$, close to the unity, gives information on the nature of the bridging stress acting on the crack, meaning that under Hertzian indentation the shearing component of such stress is similar to the opening contribution. This, on the other hand, is intuitively understandable, since the interlocking between grains on opposing crack lips (see Fig. 5.1) is likely to act against sliding as much as against opening, or even more in an inhomogeneous stress field.

In addition to the results presented so far, simulations of cone crack propagation in silicon nitride with or without elongated grains were performed. Experimental results by Belmonte *et al.* [98] were reproduced with indentation and materials conditions (contact radius $a \approx 200\,\mu m$, load $P = 2000\,N$, toughness $K_{Ic} = 5.2\,MPa\sqrt{m}$) taken from the same work or from other reference [97]. The shielding was assumed higher in the long-grained material, consistently with the apparent toughness from Ref. [98] (7.4 and 8.1 $MPa\sqrt{m}$, respectively); such effect can be seen in the variation of the crack angles, as measured from the micrographs presented in the cited reference, corresponding to approx. 25° and 31° respectively.

In the simulations, the values of toughness were translated into the shielding parameters $K_I^{\infty} = K_{II}^{\infty} = 2.2\,MPa\sqrt{m}$ in homogeneous and $K_I^{\infty} = K_{II}^{\infty} = 5.0\,MPa\sqrt{m}$ in textured materials, respectively. The resulting angles were compared with the experi-

mental ones. The agreement was found to be good, especially in the case of the former material, for which $\alpha = 25.2°$, while in the long-grained material a slight difference is present ($\alpha = 28.8°$). This can be attributed to an underestimation of the shielding, depending on the technique employed for the toughness measurement, or to the presence of inelastic damage, enhanced by the microstructure itself [97], which affects the stress field and, therefore, the crack path.

5.2 Residual stresses

Residual stress in the first layer was included in the simulations as a constant pressure acting on the border. Although such representation does not consider the relaxation of the stress at the edge, it describes well the central region of the samples; if simulations are compared with indentations performed far enough from the edge, as mentioned above (section 2.3), the approximation is considered acceptable.

The influence of such stress distribution on the stress intensity factors (and, therefore, on the crack path) is included in the output given by the software, which is calculated from the stress field at the crack tip; the kinking angle definition, therefore, is formally just the same as in Eq. (3.4). However, in order to evaluate intuitively which effect can be expected, an approximation of such contribution can be seen as that of a slanted crack in a semi-infinite plate (shown in Fig. 5.6):

$$K_I^r = Y\sigma_r\sqrt{c}\sin^2\alpha \tag{5.6}$$

$$K_{II}^r = Y\sigma_r\sqrt{c}\sin\alpha\cos\alpha \tag{5.7}$$

with Y a geometry factor. A more correct formulation should include the mixed terms (*i.e.* the normal stress-deriving K_{II} and the shear stress-deriving K_I), but since such terms are in general modest, and Eqs. (5.6) and (5.7) are only illustrative, they were neglected for the sake of clarity.

Since α has not a constant value, an analytical calculation of K_I^r and K_{II}^r would be unviable. For this reason Finite Element analysis is needed for evaluating cone crack on stressed materials.

The K_I evolution is similar to the one presented above (Fig. 3.13), reduced of a quantity which increases as the crack advances, as shown schematically in Fig. 5.7. The propagation direction is defined, again, as the direction of the disappearing K_{II}; in other

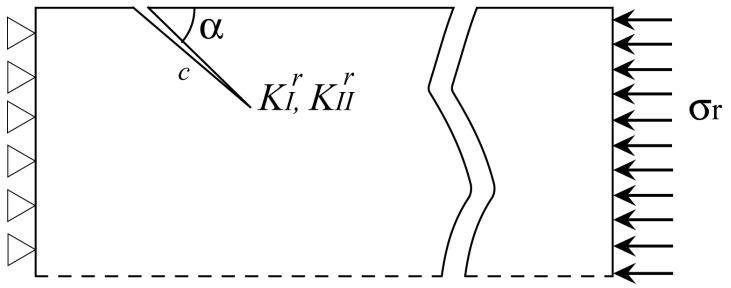

Figure 5.6: Scheme of slanted crack on a semi-infinite plate, whose stress intensity factors approximate the effect of residual stress on the Hertzian cone crack.

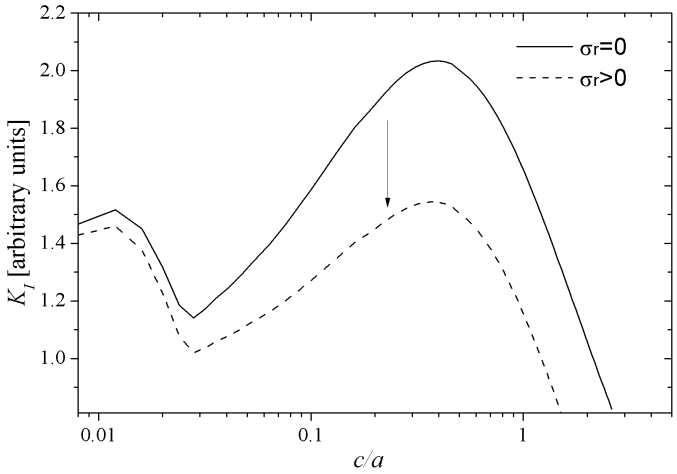

Figure 5.7: Scheme of the influence of the residual stresses on the unstable mode-I stress intensity factor

words the one for which

$$K_{II}^i + K_{II}^r = 0 \tag{5.8}$$

The left-hand side of the relation is composed by a decreasing (from indentation) and an increasing (from residual stresses) terms, therefore the relative weight of the latter grows as the crack propagates. The crack angle, therefore, changes progressively.

It can be seen that many parameters are involved in the determination of $K_{I,II}^{i,r}$ and, therefore, of the crack path: the Poisson ratio ν, the indentation load P, the residual stress σ_r, the fracture toughness K_{Ic}, microstructural effects, such as grain bridging. In order to simplify the problem and isolate the contribution of each parameter, it was decided to focus first on the effect of the residual stress σ_r, and to include successively

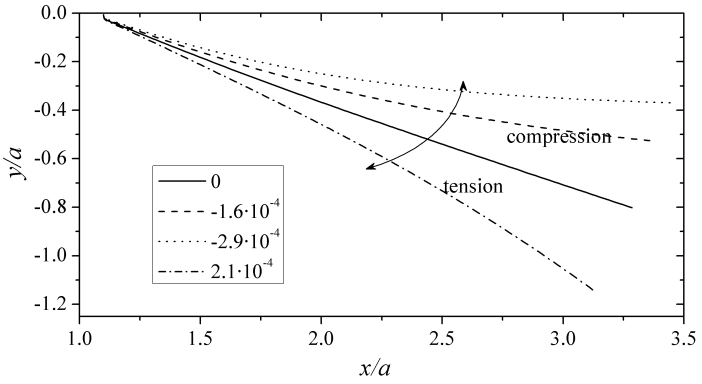

Figure 5.8: Crack paths in alumina as functions of the normalized residual stresses parameter σ_r/p_0

the shielding effects, which were determined in the monolithic reference material, and load increments when the condition

$$K_I > K_{Ic} \tag{5.9}$$

is not fulfilled, allowing thus to simulate both stable and unstable segments, and providing hence a more realistic representation of actual experiments and a correct comparison.

5.2.1 Influence of the residual stresses on the unstable propagation

In a first step, only unstable propagation was considered, in other words no check on the toughness was performed (see flow diagram of the algorithm, fig. 3.8); instead, the penetration depth was kept constant, and so was, consequently, the indentation load. The graph paths obtained from the simulation of indentation of alumina, neglecting any microstructural shielding effect and varying the value of the residual stress σ_r are shown in Fig. 5.8. The same indentation depth h was applied to all cases, although it must be considered that when residual stresses are present, the corresponding indentation load is modified by the additional constraint provided by the residual stress itself.

It can be seen that without residual stresses the angle stabilizes shortly to a constant value, while, if stresses, either compressive or tensile, are present, the angle decreases or increases progressively, respectively.

The amount of variation with respect to the unstressed case depends mainly on the value of the σ_r/p_0 ratio, with p_0 the mean contact pressure, as can be inferred considering

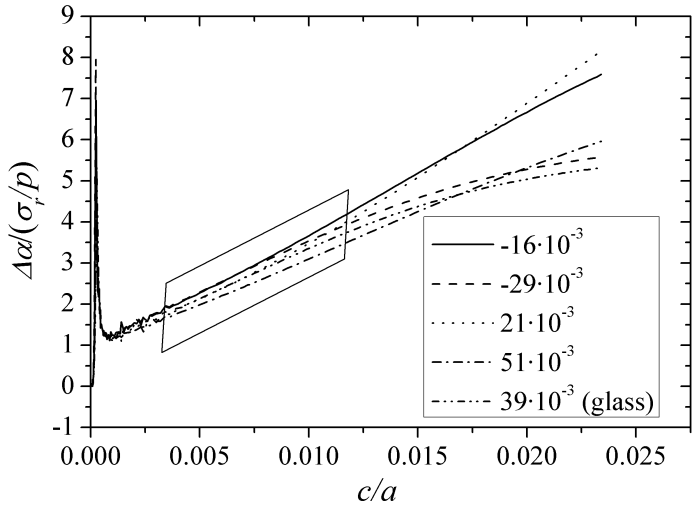

Figure 5.9: Normalized angle variation, with respect to the unstressed counterpart, of alumina with various amounts of residual stress and of soda-lime glass. The zone of linearity is highlighted

the dependencies given by the approximated analytical formulations of Eqs. (3.7) (with $K_I \propto P$) and (5.6) ($K_I \propto \sigma_r$).

To confirm such dependency, the normalized curves fall within a common band (Fig. 5.9), following approximately a linear relationship with the parameter σ_r/p_0:

$$\Delta\alpha \propto \frac{\sigma_r}{p} c \tag{5.10}$$

The linear behavior is lost in the first portion, during the transition from ring to cone crack, and in the last, where the angle tends asymptotically either towards $\alpha = 0$ (compressive stresses), or $\alpha = 90°$ (tensile stresses).

Calculations for alumina with different residual stresses and for stressed soda-lime glass ($E = 72.3\,GPa$, $\nu = 0.21$, $\sigma_r = 100\,MPa$) are presented in the same graph. Curves from all the cases are comprised into the same linear distribution, meaning that the relation has general validity, and that the main factor for determining the angle variation is the value of the σ_r/p_0 ratio.

5.2.2 Influence of the residual stresses on the stable propagation

In order to represent correctly the crack growth, the fulfilling of the condition $K_I > K_{Ic}$ was imposed for crack propagation on laminated materials (still neglecting any shielding

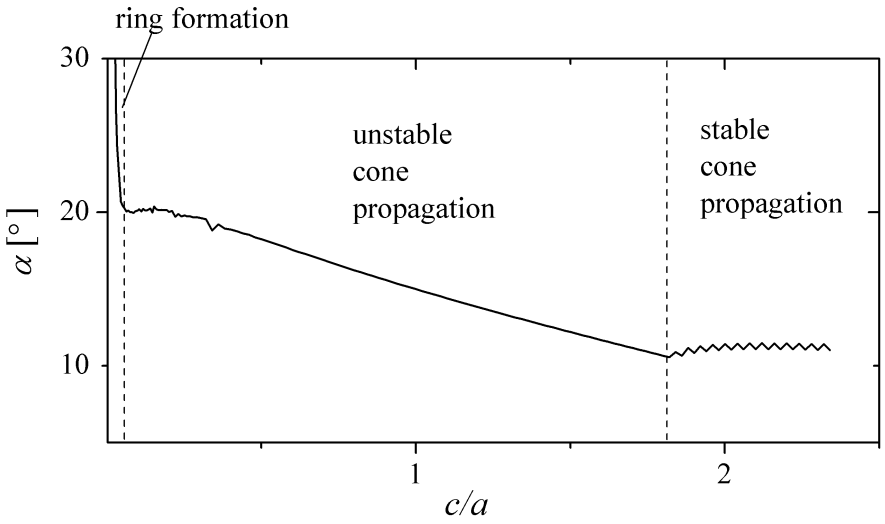

Figure 5.10: Cone crack angle in presence of residual stress, presenting a progressive decrease during unstable propagation and a constant value when stability is attained

effect). The crack growth is strongly modified: the linear behaviour presented in Fig. 5.9 is fulfilled on the unstable portion of the propagation, but when the point D of the curve in Fig. 3.13 is reached, the equation of the kink angle becomes:

$$\beta = -2\frac{K_{II}^i + K_{II}^r}{K_{Ic}} \tag{5.11}$$

with i and r indicating indentation and residual stress contributions, respectively. On the upper side, K_{II}^i increases as the crack propagates, as a consequence of load P increment; K_{II}^r increases as well, following Eq. (5.7), so that equilibrium is achieved, and the angle from here on is almost constant. Such effect is illustrated in the form of angle as a function of crack length in Fig. 5.10.

5.3 Ceramic laminates

The relations obtained in the previous sections, including bridging effects, were included in the simulations, in order to obtain a representation as realistic as possible of the ceramic laminates object of the study. For the crack shielding evaluation, it was assumed that the presence of bridging modifies the crack path to the same extent in monolithic MA and in A/AZ and A/2AZ laminates, because it depends only on the microstructure, which is very similar in the three materials. Therefore, the same values are assumed

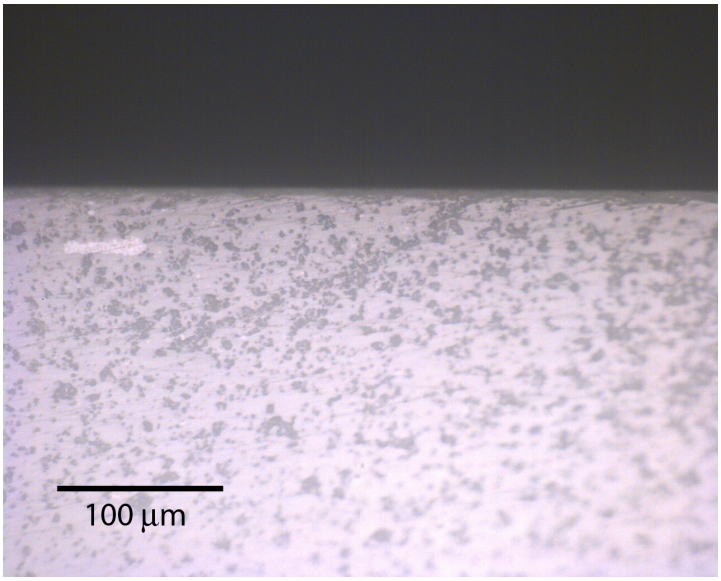

Figure 5.11: Micrograph of cone crack produced by Hertzian indentation ($P = 980\,N$, $\phi = 2.5\,mm$) on laminated material ($\sigma_r \approx -200\,MPa$)

Table 5.2: Experimental (lower index *exp*) and simulation (FE) results for A/AZ and A/2AZ laminates and monolithic MA, as reference material, obtained from indentations with a 1.25 mm radius sphere under the load P=980 N. The common value of $K_I^\infty = K_{II}^\infty = 2.0\,MPa\sqrt{m}$ was included in all the calculations for representing the R-curve.

	$\alpha_{exp}[^\circ]$	$\alpha_{FE}[^\circ]$	c/a_{exp}	c/a_{FE}
MA	26.9 ± 3.1	26.0	1.9 ± 0.2	2.0
A/AZ	20.4 ± 1.6	21.3	1.6 ± 0.2	1.6
$A/2AZ$	18.1 ± 4.0	20.2	1.2 ± 0.5	1.4

for all materials, and they are calculated for MA with the method presented in section 5.1.2, yielding the values $K_I^\infty = K_{II}^\infty = 2.0MPa\sqrt{m}$.

Compressive stress during unstable propagation produces a progressive reduction in angle, because its contribution to K_{II} grows as the crack grows. On the other hand, grain bridging has the opposite effect, which is to say that the angle increases slightly until saturation is reached, so that, depending on the involved parameters, the crack path can present some variation or oscillation in angle, and the global effect is a quite straight path, as it is confirmed by the experimental observations, such as the crack shown in Fig. 5.11.

The crack paths for the specific cases of A/AZ and A/2AZ laminates are presented in Fig. 5.12; comparison with the monolithic reference gives a difference in crack angle,

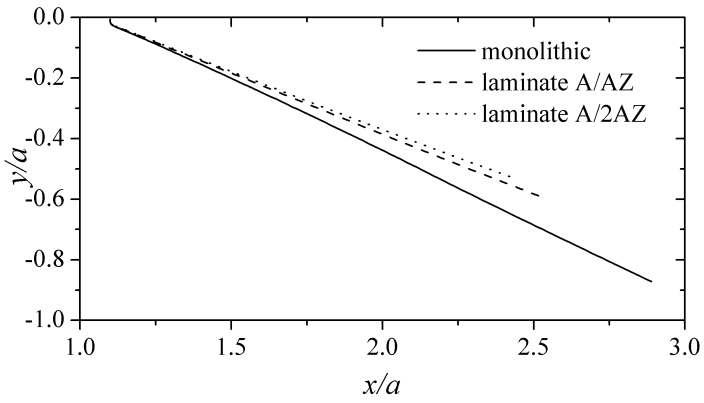

Figure 5.12: Crack path obtained for MA, A/AZ and A/2AZ materials, considering the effect of crack shielding and residual stress on the crack propagation

which is in both cases narrower than in the monolithic, and almost constant, as observed above, and in final crack length, which is shorter. The numerical values of both geometry parameters are confirmed by experimental observations, as presented in table 5.2.

It is worth noting that despite the complexity and inter-relation of several phenomena, the study allowed to isolate the contribution from any of the features involved, by superposition of simple analytical relations or stress fields to Finite Element simulations, and to combine them again in the analysis of complex materials. The prediction of the overall effect is consistent with experimental observations, and the effectiveness of the model was also confirmed by comparison with data from literature.

CHAPTER 6

Strength degradation by cone cracking

The geometry of the cone crack, analyzed in deep in the previous chapter, has a profound influence on the strength of the sample/component, because the presence of such type of crack *in service* can act as the fracture starting defect under remote loading. For this reason, although the issue of strength of ceramics goes beyond the main scope of this thesis, the subject was given some insight, in order to point out the relevance of contact resistance within an overall evaluation of the material mechanical properties.

The assessment of the strength degradation is usually conducted by comparing the flexural strength of indented samples with that of unindented materials. In the case of laminated materials, the strength degradation must be compared with that of monolithic materials in order to interpret correctly the results; however such comparison is complex, because several phenomena are involved in determining the difference of fracture resistance between monolithic and laminated material, such as:

- Inhomogeneous elastic properties
- Residual stresses
- Cone crack geometry

In order to obtain a thorough evaluation of the specific case, and to derive general conclusions, valid for any ceramic laminated structure, the above-mentioned issues were

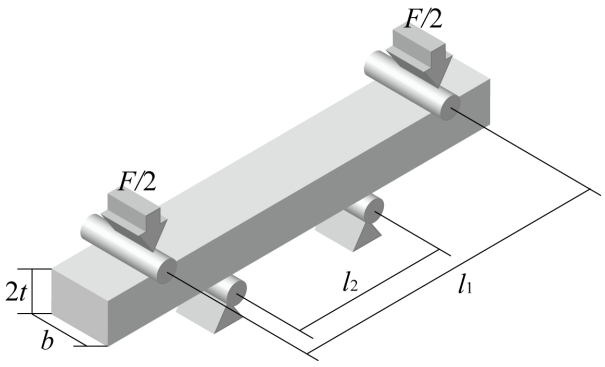

Figure 6.1: Scheme of transversal flexural testing

studied individually from the analytical point of view and consistency was sought by taking an approach combines aimed experiments (described in section 2.5) and two-steps simulation of the same case of study (section 3.3).

6.1 Flexural strength of laminated materials

The first point, the elastic mismatch, influences the distribution among the layers of the stress field generated by bending test. Considering the component parallel to the sample length, the expression of such distribution in an homogeneous material is:

$$\sigma = \frac{3F(l_1 - l_2)}{2b(2t)^3}y \tag{6.1}$$

with the symbols as in Fig. 6.1. Fracture is assumed to start at the surface ($y = t$, where the bending stress is higher. From eq. (6.1), the critical value is:

$$\sigma^* = \frac{3F(l_1 - l_2)}{4b(2t)^2} \tag{6.2}$$

Application of (6.2) to the case of multilayers yield an equivalent stress (σ_{eq}) rather than an actual value *i.e.* the maximum stress that would exist if the material was elastically homogeneous:

$$\sigma^*_{eq} = \frac{3F(l_1 - l_2)}{2b(2t)^2}t \tag{6.3}$$

Following Cai *et al.* [99], the flexural rigidity of a (2n+1)-multilayered composite can be expressed as:

$$(EI)^* = \frac{1}{3}\sum_{i=1}^{n} E_i b(t_i^3 - t_{i-1}^3) \tag{6.4}$$

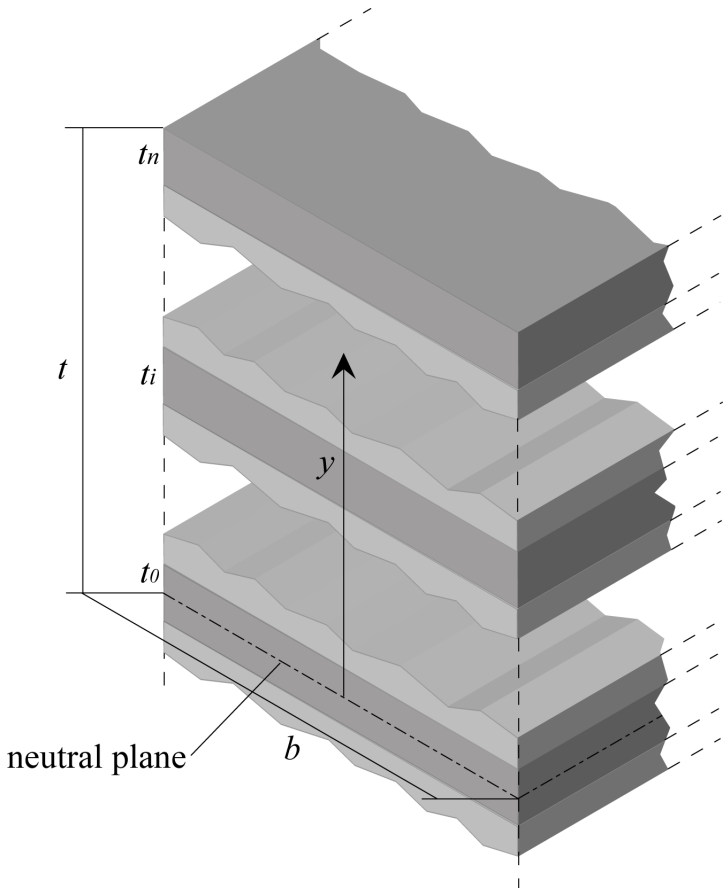

Figure 6.2: Notation for the rigidity and stress calculation of a multilayer subjected to flexion

with $\sum^n t_i = 2t$.

Therefore, the bending stress at a distance y from the neutral axis, with y contained within a layer with Young's modulus E_i is given by:

$$\sigma(y) = \frac{3F(l_1 - l_2)y}{4(EI)^*} E_i \tag{6.5}$$

Eq. (6.5) means that the stiffer material bear a higher part of the load, *i.e.* act as a "shield" of the stress from the other, more compliant, material.

Such effect is shown in Fig. 6.3 for both the A/AZ and A/2AZ materials; the stress distribution is compared with the solution of Eq. (6.1). In both cases the stiffer alumina layers bear a higher portion of the load, so that the stress at the surface is higher than the equivalent stress. A scaling coefficient can be defined, based on the ratio between the stiffness of the alumina layer and the composite flexural rigidity of the multilayer,

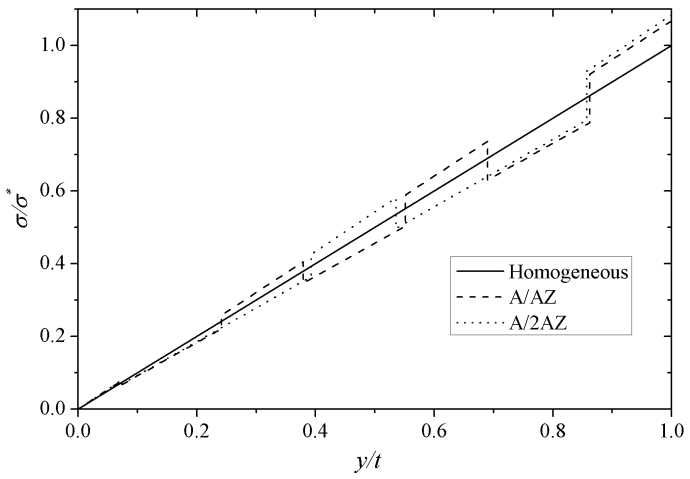

Figure 6.3: Normalized stress distribution on laminated A/AZ and A/2AZ, compared with an homogeneous material. σ^*_{eq} is the surface value, defined in eq. (6.2)

by combining eqs. (6.4) and (6.1):

$$\xi = \frac{btE_{Al_2O_3}}{2(EI)^*} \tag{6.6}$$

so that the actual critical stress for the laminates will be

$$\sigma^* = \xi\sigma^*_{eq} \tag{6.7}$$

with $\xi_{A/AZ} = 1.07$ and $\xi_{A/2AZ} = 1.08$, for the laminates object of this study.

On the other hand, the presence of compressive residual stress acts in the opposite way, so that the actual stress in ceramic laminates can be calculated as:

$$\sigma^* = \xi\sigma^*_{eq} - \sigma_r \tag{6.8}$$

A consequence of Eq. (6.8) is that the beneficial effect of improved surface resistance provided by compressive residual stress is hampered, to a certain extent, by the stress redistribution, because the surface layer assumes the greatest part of the load. In the limit case of

$$(\xi - 1)\sigma^*_{lam} > \sigma_r \tag{6.9}$$

fracture would occur at a lower load (or, which is the same, equivalent stress) in the multilayer than in the monolithic material, as shown schematically in Fig. 6.4. Such

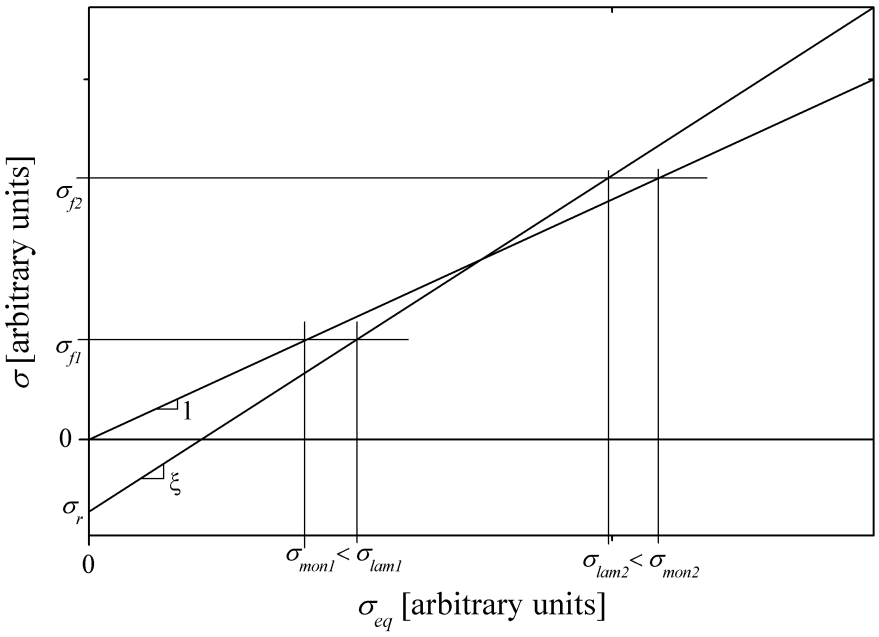

Figure 6.4: Actual surface stress against equivalent stress in monolithic and laminated material. If the fracture stress is at the right hand of the crossing point, the laminate is weaker than the monolithic material.

event is not likely to happen in the ranges of elastic mismatch, residual stresses and fracture stresses of advanced materials, nevertheless it should taken into account in the design of advanced ceramics.

It should be noted that stress redistribution does not affect the resistance to surface-focused loading types, such as contact loading, as it has been shown in section 4.1. This confirms that laminated geometries are most effective in applications in which the ceramic components are subjected to localized blunt loading, rather than to remote loading.

The results of the bending tests on unindented MA and A/AZ materials are shown in Fig. 6.5. The relation between the strength of both materials fulfils, with good agreement, Eq. (6.8): the improvement in equivalent strength is equal to the amount of residual stress, minus the effect of the stress redistribution, quantifiable in approx. the 10% of the strength.

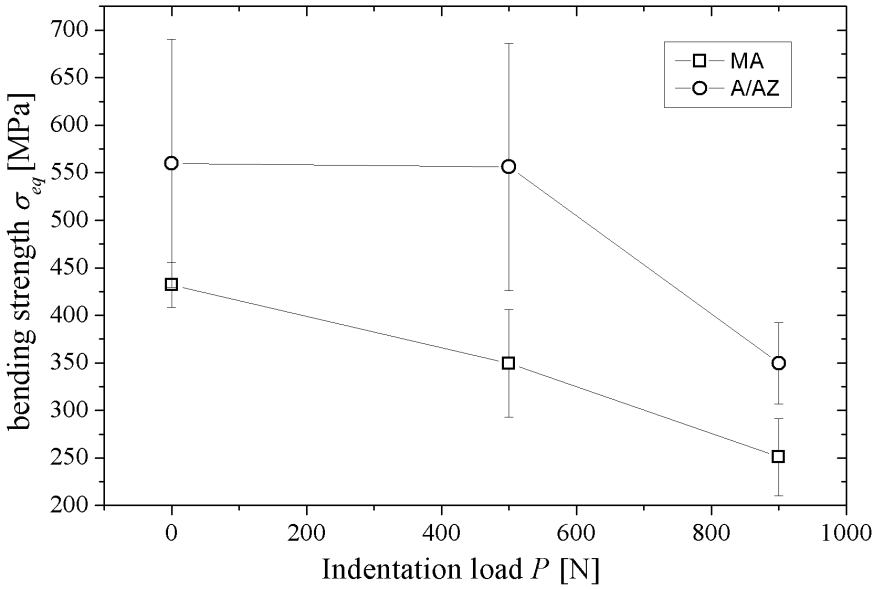

Figure 6.5: Experimental strength degradation as a function of the indentation load of monolithic alumina (MA) and multilayered material (A/AZ)

6.2 Strength degradation

In post-indentation strength, another factor must be considered: the geometry of the cone crack is influenced by the presence and amount of residual stress, and this reflects on the bending test.

Experimental results show that MA and A/AZ present different trends of strength degradation: in the former the drop in strength is immediate and almost linear with the indentation load, while the latter presents a sort of "threshold effect", meaning that the damage produced by relatively low load does not generate critical damage, compared with the previously existing defects.

In the high-load case, on the other hand, well-developed cracks exist, so that such case can be represented as an ideal fracture mechanics problem, and as such it was addressed on a two-steps Finite Element model, with the limitations discussed in section 3.3. From the analytical point of view, if the cone crack is long enough, the inert strength is, on a first approximation, proportional to the classical Griffith relation [45]:

$$\sigma^* \propto \frac{K_{Ic}}{\psi(\alpha)c^{1/2}} \tag{6.10}$$

Therefore both parameters of the cone crack geometry, the length c and the angle α

Table 6.1: Cone crack geometry for MA and A/AZ, respectively, as calculated by iterative Finite Element simulation

	MA	A/AZ
α	18.5	21
c/a	1.5	0.85

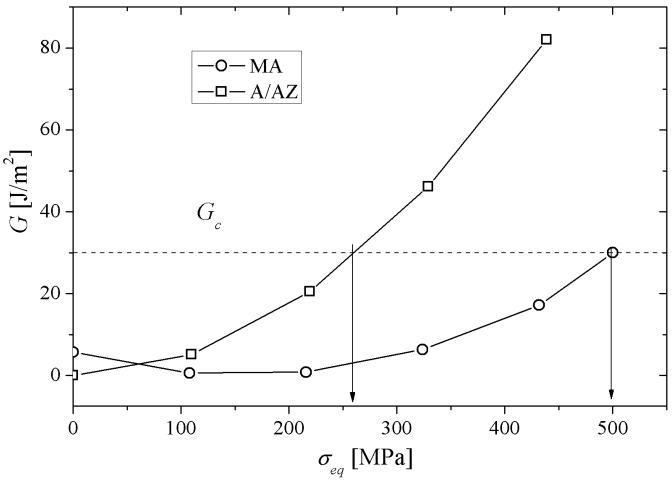

Figure 6.6: Fracture energy at the tip of the cone crack on MA and A/AZ as a function of the equivalent stress from eq. 6.3

(this latter included in the ψ coefficient) take part in the strength definition, and can be included in an unique geometry coefficient:

$$Y = Y(\alpha, c, P) \tag{6.11}$$

whose ratio for laminated and monolithic materials, Y_{lam}/Y_{mon}, is a measure of of the improvement obtained from the crack geometry difference in the two configurations.

As already mentioned, the cracks corresponding to the high-load conditions were calculated iteratively for monolithic alumina and A/AZ on a two-dimensional axisymmetrical model, then translated to a cone crack on a three-dimensional beam (one quarter of a beam, to reduce the calculation time), which was subjected to four-point bending. The cracks thus obtained are reported in table 6.1: the slight difference with respect to the values presented in the previous section derive from the different approximations assumed in this case and the loading conditions, also somewhat different.

The results of the bending simulations are shown in Fig. 6.6: because under bending the stress state at the tip of the "slanted" cone crack is mixed, the fracture criterion applied was based on the fracture energy G rather than on the stress intensity factors.

The critical value was deduced from the particular mode-I case:

$$G_c = \frac{K_{Ic}^2}{E} \tag{6.12}$$

and was calculated as a function of the bending load.

From the fracture energy curves, two differences can be seen in the energy evolution in laminates and monolithic alumina:

1. Residual stresses in the laminated material provoke a shift of the G parabola to positive values of σ_{eq}, in other words the applied stress must overcome the residual stress before producing a positive stress intensity factor;

2. The effect of the different cone crack geometry is a change in the growth rate of the fracture energy, in geometrical terms in the $G(P)$ parabola concavity.

Both factors contribute positively to the strength of laminates with residual stresses, provided that the cone crack is small enough compared to the layer thickness.

From such considerations an analytical estimation of the equivalent indentation strength of a generic ceramic laminate, compared with its monolithic counterpart, can be extracted by combining eqs. (6.8) and (6.11), including

1. The comparison of the crack geometries (ratio Y_{lam}/Y_{mon}),

2. The stress redistribution (coefficient ξ),

3. The presence of residual stresses (value of σ_r).

Such relation is expressed as:

$$\sigma_{lam}^* = \frac{Y_{lam}}{Y_{mon}} \frac{\sigma_{mon}^*}{\xi} + \sigma_r \tag{6.13}$$

From eq. (6.13), an estimation *a priori* of the improvement obtained by any laminated structure can be obtained: the values of σ_r and ξ can be obtained easily from geometrical considerations, while the variation in the cone crack geometry is more complex, as it was shown in chapter 5, because it depends on many aspects, such as indentation load, fracture toughness, microstructure-derived R-curve, indenter size.

All the factors mentioned were included intrinsically in the FE simulation, from where the critical (equivalent) stress was extracted (as presented graphically in Fig. 6.6), yielding values in very good agreement in the case of MA and within the experimental error for A/AZ.

CHAPTER 7

Contact strength of ceramic laminates

The primary philosophy of this research is the characterization of the mechanical response to surface-focused loading of ceramic laminates with residual stresses, especially to blunt contact, obtaining thus an evaluation of the performances in actual *in service* conditions. For this, two approaches have been followed in the previous sections for defining the critical study parameters: the damage prevention (in chapter 4) and the damage tolerance (chapter 5 and 6). Despite of the differences in those approaches, in both cases the entire damage was purposely contained within the first, compressive, layer, consistently with the established research scope.

Nevertheless, the possibility that blunt contact, in its ultimate consequence, cause failure of the sample can not be disregarded, and deserves some characterization, especially in light of the differences the so-defined "contact strength testing" presents if compared with traditional remote-loading testing methods, and of the modifications laminated structures can provide against such type of loading.

7.1 Experimental results

The contact strength tests were performed with the procedure explained in section 2.6: MA and A/AZ bars were subjected to compression by opposite cylinders and the fracture equivalent stress was recorded. A scheme of the experimental setup is reported again for sake of clarity

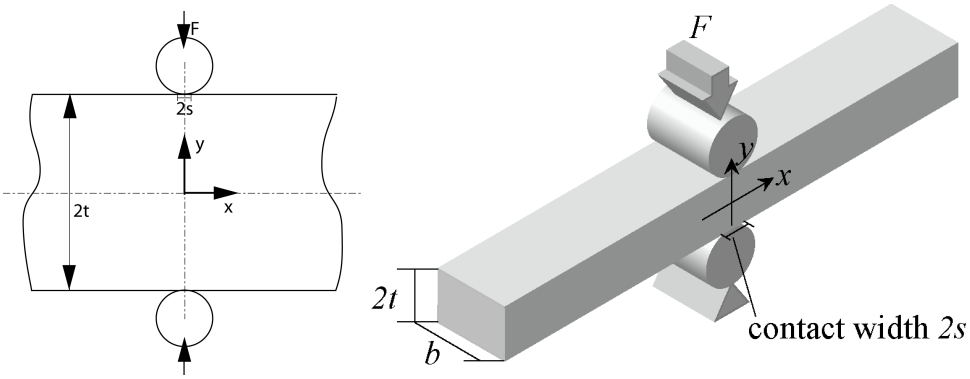

Figure 7.1: 2D and 3D Schemes of the contact strength testing

Experimental results of contact strength tests for monolithic and laminated materials, respectively, are reported in Fig. 7.2, both as calculated from Eq. 7.1:

$$\sigma_x^{max} = Y\sigma_{eq} = Y\frac{F}{tb} \tag{7.1}$$

with both $Y = 0.490$, as in the classical solution, and $Y = Y(\sigma_e q)$, *i.e.* with the Finite Element correction function which will be discussed below (section 7.2).

Although the number of pure alumina samples tested is not high enough for a proper statistical analysis of the former material, the Weibull exponent m (11, with the 90% confidence interval [4.0; 16.1]) calculated by the "Maximum Likelihood Procedure" confirmed previously reported values [69], and the strength (625 MPa [563; 703] and 579 MPa [524;648] from numerical and FE expression, respectively) is in agreement with values for fine-grained alumina.

The numerical and FE values do not differ significantly, being the dispersion within the experimental error; it is thought, therefore, that the simpler approach can be considered valid, as long as no major accuracy is needed. The strength of the laminate was found of 840 MPa [781; 904] and 794 MPa [744; 849] from numerical and FE expression, respectively.

The values measured in this case relate to an effective strength of the structure, rather than to intrinsic strength of the material. Consistently, the improvement respect to monolithic material coincides with the amount of residual stresses, as confirmed by FE analysis. The micrograph in Fig. 7.3 shows that fracture started from the surface, and this was true for all cases examined.

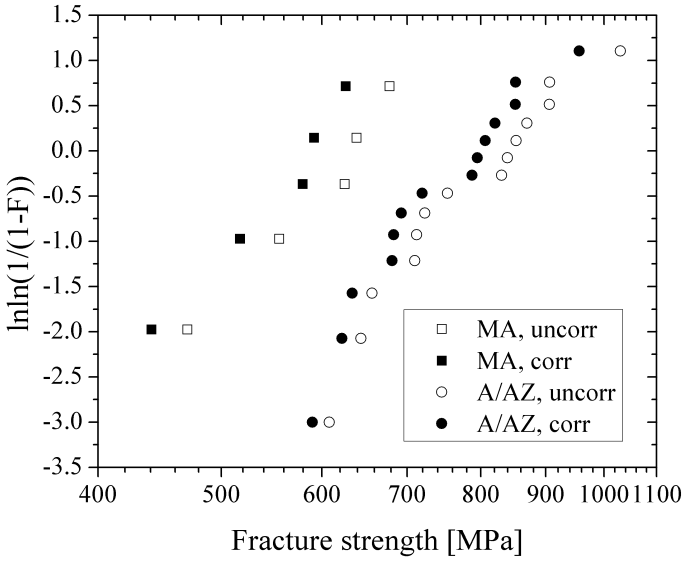

Figure 7.2: Contact strength of monolithic alumina alumina/alumina-zirconia multilayer. Values from numerical (empty symbols) and Finite Elements (solid symbols) solutions are presented.

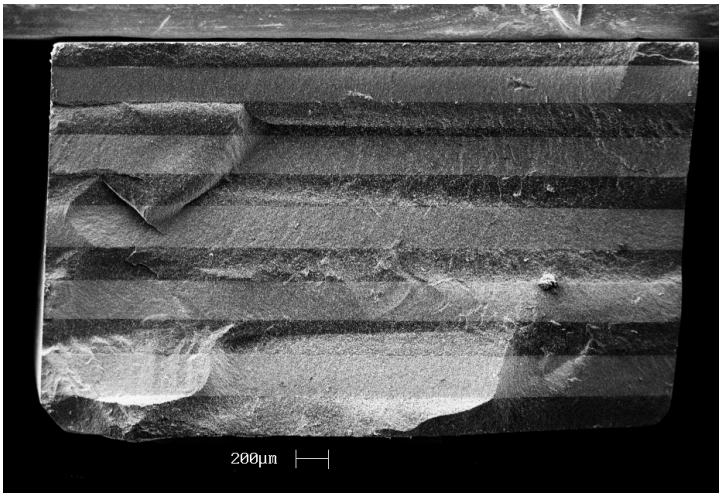

Figure 7.3: Electron Fractography of tested multilayer sample, showing that fracture started from the alumina surface layer.

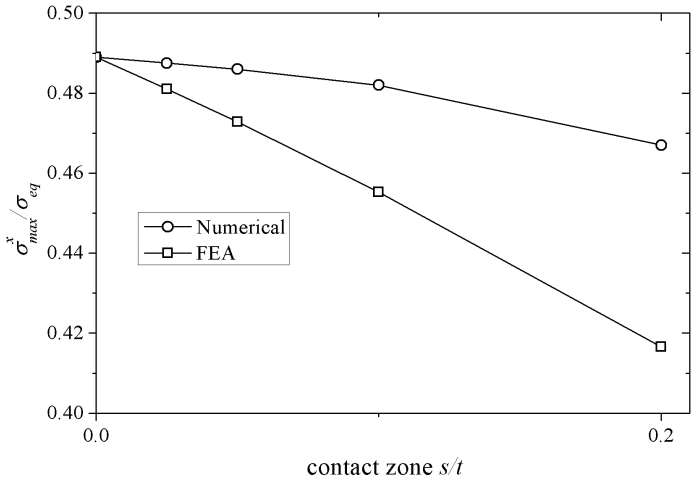

Figure 7.4: Maximum x-direction stress as a function of the contact area. Values from previous numerical calculation (circles) [69] and from the present work (squares). Variation of the former is negligible, while in the latter case should be taken into account.

7.2 Finite Element analysis

Finite Elements calculations in monolithic alumina showed that, with respect to the numerical solutions, a slightly higher decrease of the maximum stress was found with the increment of contact zone width s, reaching values approx. 10% lower in the considered range, as it is shown in Fig. 7.4. This is attributed to the relatively high deformation the material is subjected to, and that is taken into account in the simulation, since the rollers are represented as rigid bodies. This changes slightly the stress field, increasingly as s grows, with respect to the previous, numerical, solutions, which is based on calculations on the undeformed body.

Such effect was corrected by means of a polynomial curve, defined as a function of normalized contact zone s/t, in the formulation:

$$\frac{\sigma_x^{max}}{\sigma_{eq}} \equiv Y = Y_0 - a\left(\frac{s}{t}\right) - b\left(\frac{s}{t}\right)^2 \tag{7.2}$$

Because actual experiments are performed in load control, for an easier application to the experimental results in the specific case, another relation was extracted for the specific case as a function of the normalized load $\sigma_{eq} = F/tb$, presented in section 2.6:

$$Y = Y_0 - a'\sqrt{\sigma_{eq}} - b'\sigma_{eq} \tag{7.3}$$

With Y_0 being the point-load value 0.489, and $a = 0.312$, $b = 0.25$, $a' = 1.3 \cdot 10^{-3}$, $b' = 4 \cdot 10^{-6}$ fitting parameters (for σ_{eq} expressed in MPa).

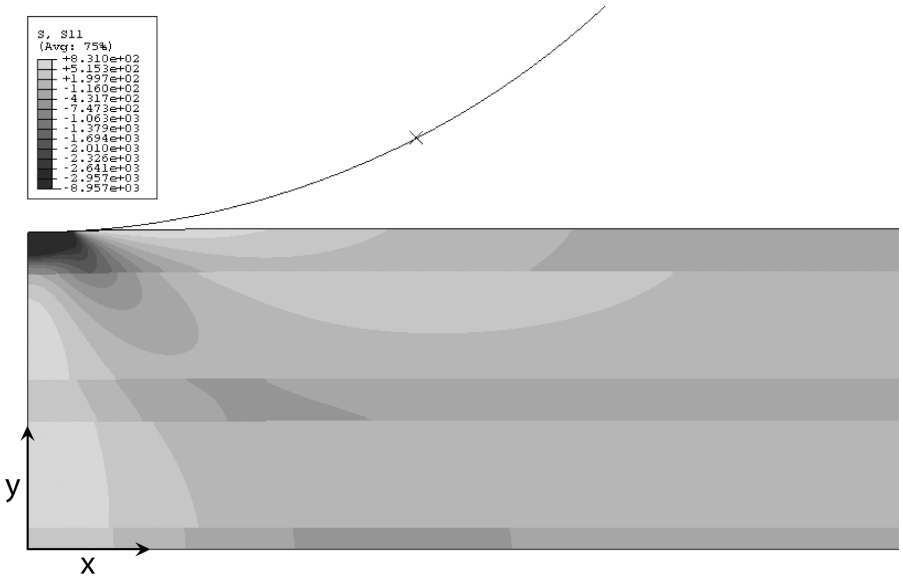

Figure 7.5: FE representation of the typical x-direction stress field in multilayered material, originated from the combination of residual stresses and testing stress fields

The difference with the $Y = constant$ solution is not substantial and could be neglected for the sake of simplicity, with no considerable loss of accuracy, however it should be noticed that the numerical solution overestimates the strength of the material, reducing thus the safety factor. In order to quantify the differences, in the previous section both the numerical and FE values were presented and compared.

Simulations of testing of the laminated material showed that the difference in terms of tensile stress, as it could be expected, corresponds to the amount of residual stress. Apart from that, and a slight shift of the point of maximum stress shown in Fig. 7.6, no substantial difference was found, so that the relation 7.2 can be expressed in a form that includes the residual stress σ_r, leading to:

$$\sigma - \sigma_r = \left(Y_0 - a\left(\frac{s}{t}\right) - b\left(\frac{s}{t}\right)^2 \right) \sigma_{eq} \tag{7.4}$$

The values of the correction curve parameters depend slightly on the geometry and materials of the laminated structure and on the rollers radius; for higher accuracy it can be obtained specifically for any case studied.

Tensile stress along the y-direction, is also subjected to a similar reduction in the maximum value, compared with the classical solution. Correction curves can be obtained

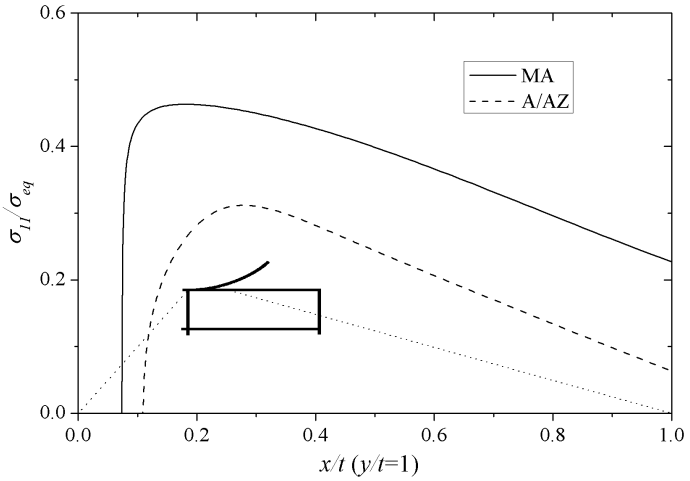

Figure 7.6: Normalized tensile stress in the surface of monolithic alumina and multilayer. The difference in the maximum values coincides with the compressive residual stress in the latter.

for this case as well, for which the best fit was obtained with the relation:

$$Y = Y_0 - a''\sqrt{\frac{s}{t}} - b''\frac{s}{t} \tag{7.5}$$

with $a'' = 0.8024$, $b'' = 0.5969$.

7.3 Considerations on the design with ceramic laminates

It can be noticed from comparison of the values of the parameters in eqs. (7.5) and (7.2) that along the y-axis, as the contact zone increases, the relative stress is reduced with a much higher rate than on the surface. It can be expected therefore, considering also the likely presence of surface flaws, that fracture is more probable to start at the surface.

However, in the case of laminated materials, in contrast with the monolithic case, the combination of residual and applied stress fields on the inner tensile layers of laminates can produce tensile values higher than the corresponding surface stress. Tensile stresses along the y-axis for monolithic and laminated material are reported in Fig. 7.7 a and b, for two arbitrary values of the normalized load σ_{eq}. The contribution from residual stresses is a constant value; therefore, under a low load (Fig. 7.7a), such a contribution is significant, leading to a double total value with respect to that on the surface ($\sigma_x^{max} \approx$

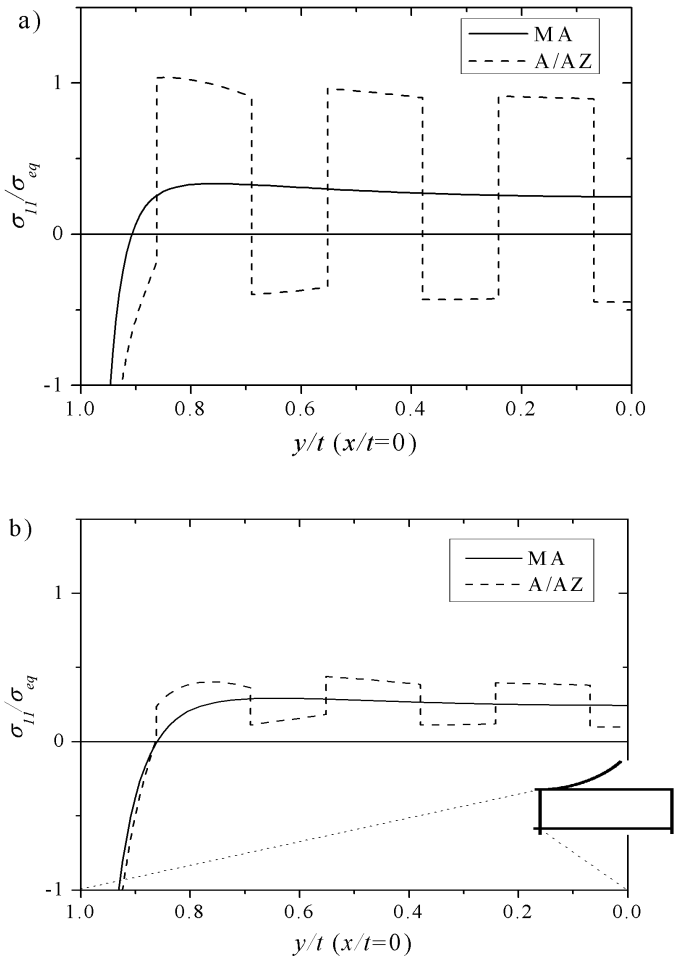

Figure 7.7: Tensile stress along the y-axis ($x/t = 0$) for monolithic and laminated materials under low load, a) and high load b).

σ_{eq}). On the other hand, under a higher load (Fig. 7.7b), the same constant value sums to a value of applied stress which is higher in absolute value, but is lower with respect to the normalized load ($\sigma_x^{max} \approx 0.3\sigma_{eq}$), due to the decrease explained above and reflected in eq. (7.5). Therefore, despite of the presence of the additional tensile contribution given by the residual stresses, the maximum stress along the axis is lower than on the surface.

Such behaviour is summarized in Fig. 7.8, where the maximum stress along the surface and along the y-axis, respectively, of the laminated structure is plotted against the normalized load σ_{eq}. A critical value σ_c^* can be defined, below which stress is higher on the y-axis, and above which it is higher on the surface.

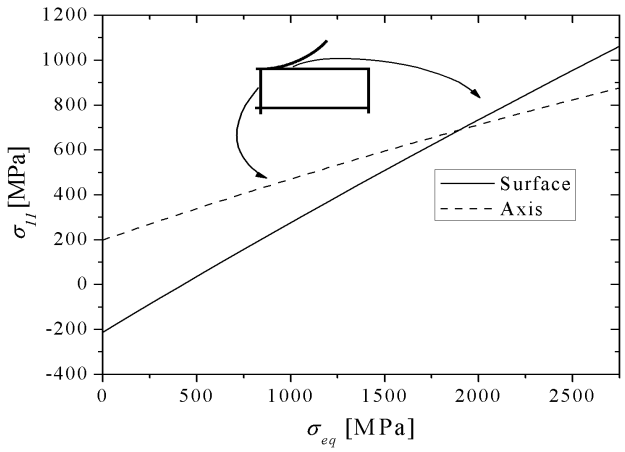

Figure 7.8: Maximum tensile stress along the surface ($y/t = 1$) and the y-axis ($x/t = 0$) for a multilayer material as a function of normalized load σ_{eq}.

It should be noticed that Fig. 7.8 does not allow prediction of the fracture location, unless the strength of both composing materials is known, as well as the flaws distribution. It points out, nevertheless, that fracture could occur on other location than the surface; therefore, when fracture load is near the critical value σ_{eq}^{c}, strength tests should be coupled with micrographic evaluation of the fracture location for a correct understanding of the failure.

In the case presented in this study (section 7.1), for example, the average strength measured coincides with a maximum stress located on the y-axis. Nevertheless, fractography observation, as in Fig. 7.3, showed that fracture started from the outer, compressive, layer.

Such a behaviour can be explained with a different strength of the composing materials, due to the smaller grain size in presence of ZrO_2, which acts as a constraint to the grain growth [100], or to the higher amount of flaws in the surface than in the bulk material.

The correct evaluation of the site of fracture initiation, combined with the calculated normalized load, as in Fig. 7.8, allows one to determine the resistance of the laminated structure, and also the strength of one, typically the weakest, of the composing materials, giving moreover information of a lower limit to the strength of the other.

Alternatively, if the equivalent strength of a laminated structure is compared with tests on similar, unstressed, materials, as in the example below, an estimation of the

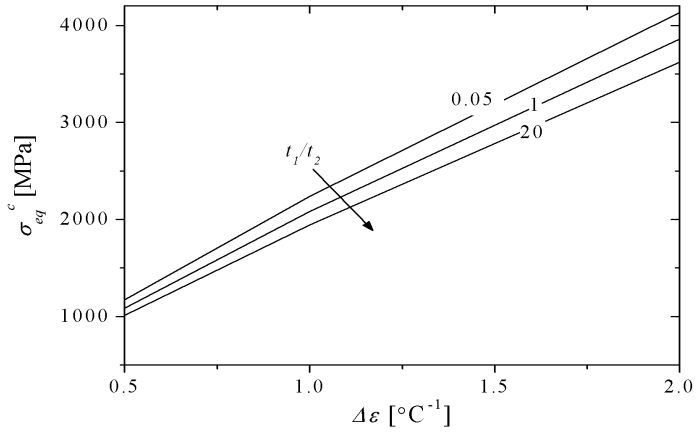

Figure 7.9: Influence of the thermal mismatch and of the tensile versus compressive stress ratio (labelled as t_1/t_2)on the critical normalized load σ^c_{eq} for the switching of the maximum location from y-axis to surface, on laminated materials

residual stresses can be obtained.

Another interesting consideration derived from Fig. 7.8 is that under low normalized load σ_{eq}, the stress on an internal layer of the laminate is higher than on the corresponding monolithic material. If the fracture strength is located in this first range, which is a condition that depends both on the laminated composing materials and geometry, the contribution of the residual stress to the strengthening would result detrimental, instead of beneficial, to the contact strength.

The maximum stress presented in Fig. 7.8 was plotted for a specific laminate. Changes of the geometry and/or of the composing materials influence the global behaviour. As a good approximation, the σ_x^{max} vs σ_{eq} relations, both on the surface and on the axis, as in Fig. 7.8 in presence of residual stress are just shifted from the origin along the y-axis to the respective value of stress. The critical (normalized) load for change of maximum location is shown on Fig. 7.9, where it can be seen that the choice of the composing materials, especially the thermal expansion mismatch, has the greatest influence on the critical load; while such value varies only slightly as the laminated structure, *i.e.* the tensile/compressive stresses ratio, changes.

The general information that can be extracted is that extensive thermal mismatch should be avoided in the laminated design; and that, expectedly enough, higher compressive stresses provide higher contact resistance and lower susceptibility to abnormal

internal fracture. Since the location of the maximum stress on the axis changes, displacing deeper into the material as the contact zone increases, it is possible that the "unstressed" maximum, which is the σ_x stress minus the residual stresses, is located on a compressive layer. In that case, the real maximum value is lower than showed on Fig 7.8. This effect is not predictable *a priori* unless information of the range of fracture stress and of the laminate geometry is provided.

CHAPTER 8

Conclusions

The objective pursued during the development of this thesis was to achieve a complete evaluation of the damage generated by blunt contact loading on all-ceramic laminated composites. The approach chosen was to try to infer conclusions as much general as possible, in order to both reach a deep comprehension of the phenomena taking place during the damage formation and to formulate considerations which could be useful for the improvement of the design of laminated ceramics.

With the same attention to the characterization completeness, the study was structured to follow steps of increasing damage, starting from the appearance of brittle damage and arriving to catastrophic failure of the material.

- The physical and mechanical characterization gave the basis for the successive studies. Although such a characterization was carried on by standard techniques in order to guarantee reproducibility, the issue of residual stress distribution deserved a deeper analysis for the strong implications on all the phases of the study and, for this reason, was examined by means of several techniques, which were compared and combined, providing thus insight of the actual material stress field and explaining the apparent differences arising between the techniques. Among the techniques employed, instrumented indentation resulted to be unsuitable for the class of ceramic materials due to their high hardness, while results from sharp indentation and Finite Element simulation, associated with piezo-spectroscopy analysis from a partner research, showed that the different approaches measure different physical magnitudes, so that a direct comparison may not be correct, but the analysis

can be unified by means of computer-assisted simulations. The residual stresses distribution has much importance both in the correct design and analysis of the experimental tests and in providing guidelines to the optimum design for the employment *in service* of multilayered ceramics.

- The study of the brittle damage appearance showed that ceramic laminates offer higher resistance against blunt contact loading than monolithic materials, and such a result was appreciable also under long-lasting tests (static fatigue) and cyclic loading. The improvement was quantified to be equal approximately, in terms of higher critical load, to the amount of residual stresses. The decrement of critical load as a function of the number of cycles or time for ring crack appearance was rationalized starting from fracture mechanics relations and Paris-like laws, which were adapted to the specific cases of both static and cyclic loading, and which yielded values of the degradation parameters in agreement with the literature. The degradation by cyclic loading showed the unexpected presence of mechanical fatigue mechanisms, consisting in the degradation of the toughening effects generated by bridging of the crack wake. Such fatigue effect, which resulted in a faster degradation compared with static loading, was unexpected for the fine microstructure; for this reason, it was attributed to enhanced quasi-brittle character.

- The superiority of laminated materials over their monolithic counterpart was questioned under severe damage, *i.e.* a high number of cycles under a relatively high load: the reduction of brittle damage, together with the residual stresses, when shear-driven subsurface microcracks (the called "quasi-plasticity") form, enhance the chipping of particles, a phenomenon which can be detrimental, for example, in tribological applications.

- The analysis of the cone crack propagation on the first, compressive layer required first to solve the issue of propagation on polycrystalline materials. Such objective was satisfactorily achieved by means of an automated incremental Finite Element Model, which allowed calculating the influence of crack shielding provided by bridging mechanisms, on the crack propagation and, as a reverse-engineering application, evaluating the amount of mode-I and mode-II shielding on alumina. The values of crack shielding obtained this way are higher than expected if compared with standard fracture toughness measurement, but are in agreement with

those obtained by similar methodologies and with the considerations on mechanic fatigue mechanisms presented above.

- The results obtained this way were expanded to the case of ceramic laminates by including residual stresses, whose influence was evaluated on both stable and unstable crack propagation. A general relationship was established, which relates the angle deviation with the amount of residual stresses and the contact pressure. Results of the simulations were confirmed by experimental measurements.

  It is worth highlighting that the FE model was developed in the optics of adaptability, in that it permits flexibility in the input and output handling, so that a wide number of problems and materials can be treated, suggesting its use as a prediction tool in the evaluation of contact resistance.

- The coupling of computer simulation and experiments allowed to quantify the effect of cone crack on the material integrity, or, in other words, on the strength degradation, and to highlight the advantages (and, in some cases, the risks) offered by a laminated ceramic structure. A predictive relation based on the elastic mismatch between layers, on the presence of residual stress and on the effect of such stresses on the geometry of the cone crack was established and confirmed by experimental tests.

- Considerations for the design focused to the *in service* application were established also from the study of catastrophic failure under contact loading, which, again, was performed by means of experimental tests coupled with Finite Element simulation, which assisted in refining the analytical expressions ruling the stress state under such a test. Both experimental and calculated results showed again a better behaviour of laminated materials compared to the reference monolithic alumina, but highlighted the risk of generating high stress in the underlying tensile layers. Such risk was quantified, in terms of a critical load for the change of the maximum stress location, as a function of the thermal mismatch between the materials composing the multilayer.

Future work

During the development of the work that led to this thesis, it was tried to perform a comprehensive analysis of the damage produced on ceramic materials, with the special focus on ceramic laminates, by blunt, localized, loading. Such a wide range of objectives required to establish some boundaries to the specific themes to be treated, to avoid excessive dispersion and loss of depth of the study. For this reason, it was decided to focus on the brittle character of the contact damage, neglecting, apart in some case worth mentioning, the quasi-plastic deformation caused by subsurface microcracking. For this reason, the logical step towards a complete understanding of the damage mechanisms acting in this class of materials would be an analysis of such quasi-plastic damage. From the experience acquired during and from works in the literature, it appears that the issue that deserves more attention is the effect of the type of loading (monotonic, cyclic, static) on the prevalence of inelastic or brittle damage; this study could be related to the analysis of how quasi-plastic and brittle damage influence each other. It is thought that the Finite Element Model of crack propagation could be adapted to include quasi-plastic deformation either as a plastic-like constitutive equation, as an elastic degradation law, more proper for damage in ceramics, or as a mesh of cohesive elements.

Bibliography

[1] Munz, D. *What can we learn from R-curve measurements?* J Am Ceram Soc 2007: **90**(1), 1–15

[2] Laraia, V. and Heuer, A. *Novel composite microstructure and mechanical-behavior of mollusk shell* J Am Ceram Soc 1989: **72**(11), 2177–2179

[3] Clegg, W., Kendall, K., Alford, N., Button, T.W., and Birchall, J.D. *A simple way to make tough ceramics* Nature 1990: **347**, 455–457

[4] Kovar, D., Thouless, M. and Halloran, J. *Crack deflection and propagation in layered silicon nitride/boron nitride ceramics* J Am Ceram Soc 1988: **81**(4), 1004–1012

[5] Mawdlsey, J., Kovar, D. and Halloran, J. *Fracture behavior of alumina/monazite multilayer laminates* J Am Ceram Soc 2000: **83**(4), 802–808

[6] Marshall, D., Morgan, P. and Housley, R. *Debonding in multilayered composites of zirconia and $LaPO_4$* J Am Ceram Soc 1997: **80**(7), 1677–1683

[7] O'Brien, M., Capaldi, F. and Sheldon, B. *A layered composite tested at high temperature* J Am Ceram Soc 2000: **83**(12), 3033–3040

[8] Lee, S.J. and Kriven, W. *Toughened oxide composites based on porous alumina-platelet interphases* J Am Ceram Soc 2001: **84**(4), 767–774

[9] Marshall, D., Ratto, J., and Lange, F. *Enhanced fracture toughness in layered microcomposites of Ce-ZrO_2 and Al_2O_3* J Am Ceram Soc 1991: **74**(12), 2979–2987

[10] Sánchez-Herencia, A., Pascual, C., He, J. and Lange, F. *ZrO_2 / ZrO_2 layered composites for crack bifurcation* J Am Ceram Soc 1999: **82**(6), 1512–1518

[11] Bermejo, R., Torres, Y., Snchez-Herencia, A., Baudn, C., Anglada, M. and Llanes, L. *Fracture behaviour of an Al_2O_3-ZrO_2 multilayered ceramic with residual stresses due to phase transformations* Fatigue Fract Engng Mater Struct 2006: **29**, 71–78

[12] Chartier, T., Merle, D. and Besson, J. *Laminar ceramic composites* J Eur Ceram Soc 1994: **15**, 101–107

[13] Virkar, A.V., Fong Jue, J., Hansen, J.J. and Cutler, R.A. *Measurement of residual stresses in oxide-ZrO_2 three-layer composites* J Am Ceram Soc 1988: **71**(3), C148–C151

[14] Ho, S., Hillman, C., Lange, F.F. and Suo, Z. *Surface cracking in layers under biaxial, residual compressive stress* J Am Ceram Soc 1995: **78**(9), 2353–2359

[15] Hansen, J., Cutler, R., Shetty, D. and A.V., V. *Indentation fracture response and damage resistance of Al_2O_3-ZrO_2 composites strengthened by transformation-induced residual stresses* J Am Ceram Soc 1988: **71**(12), C501–C505

[16] Lakshminarayanan, R., Shetty, D. and R.A., C. *Toughening of layered ceramic composites with residual surface compression* J Am Ceram Soc 1996: **79**(1), 79–87

[17] Russo, C., Harmer, M., Chan, H. and Miller, G. *Design of a laminated ceramic composite for improved strength and toughness* J Am Ceram Soc 1992: **75**(12), 3396–3400

[18] Moon, R., Hoffman, M., Hilden, J., Bowman, K., Trumble, K. and Rodel, J. *Weight function analysis on the R-curve behavior of multilayered alumina-zirconia composites* J Am Ceram Soc) 2002: **85**(6), 1505–11

[19] Lube, T., Pascual, J., Chalvet, F. and de Portu, G. *Effective fracture toughness in $Al_2O_3Al_2O_3/ZrO_2$ laminates* J Eur Ceram Soc 2007: **27**(2–3), 1449–1453

[20] Toschi, F., Melandri, C., Pinasco, P., Roncari, E., Guicciardi, S. and de Portu, G. *Influence of residual stresses on the wear behavior of Alumina/Alumina-Zirconia laminated composites* J Am Ceram Soc 2003: **86**(9), 1547–1553

[21] Hertz, H. *Hertz's Miscellaneous Papers; Chs. 5 and 6* MacMillan 1896

[22] Johnson, K. *Contact mechanics* Cambridge University Press (Cambridge) 1985

[23] Auerbach, F. Annalen der Physik 1891: **43**, 61–100

[24] Fischer-Cripps, A. *Predicting Hertzian fracture* J Mat Sci 1997: **32**, 1277–1285

[25] Roesler, F. *Brittle fracture near equilibrium* Proc Phys Soc London 1956: **B69**, 981–992

[26] Frank, F. and Lawn, B. *On the theory of Hertzian fracture* Proc R Soc London, Ser A 1967: **299**, 291–306

[27] Langitan, F. and Lawn, B. *Hertzian fracture experiments on abraded glass surfaces as definitive evidence for an energy balance explanation of auerbach's law* J Appl Phys 1969: **40**(10), 4009–4017

[28] Dai, D., Hills, D., Warren, P. and Nowell, D. *The propulsion of surface flaws by elastic indentation testing* Acta Metall Mater 1995: **43**(3), 985–991

[29] Licht, V., Hulsmeier, P. and Fett, T. *Probability of cone crack initiation due to spherical contact loading* J Eur Ceram Soc 2004: **24**(10–11), 2907–2915

[30] Langitan, F. and Lawn, B. *Effect of a reactive environment on the Hertzian strength of brittle solids* J Appl Phys 1970: **41**(8), 3357–3365

[31] Johnson, K., O'Connor, J. and Woodward, A. *The effect of the indenter elasticity on the Hertzian fracture of brittle materials* Proc R Soc Lond A 1973: **334**, 95–117

[32] Warren, R. *Measurement of the fracture properties of brittle solids by Hertzian indentation* Acta Metall 1978: **26**, 1759–1769

[33] Mouginot, R. and Maugis, D. *Fracture indentation beneath flat and spherical punches* J Mat Sci 1985: **20**, 4354–4376

[34] Lawn, B., Wiederhorn, S. and Johnson, H. *Strength degradation of brittle surfaces: blunt indenters* J Am Ceram Soc 1975: **58**(9–10), 428–432

[35] Zeng, K., Breder, K. and Rowcliffe, D. *The Hertzian stress field and formation of cone cracks - II. determination of fracture toughness* Acta Metall Mater 1992: **40**(10), 2601–2605

[36] Warren, P. *Determining the fracture toughness of brittle materials by Hertzian indentation* J Eur Ceram Soc 1995: **15**, 201–207

[37] Geandier, G., Denis, S. and Mocellin, A. *Float glass fracture toughness determination by Hertzian contact: experiments and analysis* J Non-Cryst Sol 2003: **318**, 284–295

[38] Kocer, C. and Collins, R. *Angle of Hertzian cone cracks* J Am Ceram Soc 1998: **81**(7), 1736–1742

[39] Kocer, C. *An automated incremental finite element study on Hertzian cone crack growth* Fin Elem Anal Des 2002: **39**, 639–660

[40] Fett, T., Rizzi, G. and Diegele, E. *Weight functions for cone cracks* Eng Frac Mech 2004: **71**(16–17), 2551–2560

[41] Ebrahimi, M., Chevalier, J. and Fantozzi, G. *R-curve evaluation and bridging stress determination in alumina by compliance analysis* J Eur Ceram Soc 2003: **23**, 943–949

[42] Ceseracciu, L., Jiménez-Piqué, E. and Anglada, M. *Cone cracks in laminated ceramics with residual stress* in B. Wilshire and M. Bache, eds., *Proceedings of the 10th European Inter-regional conference on Ceramics* Swansea Materials Research Center 2006: 199–208

[43] Fett, T., Ernst, E., Rizzi, G., Munz, D., Badenheim, D. and Oberacker, R. *Sphere*

contact fatigue of a coarse-grained Al_2O_3 ceramic Fatigue Fract Eng Mater Struct 2006: **29**(11), 876–86

[44] Guiberteau, F., Padture, N.P., Cai, H. and Lawn, B.R. *A simple cyclic Hertzian test for measuring damage accumulation in polycristalline ceramics* Phil Mag A 1993: **68**(5), 1003–1016

[45] Kim, D., Jung, Y., Peterson, I. and Lawn, B. *Cyclic fatigue of intrinsically brittle ceramics in contact with spheres* Acta Mater 1999: **47**(18), 4711–4725

[46] Swain, M. and Hagan, J. *Indentation plasticity and the ensuing fracture of glass* J Phys D: Appl Phys 1976: **9**, 2201–2214

[47] Lawn, B.R., Padture, N.P., Cait, H. and Guiberteau, F. *Making Ceramics "Ductile"* Science 1994: **263**(5150), 1114–1116

[48] Lawn, B. *Indentation of ceramics with spheres: a century after Hertz* J Am Ceram Soc 1998: **81**(8), 1977–1994

[49] Guiberteau, F., Padture, N. and Lawn, B. *Effect of grain size on Hertzian contact damage in alumina* J Am Ceram Soc 1994: **77**(7), 1825–1831

[50] Lee, K., Jung, Y.G., Peterson, I. and Lawn, B. *Model for cyclic fatigue of quasi-plasti ceramics in contact with spheres* J Am Ceram Soc 2000: **83**(9), 2255–2262

[51] Swadener, J., Taljat, B. and Pharr, G. *Measurement of residual stress by load and depth sensing indentation with spherical indenters* J Mater Res 2001: **16**(7), 2091–2102

[52] Wei, L. and Lawn, B. *Thermal wave analysis of contact damage in ceramics: case study on alumina* J Mater Res 1996: **11**(4), 939–947

[53] Fischer-Cripps, A. *Elasticplastic behaviour in materials loaded with a spherical indenter* J Mater Sci 1997: **32**(3), 727–736

[54] Licht, V., Ernst, E. and Huber, N. *Simulation of the Hertzian contact damage in ceramics* Modell Simul Mater Sci Eng 2003: **11**(4), 477–486

[55] Rhee, Y.W., Kim, H.W., Deng, Y. and Lawn, B.R. *Brittle fracture versus quasi plasticity in ceramics: a simple predictive index* J Am Ceram Soc 2001: **84**(3), 561–565

[56] Lee, S., Wuttiphan, S. and Lawn, B. *Role of microstructure in Hertzian contact damage in silicon nitride: I, mechanical characterization* J Am Ceram Soc 1997: **80**(9), 2367–2381

[57] Lee, K., Lee, S. and Lawn, B. *Contact fatigue in silicon nitride* J Am Ceram Soc 1999: **82**(5), 1281–1288

[58] Latella, B., Liu, T. and Atanacio, A. *Effect of grain size on Hertzian contact damage in 9mol% Ce–TZP ceramics* J Eur Ceram Soc 2002: **22**, 1971–1979

[59] Padture, N. and Lawn, B. *Fatigue in ceramics with interconnecting weak interfaces: a study using cyclic Hertzian contacts* Acta Metall Mater 1995: **43**(4), 1609–1617

[60] Giannakopoulos, A. *Indentation of graded substrates* Thin Solid Films 1998: **332**, 172–179

[61] Jitcharoen, J., Padture, N., Giannakopoulos, A. and Suresh, S. *Hertzian-crack suppression in ceramics with elastic-modulus-graded surfaces* J Am Ceram Soc 1998: **81**(9), 2301–2308

[62] An, L., Chan, H., Padture, N. and Lawn, B. *Damage-resistant alumina-based layer composites* J Mater Res 1996: **11**(1), 204–210

[63] Lee, S. and Lawn, B. *Contact damage and strength degradation in brittle/quasi-plastic silicon nitride bilayers* J Am Ceram Soc 1998: **81**(9), 2394–2404

[64] Miranda, P., Pajares, A., Guiberteau, F., Deng, Y. and Lawn, B. *Designing damage-resistant brittle-coating structures: I. bilayers* Acta Mater 2003: **51**, 4347–4356

[65] Jung, Y.G., Wuttiphan, S., Peterson, I. and Lawn, B. *Damage modes in dental layer structures* J Dent Res 1999: **78**(4), 887–897

[66] Lawn, B., Deng, Y. and Thompson, V. *Use of contact testing in the characterization and design of all-ceramic crownlike layer structures: a review* J Prosthet Dent 2001: **86**(5), 495–510

[67] Fett, T., Ernst, E. and Munz, D. *Contact strength measurements of bars under opposite sphere loading* J Mat Sci Lett 2002: **21**(24), 1955–1957

[68] Fett, T., Ernst, E., Rizzi, G. and Oberacker, R. *Failure of an Al_2O_3 ceramic under cyclic sphere contact loading* J Mater Sci Lett 2004: **39**, 6817–6819

[69] Fett, T., Munz, D. and Thun, G. *Test devices for strength measurements of bars under contact loading* J Test Eval 2001: **29**(1), 1–10

[70] Fiori, C. and de Portu, G. *Tape casting: a technique for preparing and studying new materials.* in W. Davidge, ed., *British Ceramic Proceedings No. 38 - Novel Ceramic Fabrication Processes and Applications,* 1986: 213

[71] Oliver, W. and Pharr, G. *An improved technique for determining hardness and elastic modulus using load and displacement sensing indentation experiments* J Mater Res 1992: **7**(6), 1564–8

[72] Hay, J., Bolshakov, A. and Pharr, G. *A critical examination of the fundamental*

relations used in the analysis of nanoindentation data J Mater Res 1999: **14**(6), 2296–2305

[73] Anstis, G., Chantikul, P. and Lawn, B.R. Marshall, D. *A critical evaluation of indentation techniques for measuring fracture toughness: I, direct crack measurements* J Am Ceram Soc 1981: **64**(9), 533–538

[74] Suresh, S. and Giannakopoulos, E. *A new method for estimating residual stresses by instrumented sharp indentation* Acta Mater 1998: **46**(16), 5755–5767

[75] Tsui, T., Oliver, W. and Pharr, G. *Influences of stress on the measurement of mechanical properties using nanoindentation. i. experimental studies in an aluminum alloy* J Mater Res 1996: **11**(3), 752–759

[76] Dahmani, F., Lambropoulos, J., Schmid, A., Burns, S. and Pratt, C. *Nanoindentation technique for measuring residual stress field around a laser-induced crack in fused silica* J Mat Sci 1998: **33**, 4677–4685

[77] Xu, Z.H. and Li, X. *Influence of equi-biaxial residual stress on unloading behaviour of nanoindentation* Acta Mater 2005: **53**(7), 1913–1919

[78] de Portu, G., Micele, L., Sekiguchi, Y. and Pezzotti, G. *Measurement of residual stress distributions in Al_2O_3/3Y-TZP multilayered composites by fluorescence and raman microprobe piezo-spectroscopy* Acta Mater 2005: **53**(5), 1511–1520

[79] Fett, T., Creek, D., Badenheim, D. and Oberacker, R. *Crack growth data from dynamic tests under contact loading?* J Eur Ceram Soc 2004: **24**, 2049–2054

[80] Karlsson Sorensen *ABAQUS Documentation v. 6.6* 2006

[81] Hillman, C., Suo, Z. and Lange, F. *racking of laminates subjected to biaxial tensile stress* J Am Ceram Soc 1996: **78**(8), 2127–2133

[82] Cotterell, B. and, R.J. *Slightly curved or kinked cracks* Int J Fract 1980: **16**, 155–169

[83] Fett, T. and Munz, D. *Kinked cracks and richard criterion* Int J Fract 2002: **115**, 69–73

[84] Roberts, S., Lawrence, C., Bisrat, Y., Warren, P. and Hills, D. *Determination of surface residual stresses in brittle materials by Hertzian indentation:theory and experiment* J Am Ceram Soc 1999: **82**(7), 1809–1816

[85] van der Laag, N., Dortmans, L. and de With, G. *Influence of relative humidity on mechanical properties of alumina, pzt and zirconia* Key Eng Mater 2002: **206**(2), 751–754

[86] Li, M. and Guiu, F. *Subcritical crack growth in alumina – i. effects of grain size,*

specimen size and loading mode Acta Metall Mater 1995: **43**(5), 1859–1869

[87] Guiu, F., Reece, M. and Vaughan, D. *Cyclic fatigue of ceramics.* J Mater Sci 1991: **26**, 3275–3286

[88] Healy, J., Bushby, A., Mai, Y.W. and Mukhopadhyay, A. *Cyclic fatigue of long and short cracks in alumina* J Mat Sci 1997: **32**, 741–747

[89] Geraghty, R., Hay, J. and White, K. *Fatigue degradation of the crack wake zone in monolithic alumina* Acta Mater 1999: **47**(4), 1345–1353

[90] Kruzic, J., Cannon, R. and Ritchie, R. *Crack-size effect on cyclic and monotonic crack growth in polycristalline alumina: quantification of the role of grain bridging* J Am Ceram Soc 2004: **87**(1), 93–103

[91] Jacobs, D. and Chen, I.W. *Cyclic fatigue in ceramics: a balance between crack shielding accumulation and degradation* J Am Ceram Soc 1995: **78**(3), 513–520

[92] Warren, P., Hills, D. and Dai, D. *Mechanics of Hertzian cracking* Trib Int 1995: **28**(6), 357–362

[93] Fett, T., Keller, R., Munz, D., Ernst, E. and Thun, G. *Fatigue of alumina under contact loading* Eng Frac Mech 2003: **70**, 1143–1152

[94] Barinov, S., Ivanov, N., Orlov, S. and Shevchenko, V. *Influence of environment on delayed failure of alumina ceramics* J Eur Ceram Soc 1998: **18**, 2057–2063

[95] Warren, P. and Hills, D. *The influence of elastic mismatch between indenter and substrate on Hertzian fracture* J Mat Sci 1994: **29**, 2860–2866

[96] Kara, H. and Roberts, S. *Polishing behavior and surface quality of alumina and alumina/silicon carbide nanocomposites* J Am Ceram Soc 2000: **83**(5), 1219–1225

[97] Ramachandran, N. and Shetty, D.K. *Rising crack-growth-resistance (R-curve) behavior on toughened alumina and silicon nitride* J Am Ceram Soc 1991: **74**(10), 2634–41

[98] Belmonte, M., Miranzo, P. and Osendi, I. *Mechanical properties and contact damage behavior in aligned silicon nitride materials* J Am Ceram Soc 2007: **90**(4), 1157–1163

[99] Cai, P., Green, D. and Messing, G. *Mechanical characterization of Al_2O_3/ZrO_2 hybrid laminates* J Eur Ceram Soc 1998: **5**, 2025–2034

[100] Nagl, M., Llanes, I., Fernandez, R. and Anglada, M. *The fatigue behaviour of Mg-PSZ and ZTA ceramics* Fracture Mechanics of Ceramics Vol12 Fatigue, Composites, and High-Temperature Behavior 1996: 61–76

APPENDIX A

Script codes of the FE model

In this section the three scripts composing the automated model of crack propagation are analyzed in detail.

A.1 propcrack.py

```
'''
propcrack.py
Crack propagation: root model
'''
```

Headings of the script; name and scope

```
from odbAccess import *
import visualization

fields=(('Project name', ''), ('Number of increments',''),
  ('Initial depth [microns]','-4'), ('Contact radius [microns]',
  '100'), ('c0/a','1.1'),('Initial defect c0/a [microns]','0.3'),
  ('Initial increment dc [microns]:\t approx half the defect','0.2'))
mdname, stepss, dep, rad, rovera, defect, incr =getInputs(fields=
  fields, label='Initial data')
```

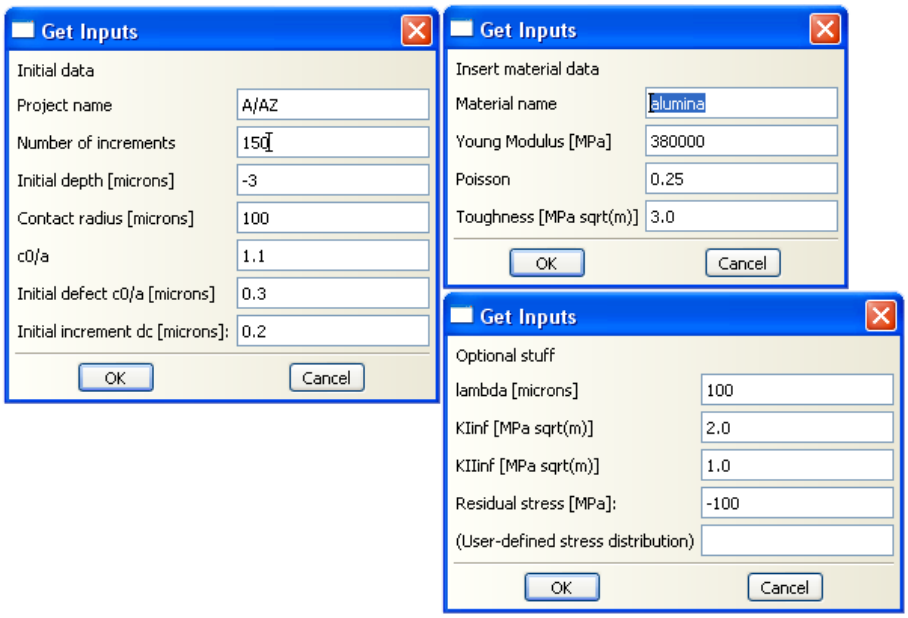

Figure A.1: Input request windows

```
fields4=(('Material name','alumina'), ('Young Modulus [MPa]',
  '380000'), ('Poisson','0.25'), ('Toughness [MPa sqrt(m)]','3.0'))
matname, youn, poiss, KIcrit=getInputs(fields=fields4, label=
  'Insert material data')

fields2=(('lambda [microns]','100'),('KIinf [MPa sqrt(m)]','0.0'),
  ('KIIinf [MPa sqrt(m)]','0.0'), ('Residual stress [MPa]:\t positive
   if compressive','0.0'),('(User-defined stress distribution)',''))
lambd, Kinf, Kinf2, resstr, udsd =getInputs(fields=fields2, label=
  'Optional features')
```

The user is requested to define the initial conditions of the system in request windows, as in Fig. A.1, respectively the indentation parameters, the material properties, eventual additional features.

```
reply = getWarningReply(message='Check on toughness?', buttons=
  (YES,NO))
```

```
if reply == YES:
    incrdep=TRUE
elif reply == NO:
    incrdep=FALSE
```

Activates the function of check on the toughness.

```
stepss=float(stepss)
dep=float(dep)
rad=float(rad)
rovera=float(rovera)
incr=float(incr)
defect=float(defect)
youn=float(youn)
poiss=float(poiss)
KIcrit=1000*float(KIcrit)
resstr=float(resstr)
lambd=float(lambd)
Kinf=1000*float(Kinf)
Kinf2=1000*float(Kinf2)
```

The input variables are converted to script variables.

```
rad0=100
pict=FALSE
```

Activates the function of picture capturing after every step

```
ang=270
```

The local variable of the crack angle is initialized

```
crl=defect
```

The initial crack length is equal to the user-defined defect

```
nrmlzator=rad0/rad
KIcrit=KIcrit*sqrt(nrmlzator)
Kinf=Kinf*sqrt(nrmlzator)
Kinf2=Kinf2*sqrt(nrmlzator)
lambd=lambd*nrmlzator
```

The normalization parameter κ is defined and applied to the relevant properties

```
KIcum=[]
angcum=[]
```

The cumulative arrays which will save the data of local angle and stress intensity factor are initialized

```
xyCoordsCrack = [(rad0*rovera,0.), (rad0*rovera,-defect+incr),
  (rad0*rovera,-defect)]
seedCrack=0.2
```

A crack geometry coordinates array is defined as the initial defect:

$$[c_x, c_y] = [(r, 0), (r, -c_0)] \tag{A.1}$$

```
execfile('model.py', __main__.__dict__)
myJob.submit()
myJob.waitForCompletion()
```

The model is generated with the imposed characteristics (see section A.2)

```
execfile('output.py')
#odb.close()
```

The `output.py` script elaborates the output

```
logr=open(mdname+".txt",'a')
logr.write('step c c/a angle Dang KInorm KII depth tipX tipY load%
  G\n')
logr.close()
```

A `.txt` file is created with the name of the model and initialized.

```
for i in range(stepss):
```

An iterative procedure is repeated for the given number of steps

```
logr=open(mdname+".txt",'a')
if crl>3.0:
    incr=0.6
    seedCrack=0.3
if crl>20.0:
    incr=1.0
    seedCrack=0.5
if crl>30.0:
    incr=2.0
    seedCrack=1.0
if crl>40.0:
   seedCrack=2.0
```

For reducing the calculation time far from the high stress gradient zone, the crack increment δc is augmented as the crack propagates

```
if incrdep and (KIav-KiSh)<KIcrit:
    print "st: %s, c: %s, ang: %s, Dang: %s, KI: %s, KII: %s,%
      dep: %s, tip: %s,%s, load: %s, G: %s"% (i, crl/nrmlzator,%
      360-ang, deltaang2, (KIav-KiSh)/sqrt(nrmlzator)*1E-3,%
      KIIav*1E-3/sqrt(nrmlzator), dep/nrmlzator, lastP[0]/%
      nrmlzator, lastP[1]/nrmlzator, -loadcalc*1e-6/nrmlzator**2,
```

```
      Jint)
     print "increasing depth..."
    logr.write('%s %s %s %s %s %s %s %s %s %s %s %s\n'% (i,
      crl/nrmlzator, crl/rad0, 360-ang, deltaang2, (KIav-KiSh)
      /sqrt(nrmlzator)*1E-3, KIIav*1E-3/sqrt(nrmlzator),
      dep/nrmlzator,lastP[0]/nrmlzator, lastP[1]/nrmlzator,
       -loadcalc*1e-6/nrmlzator**2, Jint))
    dep=dep*(KIcrit*1.01)/(KIav-KiSh)
    myModel.boundaryConditions['load'].setValues(u2=dep)
    myJob.submit()
    myJob.waitForCompletion()
    execfile('output.py')
```

If the toughness check function is active and the stress intensity factor is lower than the toughness, the current vlaues are written in the result file and a new case is computed with the same geometry and an updated penetration depth, following eq. 3.5

```
else:
    print "st: %s, c: %s, ang: %s, Dang: %s, KI: %s, KII: %s, dep:
       %s, tip: %s,%s, load: %s, G: %s"% (i, crl/nrmlzator, 360-ang,
       deltaang2, (KIav-KiSh)/sqrt(nrmlzator)*1E-3, KIIav*1E-3/
       sqrt(nrmlzator), dep/nrmlzator, lastP[0]/nrmlzator,
       lastP[1]/nrmlzator, -loadcalc*1e-6/nrmlzator**2, Jint)
    logr.write('%s %s %s %s %s %s %s %s %s %s %s %s\n'% (i,
      crl/nrmlzator, crl/rad0, 360-ang, deltaang2, (KIav-KiSh)/
      sqrt(nrmlzator)*1E-3, KIIav*1E-3/sqrt(nrmlzator),
      dep/nrmlzator, lastP[0]/nrmlzator, lastP[1]/nrmlzator,
       -loadcalc*1e-6/nrmlzator**2, Jint))
    ang=ang+deltaang2
    angcum.append(360-ang)
    xyCoordsCrack=xyCoordsCrack + [(lastP[0]+
      incr*cos(degreeToRadian(ang)), lastP[1]+
      incr*sin(degreeToRadian(ang)))]
    KIcum.append(KIav)
```

```
    crl=crl+incr
```

If $K_I < K_{Ic}$, the crack geometry array is updated with a new point corresponding to:

$$(c_{xi+i}, c_{yi+1}) = (c_{xi} + \delta c \cos\beta, c_{yi} + \delta c \sin\beta) \tag{A.2}$$

where β is the kink angle calculated by the `output.py` script.

```
        logv=open(mdname+"var.txt", 'w')
        logv.write('%s \n %s \n %s \n %s'
          %(xyCoordsCrack,dep,ang,crl))
        logv.close()
```

A backup file is created with the crack geometry for resuming the calculation from the latest position

```
        execfile('model.py', __main__.__dict__)
        myJob.submit()
        myJob.waitForCompletion()
        execfile('output.py')
    logr.close()
```

The result file is closed. It is opened at the beginning of each step as a security measure, to avoid losing data in case of calculation errors.

A.2 `model.py`

```
'''
incrmod1t.py
iterative model with just one script!
'''
```

Headings of the script; name and scope

```
from abaqus import *
from abaqusConstants import *
import sketch
import part
import mesh
```

The necessary functions are called

```
myModel = mdb.Model(name=mdname)
```

A new model is created with the name given by the user

```
mySketch = myModel.Sketch(name='basicgeom', sheetSize=3000.0)
mySketch.ObliqueConstructionLine(point1=(0.0, -250.0),
    point2=(0.0, 250.0))
xyCoordsBase = [(0,0), (rad0,0), (2000,0), (2000,-2000), (0,-2000),
  (0,0)]
for i in range(len(xyCoordsBase)-1): mySketch.Line(
  point1=xyCoordsBase[i], point2=xyCoordsBase[i+1])
myPart=myModel.Part(name='body', dimensionality=AXISYMMETRIC,
  type= DEFORMABLE_BODY)
myPart.BaseShell(sketch=mySketch)
```

The sample body is created from a sketch

```
my2Sketch = myModel.Sketch(name='crack', sheetSize=2000.0)
lastP = xyCoordsCrack[-1]
for i in range(len(xyCoordsCrack)-1):
    my2Sketch.Line(point1=xyCoordsCrack[i], point2=xyCoordsCrack[i+1])
my2Sketch.CircleByCenterPerimeter(center=(lastP),
  point1=(xyCoordsCrack[-2]))
```

The sketch of the crack is created from the crack geometry array defined above. A variable is defined corresponding to the tip of the crack

```
f=myPart.faces.findAt((0,0,0))
myPart.PartitionFaceBySketch(faces=f, sketch=my2Sketch)
sk=myModel.Sketch(name='rectgle', sheetSize=200)
pointTrans2=(ceil((lastP[0]+10)/4.5)*4.5,floor((lastP[1]-20)/4.5)*4.5)
sk.rectangle(point1=(0,0), point2=pointTrans2)
sk.rectangle(point1=(0,0), point2=(pointTrans2[0]+3,pointTrans2[1]-3))
```

The sample is partitioned to generate a mesh transition, whose size depends on the crack tip position

```
tr1=sk.Line((pointTrans2[0],-1.5),(pointTrans2[0]+1.5,-1.5))
tr2=sk.Line((pointTrans2[0]+1.5,-1.5),(pointTrans2[0]+3,0))
tr3=sk.Line((pointTrans2[0]+1.5,-1.5), (pointTrans2[0]+1.5,-3))
tr4=sk.Line((pointTrans2[0],-3), (pointTrans2[0]+1.5,-3))
tr5=sk.Line((pointTrans2[0]+1.5,-3), (pointTrans2[0]+3,-4.5))
tr6=sk.Line((pointTrans2[0],-4.5), (pointTrans2[0]+3,-4.5))
sk.linearPattern(objectList=(tr1,tr2,tr3,tr4,tr5,tr6),
  number1=-int(pointTrans2[1]/4.5), spacing1=4.5, angle1=270)

rr1=sk.Line((0,pointTrans2[1]-3), (1.5,pointTrans2[1]-1.5))
rr2=sk.Line((4.5,pointTrans2[1]-3), (4.5,pointTrans2[1]))
rr3=sk.Line((1.5,pointTrans2[1]-1.5), (1.5,pointTrans2[1]))
rr4=sk.Line((1.5,pointTrans2[1]-1.5), (3,pointTrans2[1]-1.5))
rr5=sk.Line((3,pointTrans2[1]-1.5), (3,pointTrans2[1]))
rr6=sk.Line((3,pointTrans2[1]-1.5), (4.5,pointTrans2[1]-3))
sk.linearPattern(objectList=(rr1,rr2,rr3,rr4,rr5,rr6),
  number1=int(pointTrans2[0]/4.5), spacing1=4.5, angle1=0)
f=myPart.faces.findAt((0,0,0))
myPart.PartitionFaceBySketch(faces=f, sketch=sk)
```

The one-to-three-elements sketch shown in Fig. A.2 is reproduced along the transition border

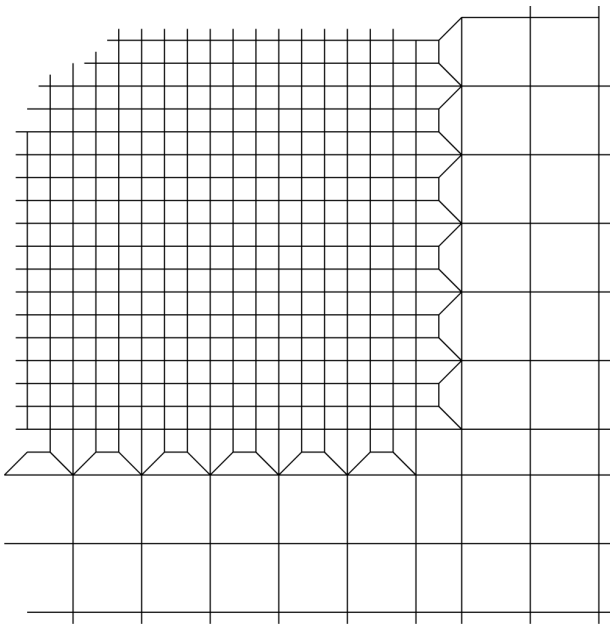

Figure A.2: One-to-three elements transition

```
import material
import section
myModel.Material(name=matname)
myModel.materials[matname].Elastic(table=((youn, poiss), ))
myModel.HomogeneousSolidSection(name=matname+"sec", material=matname,
  thickness=1.0)
allfaces=myPart.faces
myPart.Set(faces=allfaces, name='regall')
myPart.SectionAssignment(region=myPart.sets['regall'], sectionName=
  matname+"sec")
```

The material properties are assigned the user-defined values

```
myAssemb=myModel.rootAssembly
myThing=myAssemb.Instance(name='thing', part=myPart, dependent=OFF)
myModel.StaticStep(name='Load', previous='Initial',
    description='Apply the load', initialInc=1, maxInc=1)
```

The body part is loaded in the model itself and the step of calculation is defined

```
cracktip=myThing.vertices.findAt(((lastP[0],lastP[1],0),))
myAssemb.Set(vertices=cracktip, name='crtipset')
loadr=myThing.edges.findAt((50,0,0))
loadreg = myThing.edges[loadr.index:(loadr.index+1)]
myAssemb.Set(edges=loadreg, name='loadface')
resr=myThing.edges.findAt((2000,-100,0))
resreg = myThing.edges[resr.index:(resr.index+1)]
myAssemb.Surface(side1Edges=resreg, name='ressurf')
baser=myThing.edges.findAt((500,-2000,0))
basereg = myThing.edges[baser.index:(baser.index+1)]
myAssemb.Set(edges=basereg, name='baseface')
```

The nodes sets which will be subjected to load of boundary conditions and are defined

```
crackS=myThing.faces.findAt((lastP[0],lastP[1],0))
cracksup=myThing.faces[crackS.index:(crackS.index+1)]
myAssemb.Set(faces=cracksup, name='cracksurf')
crackreg=myThing.edges.findAt(((xyCoordsCrack[-1][0],
  xyCoordsCrack[-1][1],0),))
for i in range(len(xyCoordsCrack)-2): crackreg = crackreg +
  myThing.edges.findAt((((xyCoordsCrack[i][0] +xyCoordsCrack[i+1][0])
  /2,(xyCoordsCrack[i][1]+xyCoordsCrack[i+1][1])/2,0),))
myAssemb.Set(edges=crackreg, name='crackseam')
pickedRegions = myAssemb.sets['crackseam']
myAssemb.engineeringFeatures.assignSeam(regions=pickedRegions)
qvect=((xyCoordsCrack[-2][0],xyCoordsCrack[-2][1],0),(xyCoordsCrack
  [-1][0], xyCoordsCrack[-1][1],0))
crackFront = crackTip = myAssemb.sets['crtipset']
myAssemb.engineeringFeatures.ContourIntegral(name='Crack',
  symmetric=OFF, crackFront=crackFront, crackTip=crackTip,
  extensionDirectionMethod=Q_VECTORS, qVectors=((qvect), ),
  midNodePosition=0.25, collapsedElementAtTip=SINGLE_NODE)
```

The crack geometry is assigned and the parameters of the crack calculation are defined

```
myModel.DisplacementBC(name='baseBC', region=myAssemb.sets
  ['baseface'], createStepName='Initial', u2=0.0, fixed=OFF,
  distributionType=UNIFORM)
myModel.DisplacementBC(name='load', region=myAssemb.sets
  ['loadface'], createStepName='Load', u2=dep, fixed=OFF,
  distributionType=UNIFORM)
if resstr!=0.0 and udsd=='':
    myModel.Pressure(name='resstr', region=myAssemb.
    surfaces['ressurf'], createStepName='Load', magnitude=resstr,
    distributionType=UNIFORM)
if udsd:
    myModel.Pressure(name='resstr', region=myAssemb.surfaces
    ['ressurf'], createStepName='Load', magnitude=resstr,
    distributionType=USER_DEFINED)
```

Boundary conditions and loads are assigned the user-defined values

```
myAssemb.seedEdgeBySize(edges=(loadr,), size=1.5, constraint=FREE)
myAssemb.seedEdgeByNumber(edges=(baser,), number=60, constraint=FINER)
myAssemb.seedEdgeBySize(edges=myThing.edges.findAt
  (((rad0+0.5,0,0),)), size=1.5, constraint=FINER)
myAssemb.seedEdgeBySize(edges=myThing.edges.findAt
  (((rad0*rovera+1,0,0),)), size=1.0)
myAssemb.seedEdgeByBias(end2Edges=myThing.edges.findAt
  (((500,0,0),)), ratio=5, number=100)
myAssemb.seedEdgeByNumber(edges=myThing.edges.findAt
  (((2000,-300,0),)), number=60)
myAssemb.seedEdgeBySize(edges=myThing.edges.findAt
  (((0,pointTrans2[1]+2,0),)), size=1.5)
myAssemb.seedEdgeByBias(end1Edges=myThing.edges.findAt(((0,
  pointTrans2[1]-4,0),)), ratio=3, number=80)
for t in range(-int(pointTrans2[1]/4.5)): myAssemb.seedEdgeByNumber
  (edges=myThing.edges.findAt(((pointTrans2[0]+3,-3-t*4.5,0),)),
```

```
  number=1)
for t in range(-int(pointTrans2[1]/1.5)): myAssemb.seedEdgeByNumber
  (edges=myThing.edges.findAt(((pointTrans2[0],-0.1-t*1.5,0),)),
  number=1)
for t in range(-int(pointTrans2[1]/4.5)): myAssemb.seedEdgeByNumber
  (edges=myThing.edges.findAt(((pointTrans2[0]+1,-t*4.5,0),)),
  number=1)
for t in range(int(pointTrans2[0]/4.5)): myAssemb.seedEdgeByNumber
  (edges=myThing.edges.findAt(((3+t*4.5,pointTrans2[1]-3,0),)),
  number=1)
for t in range(int(pointTrans2[0]/1.5)): myAssemb.seedEdgeByNumber
  (edges=myThing.edges.findAt(((t*1.5,pointTrans2[1]-1.1,0),)),
  number=1)
myAssemb.seedEdgeBySize(edges=crackreg, size=seedCrack,
  constraint=FREE)
myAssemb.seedEdgeByNumber(edges=myThing.edges.findAt(((lastP[0],
  lastP[1],0),)), number=12, constraint=FINER)
myAssemb.seedEdgeByNumber(edges=myThing.edges.findAt(((lastP[0]+incr,
  lastP[1],0),)), number=36, constraint=FINER)
```

The element (approximate) size is assigned to some of the faces the model is composed of

```
myThing.faces.findAt((pointTrans[0]+2,pointTrans[1]-2,0)))
myAssemb.setMeshControls(regions=(crackS,),
  elemShape=QUAD_DOMINATED, technique=SWEEP)
ba=myThing.faces.findAt(((rad0*rovera-0.1,-0.1,0),))
myAssemb.setMeshControls(regions=ba, algorithm=ADVANCING_FRONT)
aba=myThing.faces.findAt(((1500,-1000,0),))
myAssemb.setMeshControls(regions=aba, algorithm=ADVANCING_FRONT)

elemType1 = mesh.ElemType(elemCode=CAX8, elemLibrary=STANDARD,
    secondOrderAccuracy=OFF, hourglassControl=STIFFNESS,
    distortionControl=OFF)
```

```
myAssemb.setElementType(regions=(myThing.faces,), elemTypes=
  ((elemType1,)))
myAssemb.generateMesh(regions=((myThing,)))
```

The meshing techniques and the element types are assigned to the relevant faces of the model

```
myModel.fieldOutputRequests['F-Output-1'].setValues(variables=('S',
  'U','RT'))
myModel.historyOutputRequests.changeKey(fromName='H-Output-1',
    toName='JInt')
myModel.historyOutputRequests['JInt'].setValues(
    contourIntegral='Crack', numberOfContours=9)
myModel.HistoryOutputRequest(name='StrInt', createStepName='Load',
    contourIntegral='Crack', numberOfContours=9,
    contourType=K_FACTORS, kFactorDirection=KII0)
```

The output requested, including the fracture mechanics response, is defined

```
if udsd:
    userFile = udsd+'.for'
    myJob = mdb.Job(name=mdname, model=myModel, description='Crack
      propagation - steps', userSubroutine=userFile)
else:
    myJob = mdb.Job(name=mdname, model=myModel, description='Crack
      propagation - steps')
```

A case job is created with the model name; the eventual user-defined pressure distribution is assigned.

A.3 output.py

```
'''
readoutput.py
Reading the odb, getting KI, KII, Dang, load
Version with Shielding
'''
```

Headings of the script; name and scope

```
odb = openOdb(path=mdname+".odb")
```

The file containing the result of the calculation is opened

```
KIav=(odb.steps['Load'].historyRegions['ElementSet  PIBATCH'].
  historyOutputs['K1 at STRINT_CRACK_CRTIPSET_Contour_6'].data[0][1]+
  odb.steps['Load'].historyRegions['ElementSet  PIBATCH']
  .historyOutputs['K1 at STRINT_CRACK_CRTIPSET_Contour_7'].data[0][1]+
  odb.steps['Load'].historyRegions['ElementSet  PIBATCH'].
  historyOutputs['K1 at STRINT_CRACK_CRTIPSET_Contour_8'].data[0][1]+
  odb.steps['Load'].historyRegions['ElementSet  PIBATCH'].history
  Outputs['K1 at STRINT_CRACK_CRTIPSET_Contour_9'].data[0][1])/4
KIIav=(odb.steps['Load'].historyRegions['ElementSet  PIBATCH'].
  historyOutputs['K2 at STRINT_CRACK_CRTIPSET_Contour_6'].data[0][1]+
  odb.steps['Load'].historyRegions['ElementSet  PIBATCH'].
  historyOutputs['K2 at STRINT_CRACK_CRTIPSET_Contour_7'].data[0][1]+
  odb.steps['Load'].historyRegions['ElementSet  PIBATCH'].
  historyOutputs['K2 at STRINT_CRACK_CRTIPSET_Contour_8'].data[0][1]+
  odb.steps['Load'].historyRegions['ElementSet  PIBATCH'].history
  Outputs['K2 at STRINT_CRACK_CRTIPSET_Contour_9'].data[0][1])/4
Jint=(odb.steps['Load'].historyRegions['ElementSet  PIBATCH'].
  historyOutputs['J at JINT_CRACK_CRTIPSET_Contour_6'].data[0][1]+
  odb.steps['Load'].historyRegions['ElementSet  PIBATCH'].
  historyOutputs['J at JINT_CRACK_CRTIPSET_Contour_6'].data[0][1]+
  odb.steps['Load'].historyRegions['ElementSet  PIBATCH'].
  historyOutputs['J at JINT_CRACK_CRTIPSET_Contour_6'].data[0][1]+
```

```
odb.steps['Load'].historyRegions['ElementSet  PIBATCH'].
historyOutputs['J at JINT_CRACK_CRTIPSET_Contour_6'].data[0][1])/4
```

The stress intensity factors K_I, K_{II} and the fracture energy G are calculated as an average of the values given along four contours at the crack tip

```
KiiSh=Kinf2*(1-exp(-crl/lambd))
KiSh=Kinf*(1-exp(-crl/lambd))
```

The mode-I and mode-II shielding stress intensity factors are calculated (if present) as a function of the user-defined parameter λ and of the crack length c

```
deltaang2=radianToDegree(-2*(KIIav+KiiSh)/KIav)
```

The kink angle β is calculated following eq. 3.4

```
loadcalc=0
val=odb.steps['Load'].frames[1].fieldOutputs['RT']
appl=odb.rootAssembly.nodeSets['LOADFACE']
val.getSubset(region=appl)
applvalu=val.getSubset(region=appl)
for hj in applvalu.values: loadcalc=loadcalc+ hj.data[1]
```

The indentation load P is calculated as the sum of the reaction forces at the contact nodes

```
odb.close()
```

The results file is closed.

A.4 initcrack.py

The `initcrack.py` script is a modification of `propcrack.py`which calculates the fracture energy G at the tip of short cracks near the contact zone, with both the crack position and size as parameters. Such script was employed for the example given in section 3.5.1.

```
,,,
initcrack.py
Crack initiation energy: root model
,,,
```

Headings of the script; name and scope

```
from odbAccess import *
import visualization

dep=-3.0
rad=100.0
incr=0.2
youn=380000.0
poiss=0.25
KIcrit=3000.0
rad0=100
seedCrack=0.1
matname='alumina'
resstr=0
udsd=FALSE
```

The necessary variables are defined

```
deff=[0.5,0.6,0.7,0.8,0.9,1.0,1.2,1.4,1.6,1.8,2.0,2.5,3.0,3.5,4.0,4.5
    ,5.0,5.5,6.0,6.5,7.0,7.5,8.0,8.5,9.0,9.5,10.0,12.0,14.0,16.0,18.0
    ,20.0]
rov=[1.05,1.1,1.2,1.3,1.4,1.5,1.6]
```

the arrays `deff` and `rov` contain the combinations of crack sizes and positions which will be calculated

```

```

```
mdname='crackdef'
logr=open(mdname+".txt",'w')
logr.close()
```

the model and the output file are created

```
for kk in range(len(deff)):
    logr=open(mdname+".txt",'a')
    logr.write('%s '%(deff[kk]))
    for ll in range(len(rov)):
        rovera=float(rov[ll])
        defect=float(deff[kk])

        ang=270
        crl=defect
        xyCoordsCrack = [(rad0*rovera,0.), (rad0*rovera,-defect+incr)
            ,(rad0*rovera,-defect)]

        execfile('model.py', __main__.__dict__)
        myJob.submit()
        myJob.waitForCompletion()

        execfile('output.py')
        logr.write('%s ' %(Jint))
    logr.write('\n')
    logr.close()
```

A two-level iterative procedure calculates all the combinations of defect size and position and writes in the output file the values requested in an easy to graph format.

List of publications

Jiménez-Piqué, E., Ceseracciu, L., Chalvet, F., Anglada, M. and de Portu, G. *Hertzian contact fatigue on alumina/alumina-zirconia laminated composites* J Eur Ceram Soc 2005: **25**(15), 3393–3401

Jiménez-Piqué, E., Ceseracciu, L., Chalvet, F., Anglada, M. and de Portu, G. *Fatiga por contacto esfrico en materiales multicapa de almina circona* Bol Soc Esp Ceram Vid 2005: **44**(5), 307–312

Ceseracciu, L., Chalvet, F., de Portu, G., Anglada, M. and Jiménez-Piqué, E. *Surface contact degradation of multilayer ceramics under cyclic subcritical loads and high number of cycles* Int J Refr & Hard Mat 2005: **23**(4–6), 375–381

Ceseracciu, L., Chalvet, F., Jimenéz-Piqué, E., Anglada, M. and de Portu, G. *Contact fatigue in ceramic laminated composites* Key Eng Mat 2005: **290**, 222–229

Hvizdos, P., Calderon Moreno, J.M., Ocenasek, J., Ceseracciu, L. and Anne, G. *Mechanical properties of alumina/zirconia functionally graded prepared by electrophoretic deposition* Key Eng Mat 2005: **290**, 332–335

Jiménez-Piqué, E., Ceseracciu, L., Gaillard, Y., Brach, M., de Portu, G. and Anglada, M. *Instrumented indentation on alumina-alumina/zirconia multilayered composites with residual stresses* Phil Mag 2006: **86**(33–35), 5371–5382

Ceseracciu, L., Jiménez-Piqué, E. and Anglada, M. *Cone cracks in laminated ceramics with residual stress* in B. Wilshire and M. Bache, eds., *Proceedings of the 10th European Inter-regional conference on Ceramics* Swansea Materials Research Center 2006: 199–208

Ceseracciu, L., Anglada, M. and Jiménez-Piqué *Influence of residual stress on cone crack propagation in brittle materials under blunt indentation* in *Anales de mecánica de la fractura* volume 23 2006: 479–484

Ceseracciu, L., Anglada, M. and Jiménez-Piqué, E. *Influence of the cone crack geometry on the strength degradation* Key Eng Mat 2007: **333**, 255–258

Ceseracciu, L., Anglada, M. and Jiménez-Piqué, E. *An automated model of crack propagation on brittle materials* in M. Anglada, ed., *Proceedings of the fourth meeting of the European school of Materials Science and Engineering* 2007: 245–252

Ceseracciu, L., Anglada, M. and Jiménez-Piqué E. *Hertzian cone crack propagation on polycrystalline materials: role of* R*-curve and residual stresses* Acta Mater 2008: **56**(2), 265–273

Ceseracciu, L., Jiménez-Piqué, E., Fett, T. and Anglada, M. *Contact strength of ceramic laminates* Compos Sci Technol 2008: **68**(1), 209–214

Ceseracciu, L., Anglada, M. and Jiménez-Piqué, E. *Influence of the elastic mismatch on the Hertzian cone crack propagation in brittle bilayers* in *Anales de mecánica de la fractura* volume 25 2008: 102–106